Fermi National Accelerator Laboratory

FERMILAB-TM-1946

Status Report: Technical Design of Neutrino Beams for the Main Injector (NuMI)

D.A. Crane, W. Freeman, M.C. Goodman, D. Johnson, A. Malensek, J.G. Morfin, S. O'Day, J. Thomas

Fermi National Accelerator Laboratory
P.O. Box 500, Batavia, Illinois 60510

July 1995

Operated by Universities Research Association Inc. under Contract No. DE-AC02-76CHO3000 with the United States Department of Energy

Disclaimer

This report was prepared as an account of work sponsored by an agency of the United States Government. Neither the United States Government nor any agency thereof, nor any of their employees, makes any warranty, expressed or implied, or assumes any legal liability or responsibility for the accuracy, completeness, or usefulness of any information, apparatus, product, or process disclosed, or represents that its use would not infringe privately owned rights. Reference herein to any specific commercial product, process, or service by trade name, trademark, manufacturer, or otherwise, does not necessarily constitute or imply its endorsement, recommendation, or favoring by the United States Government or any agency thereof. The views and opinions of authors expressed herein do not necessarily state or reflect those of the United States Government or any agency thereof.

NuMI-B-92

Status Report: Technical Design of Neutrino Beams for the Main Injector (NuMI)

July 21, 1995

D. A. Crane[1], W. Freeman[5], M. C. Goodman[1], D. Johnson[5], A. Malensek[5], J. G. Morfin[5], S. O'Day[5], J. Thomas[8]

1. Argonne National Laboratory
2. Boston College
3. Caltech
4. Columbia University
5. Fermilab
6. Kansas State University
7. University of Michigan
8. Oxford University
9. Stanford University
10. Tufts University

The following members of the NuMI Beam Group also contributed to the overall design of the neutrino beams

R. Bernstein[5], R. E. Blair[1], D. Bogert[5], D. Carey[5], Y. Ho[4], G. Koizumi[5], W. Lee[4], D. Michael[3], R. Milburn[10], F. Nezrick[5], G. Rameika[5], A. L. Read[5], N. W. Reay[6], B. Roe[7], N. Stanton[6], T. Toohig[2], S. Wojcicki[9]

Contents

1 Introduction **11**
1.1 Neutrinos at the Main Injector (NuMI) 11
1.2 Previous Studies 12

2 Main Injector Extraction **16**
2.1 Main Injector extraction geometry 16
2.2 Beamline description 17
2.3 Beamline optics 22

3 The Neutrino Beam Lines **32**
3.1 Beam Design Criteria 34
3.2 Calculation of Neutrino Flux 37
3.3 Wide Band Beam 38
3.3.1 Focusing Devices 38
3.3.2 Double Horn Design 39
3.3.3 Horn Design Parameter Variations 45
3.3.4 Horn Electrical Design 47
3.3.5 Horn Support Design 49
3.3.6 Neutrino Event Rates 53
3.3.7 Neutrino Backgrounds 58
3.4 Narrow Band Beam 59
3.4.1 Physical Layout 60
3.4.2 Lithium Lens Design and Operation 61
3.4.3 NBB Optics 62
3.4.4 NBB Element Support Design 62
3.4.5 NBB Tunes and Neutrino Event Rates 65
3.4.6 NBB backgrounds 68
3.5 Replacement of Failed Components 69
3.6 Radiation Handling and Shielding 69
3.7 Switching between Wide–band and Narrow–band beams 73
3.8 Maintenance of the neutrino beamline 74

4 The Target for the Wideband Beam **78**
4.1 Secondary Particle Production 78
4.2 Energy Deposition 79

4.3 Temperature Distribution and Cooling 79
4.4 Stresses 80
4.5 Conclusions 81

5 The Decay Region **84**
5.1 Optimizing the ν_τ rate at the far detector 84
5.2 Variation of the ν_τ rate at the near detector 87
5.3 Precision of beam pointing to the far detector 90

6 NuMI Beam Monitoring **92**
6.1 Monitoring of the Wide Band Beam 92
6.1.1 The Proton Beam 92
6.1.2 The Secondary Hadron Beam and Muon Beam 93
6.1.3 Target and Horn Displacement Studies 94
6.2 Monitoring of the Narrow Band Beam 95

7 Radiation Safety **103**
7.1 Introduction 103
7.2 CASIM Model Geometry 103
7.3 Shielding of Prompt (Beam-on) Radiation 106
7.3.1 Pre-target Enclosure 106
7.3.2 Target Hall 106
7.3.3 Decay Pipe 107
7.3.4 Summary 107
7.4 Activation of Shielding and Components 107
7.5 Air Activation 110
7.6 Ground Water and Surface Water Activation 111
7.7 Summary 113

8 Optimization of the Beam Lines **116**
8.1 Pre-target proton transport and the target 116
8.2 Secondary Collection and Focusing 117
8.3 Replacement of Damaged Components 117
8.4 Decay Region 118
8.5 Monitoring 118

A Neutrino Oscillations Facility: Design Basis for Civil Construction - G. Koizumi, Fermilab and T. Toohig, Boston College **119**
A.1 Scope 119
A.2 Design Considerations 119
A.3 The Pre-Target System 120
A.4 The Target Hall 121
A.5 The Decay Tunnel and Pipe 121
A.6 The Dump Enclosure 121
A.7 The Detector Hall 122

B NuMI Technical Costs (preliminary) **123**

C Reply to HEPAP Subpanel Questions **128**
C.1 Question #1 (a): Near Hall Location 128
C.2 Question #1 (c): Lower Neutrino Energies 136
C.2.1 Introduction 136
C.2.2 Narrow-band beam 136
C.2.3 Wide-band beam 136
C.2.4 Conclusion 137
C.3 Question #1 (d): Higher Energy Protons 142
C.3.1 Higher energy beam from the Main Injector 142
C.3.2 Tevatron beam possibilities 142
C.4 Question #1 (e): Effects of the Decay Pipe Baffles 144

List of Tables

1.1 Neutrino Oscillation proposals for use of the Fermilab Main Injector. The first four proposals were submitted in 1990-91. The last four were submitted in 1994. 12
1.2 Documents leading to the NuMI beam design. 14

2.1 Nominal Dipole Strengths for Wide Band Beam 18
2.2 Nominal Quadrupole Strengths for Wide Band Beam. 23
2.3 Quadrupole Strengths verses beam size [mm] on target. 24

3.1 Dimensions of the two horns and design values of the power supplies. 39
3.2 Variation of ν_τ event rates and average energy for changes in Horn 1 length. 45
3.3 Expected number of muon and tau neutrino events in a kiloTon-year at Soudan for $\sin^2 2\theta = 1.0$ and various values of Δm^2. 53
3.4 Expected number of muon and tau neutrino events in a kiloTon-year at Soudan for $\sin^2 2\theta = 1.0$ and various values of Δm^2 for the 15 GeV π^+ NBB. 65
3.5 Expected number of muon and tau neutrino events in a kiloTon-year at Soudan for $\sin^2 2\theta = 1.0$ and various values of Δm^2 for the 30 GeV π^+ NBB. 66
3.6 Expected number of muon and tau neutrino events in a kiloTon-year at Soudan for $\sin^2 2\theta = 1.0$ and various values of Δm^2 for the 45 GeV π^+ NBB. 66
3.7 Expected number of muon and tau neutrino events in a kiloTon-year at Soudan for $\sin^2 2\theta = 1.0$ and various values of Δm^2 for the 60 GeV π^+ NBB. 66

4.1 Event rate for various targets. z = 0 is the upstream end of Horn 1. 78
4.2 Properties of ZXF-5Q Graphite. 79
4.3 Maximum Temperature for various target sizes and forms of cooling where natural and forced convection uses He gas. 81

C.1 Integrated NuMI flux and event rate as a function of energy, for a two year exposure of a 7 kT MINOS far detector. Neutrino flux is given in units of $m^{-2}GeV^{-1}$. 140
C.2 WBB energy fluxes for 170 kAmp (nominal) and 50 kAmp horn currents, compared to 10 GeV (E_π) NBB fluxes, at the MINOS far detector for a two-year exposure. 140
C.3 The locations and inner diameters of the collimators along the NuMI beamline. 144

List of Figures

2.1 Elevation view of the NuMI extraction beamline (top) and the MI ring. The MI quadrupole 608 is located between the first two (of three) extraction lambertsons (large boxes). Vertical scale is exaggerated. 19
2.2 Elevation view of the NuMI beamline in the Extraction Stub. Vertical scale is exaggerated. 20
2.3 Elevation view of the Pre-target area showing the WBB primary beamline (shaded). The last two (unshaded) magnets, B6(A,B), before the target are included in the NBB option and are not installed in the WBB beamline. Vertical scale is exaggerated. 21
2.4 Distribution of particles during 1 ms resonant extraction. 24
2.5 Normalized phase space of circulating and extracted beam midway through extraction. 25
2.6 Comparison between resonant extraction beam distribution and nominal MI lattice optics at the face of the first extraction Lambertson. 26
2.7 Lattice functions of primary beamline to target. Target is located at 360 m. 27
2.8 Beam sizes through the pre-target hall corresponding to various Courant-Snyder parameters. The first two quadrupoles in the triplet are located at s = 320 meters with the third quadrupole at s = 350 meters. The vertical beam size is shown as the dashed line. 28
2.9 Beam size at the longitudinal midpoint of the target from tracking an extracted phase space distribution of roughly 1000 particles through six optical solutions. The dashed circle represents a 2 mm radius target. 29

3.1 The approximate layout of the NuMI neutrino facility for E–803 (COSMOS) and E–875 (MINOS). 33
3.2 a) A sample secondary particle energy spectrum, b) the CC ν_τ cross section and c) the product of a) and b). 35
3.3 The CC ν_τ event rate shape (solid) obtained by multiplying the WBB ν_μ flux (dashed) by the ν_τ CC cross section shape. 36
3.4 Depth of focus for the nominal double horn system. 41
3.5 The optics of the triple horn system. 42
3.6 Schematic diagram of the wide–band beam illustrating the regions of magnetic field and the dimensions of the beam line. 43
3.7 Comparison of the double horn beam focus to "perfect" focus. The lines are solely to guide the eye. 44

3.8 Comparison of the relative ν_τ event rate and average event energy as the length of the horn is varied. 46
3.9 The horn electrical circuits for a) the transformer option and b) the no transformer option. 48
3.10 A representation of the complete horn assembly viewed from the side of the horn. 51
3.11 A conceptual design for the alignment table position adjusting system viewed from the downstream end of the first horn. 52
3.12 The CC ν_μ event rate at the near detector. 54
3.13 The CC ν_μ event rate at the far detector. 55
3.14 The $\nu_\mu \rightarrow \nu_\tau$ oscillation probability curves at the far detector for various Δm^2 with $\sin^2 2\theta = 1.0$. 56
3.15 a) The ν_τ flux at Soudan for $\sin^2 2\theta = 1.0$ and $\Delta m^2 = 0.005$, 0.02 and 0.1 with the ν_μ flux shown for comparison. b) The CC ν_τ event rate at the far detector for $\sin^2 2\theta = 1.0$ and $\Delta m^2 = 0.005$, 0.02 and 0.1 eV^2. 57
3.16 The ν_μ, ν_e, $\overline{\nu}_\mu$, and $\overline{\nu}_e$ flux for the 800 m nominal decay pipe. The absolute value of the vertical scale is arbitrary. Only the relative values for each ν type are important. 58
3.17 Schematic diagram of the wide–band and narrow–band beams. The figure is not to scale in the direction perpendicular to the beamline. 59
3.18 The angular paths of the wide and narrow band beams. 60
3.19 A cutaway view of the Fermilab $\overline{p}$ source lithium lens. 63
3.20 The Narrow Band Beam design optics. L is the Li-lens, Q are quadrupoles and B1 and B2 are the two bends. The upper trajectory is the vertical (bend plane) while the bottom is the horizontal trajectory. 64
3.21 The Narrow Band Beam CC ν_μ event rates at the far detector. 67
3.22 The danger parameter curves from the Fermilab Radiological Control Manual for Fe, Al, and $CaCO_3$ for 360 days of beam. 71
3.23 The shielding design for the NuMI first horn with pieces removed and stacked showing the access to the horn. 72
3.24 The layout of the WBB and the shielding design for it viewed from the top with the top shielding removed. 75
3.25 The layout of the NBB and the shielding design for it viewed from the top with the top shielding removed. 76
3.26 The layout of the WBB and NBB with the location of the NBB dump shown. 77

4.1 The design of the NuMI target. 82
4.2 The target temperature profile as a function of time for a) the rise to steady state and b) at steady state for two beam pulses 1.9 seconds apart. 83

5.1 Comparison of the ν_τ event rates at Soudan for decay lengths from 300 to 1000 m and decay pipe radii from 0.25 to 4.0 m using the WBB. 85
5.2 Comparison of the ν_τ event rates at Soudan for decay lengths from 300 to 1000 m and decay pipe radii from 0.25 to 3.0 m using a generic 45 GeV/c NBB. 86

5.3 Comparison of the ν_τ event rates at Fermilab for decay lengths from 300 to 1000 m and decay pipe radii from 0.25 to 3.0 m for the WBB. Note the suppressed zero on the vertical scale. 88
5.4 Comparison of the $\sin^2 2\theta$ sensitivity of E–803 for decay lengths from 100 to 1200 m for $\Delta m^2 = 20$, 50 and 1000 eV^2. 89
5.5 a) A comparison of NUADA and PBEAM calculations of the ν_μ beam profile at the far detector (note the suppressed zero on the vertical scale), b) The ν_μ flux normalized by the area of the 10 m bin size annulus, and c) the normalized ν_e flux *vs* distance from beam center at the far detector for a finer distance scale, using the PBEAM program. Only the relative values on the vertical scales are important. 91

6.1 Schematic showing the layout of the proton line and SWICs for Narrow Band and Wide Band Beam Configurations. 93
6.2 The radial distributions of the π^+s, K^+s and protons at the end of the second horn. 96
6.3 The energy distributions of the π^+s, K^+s and protons at the end of the second horn. 97
6.4 a) Energy of the π^+s vs radius at the beginning of the decay pipe, b) energy of the K^+s vs radius in the same location and c) energy vs radius of the protons in the same location. 98
6.5 Schematic showing the layout of the dump and muon monitoring device. . . 99
6.6 a)The energy distributions of the μs at the end of the decay pipe, b) the radial distribution of the μs and c) the energy *vs* radial position. 100
6.7 Schematic showing definitions of quadrants 101
6.8 Up-down and left-right asymmetry plotted as a function of radius after the dump as a simulation of the muon flux from decayed hadrons in the decay pipe for three different horn system offsets (x) for muons from 10^8 protons on target. (A+B)-(C+D) shows the up down asymmetry (which is essentially zero) and (A+C)-(D+B) is the left-right asymmetry resulting from the shift in position in x. 102

7.1 NUMI target hall and decay tunnel geometry used for CASIM calculations. Note that the radial and longitudinal scales are different. Horizontal dimensions in meters and vertical dimensions in cm. 105
7.2 The star density for the radial bin 160 cm $< R <$ 170 cm in the target hall region ($Z <$ 50 meters). This radial bin corresponds to the outer surface of the steel and concrete shielding installed within the target hall. The horizontal line corresponds to the star density limit that results in 100 mrads per hour residual dose rate at the surface of the steel for infinite irradiation and zero cooloff times with a primary beam intensity of 4×10^{13} protons every 2 seconds.109

7.3 The star density for the radial bin 100 cm< R <110 cm as a function of the distance along the beam line. The solid circles are the CASIM results with no forward "collimator" shielding installed. The solid squares are the CASIM results with 2 meter long steel collimators located at 48, 96, 208 and 304 meters. The horizontal line indicates the limiting star density for surface water discharge assuming 3.7×10^{20} targeted protons per year. Other lines are drawn to guide the eye. 114
7.4 The star density for the radial bin 250 cm < R < 260 cm as a function of the distance along the beam line in the target hall region (Z < 50 meters). The solid squares are the CASIM results. The horizontal line indicates the limiting star density for surface water discharge assuming 3.7×10^{20} targeted protons per year. The other lines are drawn to guide the eye 115

C.1 Map of the Fermilab site, showing the location of the NuMI beamline and the constraints imposed by the two branches of Pine Street and by the site boundary. 130
C.2 Expected 90% confidence level limit curves for $\nu_\mu \rightarrow \nu_\tau$ oscillations in the COSMOS experiment for various decay pipe lengths L and shield lengths d (labelled as "$L + d$ m"). 131
C.3 Normalized far - near differences between the neutrino flux energy spectra for various decay-pipe lengths L and shield lengths d (labelled as "$L + d$ m"). . 132
C.4 Dependence of the parameter S on the shield length d. S is a figure of merit which characterizes the beam spectrum difference between the near and far detectors. S is defined on page 10 of the "MINOS Answers" document as the maximum difference between the normalized integral neutrino spectra at the near and far detectors. 133
C.5 Dependence of the ratio T_{near}/T_{far} (where T = CC/total event ratio) on shield length d for four different energy cuts. 134
C.6 The ν_μ fluxes at the MINOS far detector for the NBB tuned to 10, 20, and 45 GeV. 138
C.7 The ν_μ CC event rate at the far detector as a function of the position of the upstream end of the target (in cm) with respect to the lithium lens focal point (for a one kT-year MINOS exposure). The position plotted is positive as the target is moved upstream. 139
C.8 Relative fluxes obtained from the wide band beam using the nominal (170 kAmp) and low-energy (50 kAmp) horn current settings described in the text. 141
C.9 a) ν_μ fluxes for the uncollimated and collimated wide-band beams. b) The far-detector flux minus the inner near-detector flux, normalized to unit areas, for the uncollimated and collimated beams. 145
C.10 The ν_μ CC event rates for the nominal beam and the beam with collimators for four different radial regions in the near detector. 146

EXECUTIVE SUMMARY

This report represents the accumulated experience of over seven years of Fermilab reviews, workshops and summer studies on the topic of what kind of neutrino beams are required to investigate neutrino oscillations and how do we most efficiently produce these beams. There have been many refinements and improvements over these years and the process of optimizing the beam design, both in terms of cost and efficiency, is still underway.

The emphasis of the Fermilab NuMI Beam Group has been to provide a facility enabling multiple tests for the discovery and, should a signal be found, the subsequent study of the phenomena of neutrino oscillations. To effectively meet these requirements two types of beams, which take advantage of the energy (120 GeV) and high proton intensity ($3-4\times10^{13}$ protons every 1.9 seconds) of the Main Injector, have been developed . A standard wide-band beam will provide an intense beam of muon neutrinos of sufficient energy to interact, should they oscillate, as tau neutrinos. In addition, a narrow-band beam will provide the experimenters with a new tool to study restricted energy bands with minimal background. These beams, in combination with the short-baseline experiment COSMOS (E803) and the long-baseline experiment MINOS (E875), will enable a series of independent investigations of the phenomena over a wide new range in the Δm^2 - $\sin^2 2\theta$ plane.

What is presented in this report is a design of a double-horn wide-band neutrino beam similar to those which have been used for over 20 years at Fermilab and other accelerator laboratories. Also presented is the design of a narrow-band (di-chromatic) beam employing a Li-lens collector identical to that successfully used in the Fermilab anti-proton source for nearly 10 years. The beamline optics required to extract the protons from the Main Injector and transport them to the production targets is described. The topic of monitoring of the beams so as to reduce beam-associated systematic errors is also covered and the question of radiation safety is addressed. It is important to emphasize that, even though our optimization studies are not yet complete, the facility as described here can provide both experiments with the beams necessary to do the physics presented in their respective proposals.

Chapter 1

Introduction

1.1 Neutrinos at the Main Injector (NuMI)

Soon after the Main Injector was proposed as a luminosity upgrade for the Tevatron collider experiments, it was realized that a moderate energy (120 GeV) high-intensity proton beam could lead to neutrino beams with unprecedented fluxes[1]. There followed a proposal for a short-baseline neutrino oscillation experiment[2], and several ideas for using the same beam for a long-baseline neutrino oscillation experiment[3]. A list of the proposed experiments is given in Table 1.1. As suggestive evidence for neutrino mass and neutrino oscillations continues to grow from solar neutrino experiments,[4] atmospheric neutrino experiments[5] and the missing matter problem,[6] the prospect of using one neutrino beam to significantly improve the sensitivity of neutrino oscillation searches in both Δm^2 and $\sin^2(2\theta)$ has become increasingly attractive.

Working with the advocates of ν oscillation experiments at Fermilab, a succession of beam working groups have studied possible neutrino beams at Fermilab since 1988. A list of several beam design study reports is given in Table 1.2. Fermilab has a long history of neutrino experiments using a double horn wide band beam (WBB) and early in the process it was realized that a double horn system would produce a high intensity neutrino flux, useful for both short-baseline and long-baseline experiments. More recently, it has been concluded that there are many advantages for a narrow band beam (NBB) as well, so now the capability for both beams is a desirable feature of a new neutrino facility.

The Fermilab Program Advisory Committee carefully studied the physics goals of the various proposals. A neutrino physics subcommittee was appointed and heard reports from proposal advocates in 1991 and again in 1993. In response to advice from this subcommittee, the short-baseline proposal (E803) was approved in November of 1993. A call for expressions of interest (EOI's) for long baseline experiments was issued by Fermilab in March of 1994 leading to the eventual approval of a long-baseline proposal (E875) in February, 1995. The present course for neutrino experiments at the Main Injector was set by Fermilab Director John Peoples after a report was issued by the Physics Advisory Committee in June 1994 [7]. As a result, Fermilab has developed a detailed design for a Main Injector neutrino beamline suitable for neutrino oscillation experiments. The present beam working group includes representatives of the Fermilab Research Division, the Main Injector Department

and the two experiments, E–803 and E–875. This Technical Design Status Report (TDR) for the beam lines and their technical components, and the concurrent volume describing the required civil construction are a result of these studies.

Experiment	Spokesman
E–803	Reay
P–805	Gajewski
P–822	Goodman
P–824	Stenger
EOI–7	Wojcicki
EOI–8	Barish/Michael
EOI–9	Goodman
E–875	Wojcicki

Table 1.1: Neutrino Oscillation proposals for use of the Fermilab Main Injector. The first four proposals were submitted in 1990-91. The last four were submitted in 1994.

In Section 1.2 of this introduction to the TDR, a historical review of the NuMI project will reference previous studies which were relevant to the present NuMI beam design. In Chapter 2, the plan for extraction from the Main Injector and proton transport to the NuMI target is described. Chapter 3 covers the focusing systems starting with the construction, mechanical and electrical details of the horns as well as radiation handling and shielding. A horn replacement scheme is described, in the event of horn failure, and the present design of a narrow band beam using a Lithium Lens is presented. Chapter 4 describes the wideband beam target and related systems. Chapter 5 covers the decay region and the dump. Beam monitoring systems are described in chapter 6. The precautions for groundwater protection and other safety issues are presented in chapter 7. Finally in chapter 8, an optimization program for further beam development is reviewed.

1.2 Previous Studies

It was recognized in 1988 that the Main Injector would provide a very high intensity of moderate energy protons, (4×10^{13} 120 GeV protons per pulse every 1.9 s) which would enable new short-baseline and long-baseline neutrino oscillation experiments. These ideas were first presented at two Fermilab Workshops, "New Directions in Neutrino Physics at Fermilab", September 14-16, 1988,[8] and the "Proceedings of the Workshop on Physics at the Main Injector", May 16-18 1989 [9]. By the end of the second workshop, four important features of the present NuMI program had been identified:

- Desirability of $\nu_\mu \rightarrow \nu_\tau$ oscillation searches using a beam with E_ν above ν_τ charged current threshold
- Complementarity of long-baseline and short-baseline experiments (motivated by the atmospheric neutrino deficit and missing matter) using the same neutrino beam from

Main Injector protons

- Event rates using the wide band double horn beam and physics tests in both experiments with the lowest possible systematic errors. In order to estimate event rates, the beam calculations used existing programs which were written for the previous double horn neutrino beam at Fermilab [10].

- The advantage of using an existing detector facility for a long baseline experiment, such as the water cerenkov detector at IMB or the Soudan 2 iron calorimeter in northern Minnesota.

As a result of the clear physics interest in new neutrino beams, Fermilab set up a working group in 1990 to address the technical issues of a new neutrino experimental program. That group worked to optimize the physics goals of such a program, while taking into account the practical problems with the beam, groundwater protection, and civil construction issues. A report was prepared in June 1991[11] with title "Neutrino Physics after the Main Injector Upgrade; Physics Goals, Technical Components and Civil Construction". In addition to describing the motivation for the experimental program, an initial design of a joint long-baseline and short-baseline beam was included in this report. For detector site-specific calculations, a beam aimed at the IMB detector near Cleveland Ohio was considered. In particular, the beam transport, target design and horn design in the 1991 report were modeled for the beam calculations at that time, and are the basis of the designs presented here. Issues concerning radiation safety were first addressed in that report; new evaluation techniques and solutions to the problems of groundwater protection have evolved since then.

The growing recognition that a long-baseline neutrino oscillation experiment was technically and economically feasible created increased interest in designing the optimum experiment for such a neutrino program. In November 1991, a Workshop on Long-baseline Neutrino Oscillations was held at Fermilab. The existing world program for neutrino oscillation experiments using accelerators was reviewed, and ideas for long-baseline experiments as well as short-baseline proposals were compared [3]. For the most part, beam designs were not the main issue, and calculations from the June 1991 report were relied upon. The Workshop concluded that the favored location for a new long baseline experiment was the Soudan site, relying in part on the existence of the fine-grained Soudan 2 calorimeter.

When the Main Injector funding issues were resolved in 1992, the proper design of a joint short-baseline and long-baseline beam then became a priority. In 1993 the Research Division began to work with experimenters and the Fermilab Facilities Engineering Services Section (FESS) to work out the difficult civil construction aspects of the beam. The NuMI project group at Fermilab was officially established in 1994. Three "Project Definition Reports" which considered different solutions to civil construction issues were produced in 1993-1994. The first report (MI60 Rev 0) considered extraction from MI-60 in the Main Injector and a deep route for the beam, which would be aimed at Soudan, Minnesota. The second report considered a short-baseline only experiment, which would use protons extracted from MI-40 (MI40 Rev 0). The third report considered a shallower version of the MI-60 beam with reduced excavation costs.

A beam aimed at a detector 730 km away will provide unique surveying requirements for an accelerator. The angular acceptance for most past neutrino detectors has been a few

Document title	Reference	Date
Proceedings of the Workshop on New Directions in Neutrino Physics at Fermilab	Fermilab	Sep. 1988
Proceedings of the Workshop on Physics at the Main Injector	Fermilab	May 1989
Neutrino Physics after the Main Injector Upgrade	1991 CDR	Jun. 1991
Proceedings of the Workshop on Long-baseline Neutrino Oscillation	Fermilab	Nov. 1991
MI 60 Rev 0	E&P 6-7-1	Nov. 1993
MI 40 Rev 0	E&P 6-7-1	Apr. 1994
MI 60 Rev 1	E&P 6-7-1	Jun. 1994
Bibliography of notes before 1994 related to NuMI	NuMI-1	Jan. 1994
An independent check of neutrino and muon flux calculations (Roe)	NuMI-S-2	Jan. 1994
Comparison of Long-baseline Neutrino Beam calculations (Michael)	NuMI-L-19	Aug. 1994
Comparison of Particle Production Measurements and FN-341 with 100 GeV protons (Malensek)	NuMI-B-22	Sep. 1994
Dichromatic Neutrino Beam Using the Main Injector (Malensek)	NuMI-B-24	Sep. 1994
E–803 sensitivity to $\bar{\nu}$ Contamination in the beam (Stanton)	NuMI-S-25	Sep. 1994
Long Baseline Beam Calculations (Blair and Goodman)	NuMI-B-27	Sep. 1994
Narrow Band Dichromatic Neutrino Beam using Plasma Lens or Lithium Lens (Nezrick)	NuMI-B-28	Sep. 1994
Studies of Decay Pipe Radius and Length (Crane)	NuMI-B-35	Nov. 1994
Status and Summary of Neutrino Beams from 120 GeV Protons (Malensek)	NuMI-B-39	Oct. 1994
Beam Issues from a Short-Baseline Perspective (Stanton)	NuMI-S-40	Oct. 1994
NuMI Beamline (Koizumi)	NuMI-B-41	Oct. 1994
Status of Beam Design Studies (Morfin)	NuMI-B-43	Nov. 1994
NuMI Groundwater Limits (Malensek)	NuMI-B-55	Jan. 1995
Lithium Lens Beamline (Malensek)	NuMI-B-56	Jan. 1995
NuMI Survey and Alignment Status and Costs	NuMI-L-62	Jan. 1995
Near/Far Differences (and Similarities) in the NuMI Beam (Crane and Goodman)	NuMI-L-64	Apr. 1995
Neutrino Beam Design Status Report (Morfin)	NuMI-B-67	Nov. 1994
Horn and Dichromatic Layouts (Malensek)	NuMI-B-68	Jan. 1995
A Narrow Band Beamline Pulsed Device Cost List (O'Day)	NuMI-B-73	Apr. 1995
Response to PAC Question No. 2 relating to the NuMI Beam Line	NuMI-L-80	Apr. 1995

Table 1.2: Documents leading to the NuMI beam design.

milliradians, while a 4 meter radius MINOS far-detector subtends only five microradians at the source. However the central 0.25 mr of the produced beam is constant in both flux and energy distribution, so the surveying requirements are not as stringent as they might seem at first. The Fermilab surveying group visited Soudan in May 1993 to tie together coordinates of Fermilab and Soudan with the Global Positioning System (GPS) [12]. The error in the absolute pointing accuracy of the beam is also covered in this document.

The Fermilab Program Advisory Committee approved the short-baseline experiment (E803) in October 1993, and in January 1994 issued a call-for-expressions-of-interest (EOI) for a companion long-baseline experiment. Three EOI's were received in May 1994. Two of them considered the potential advantages of using a narrow band beam, instead of or in addition to the double horn wide band beam. Several narrow band beam designs have been considered since that time, and it appears that the best designs take advantage of a lithium lens. The current civil construction design accommodates both the WBB and the NBB [13].

In August 1994 the present beam group was established to design and cost the NuMI beam. A system of technical reports called NuMI notes was established in January of 1994. These notes discuss issues of relevance to the short-baseline experiment COSMOS, the long-baseline experiment MINOS, the beam design, or the overall NuMI project. Most NuMI notes are available on the World Wide Web at
"*http://www.hep.anl.gov/Hypertext/NDK/numi_notes.html*"
Those which contributed to the technical beam design, or which show beam properties of the current design are listed in Table 1.2.

Chapter 2

Main Injector Extraction

2.1 Main Injector extraction geometry

The Main Injector (MI) straight section, MI-60, will be utilized for resonant extraction for the production of neutrino beams. The bearing of the straight section is 148.7685 degrees counterclockwise with respect to site east. The bearing to Soudan, Mn. and the vertical pitch required have been calculated based upon a Global Positioning Satellite tie to survey monuments outside the Soudan mine entrance [14]. The bearing to Soudan, Mn. is 152.1918 degrees counterclockwise with respect to site east, therefore, only 3.4233 degrees of bend are required to aim the beam toward Soudan. The required pitch from the neutrino production target is -3.3402 degrees.

Three bend centers are required to place the beam on the proper trajectory to Soudan:

- a horizontal bend center in the MI tunnel to establish the proper bearing,
- a vertical bend center, in the Extraction Stub, to bend the beam down toward the Pre-target enclosure,
- and a second vertical bend center, in the Pre-target enclosure, to establish the proper pitch to Soudan.

In addition to these bend centers 10 quadrupoles are required for transport and final focus. Besides these elements, the normal complement of beam diagnostics, trim magnets, and support equipment are required.

The current "primary beam" beamline design is based upon a zero targeting angle for producing a wide-band beam (WBB). A horn system would be utilized to collect and focus the secondary beam (discussed in Chapter 3). An option for an alternate target scheme using a non-zero (-14 mr) vertical targeting angle has been included in the design. This option would produce a narrow-band secondary beam (NBB) requiring a lithium lens system for collection of the secondaries (discussed in Chapter 3). The conversion of the primary beamline between the WBB and NBB options is simple and straight forward (i.e. the elevation of the pre-target beamline is shifted by $\approx$0.3 m (11.3 inches) utilizing special magnet stands). The current civil construction designs of the extraction enclosure, pre-target enclosure, and target enclosure are consistent with accommodating either the WBB

or the NBB design. The listings of the site coordinates for WBB and NBB beamline elements are shown in Appendices A and B.

2.2 Beamline description

Two ten foot MI extraction septa modules are located 270 degrees in phase upstream of the Main Injector quadrupole Q602 in the upstream section of the MI-60 RF straight section. These modules produce approximately 400 microradians of kick providing a 12 mm separation between the circulating and extracted beams at the face of the first Lambertson.

An elevation view of the MI and extraction channel and transport line inside the MI tunnel are shown in Figure 2.1. The extraction channel, which is similar in design to all other MI extraction channels [15] is located at quadrupole Q608 at the downstream end of the RF straight section. This extraction channel is composed of three MI Lambertsons, each producing a design bend of 6 mr, and a MI C-magnet producing a bend of 8.4 mr. These elements provide the vertical pitch of the extracted beam(line) required to clear the downstream MI quadrupole (Q609) and the following MI dipoles. The required strengths and currents of the Lambertsons and C-magnet circuits are listed in Table 2.1.

The first magnetic element in the transport line following the extraction C-magnet is a defocusing quadrupole (3Q60) just upstream of MI Q609. This quadrupole is followed by a 7.3 m (24 ft) drift allowing the trajectory to rise to 47.5 cm (18.7 inches) above the MI centerline before the next magnetic element. The first dipole string is made up of seven EPB dipoles , denoted as B1(A-G), and runs at approximately 1500 Amps. This dipole string maintains its footprint over the MI, places the beamline on the proper horizontal trajectory to Soudan, and levels the vertical trajectory to clear the Tevatron antiproton injection beamline (A150 beamline) approximately 54 m (177 feet) downstream. Again, Table 2.1 lists the strengths and currents for this dipole string (circuit 3) as well as the roll angles of each dipole. A pure vertical bend is denoted by a 90 degree roll angle.

The last magnetic elements in the MI tunnel are a pair of quadrupoles located in the middle of the MI half cell 611 and centered over the MI centerline. A 54 m (177 ft) drift transports the beam from this point to the entrance of the extraction stub.

After the beam crosses the A150 beamline it enters the extraction stub. Figure 2.2 shows an elevation view of the MI extraction stub with the location of the beamline elements. A quadrupole doublet, at the entrance of the stub, produces a nearly parallel beam while maintaining reasonable beam sizes through the following dipole string. This dipole string is comprised of four recycled B2 dipoles from the Main Ring, denoted as B2(A-D), which are rolled 90 degrees to produce the nominal vertical pitch (-104.59 mr) to the pre-target enclosure. A second quadrupole doublet following the dipole string again produces a nearly parallel to slightly converging beam for transport through the $\approx$ 110 m (360 foot) beam pipe to the pre-target enclosure.

The elevation of the beamline as it exits the extraction stub is 215.6 m (707.1 feet), approximately 2.6 m (8.5 feet) below the MI centerline. To provide the flexibility for a NBB, the vertical angle is reduced by 2 mr. This raises the trajectory by 6.86 cm (2.7 inches) at the exit of the extraction stub and 28.7 cm (11.3 inches) at the entrance to the pre-target enclosure.

Circuit	Magnet(s)	Type	Roll degrees	Strength kG	Approx. Current kA
1	060(A-C)	MI lam	90	8.58	1.68
2	061	MI cmg	90	10.03	2.73
3	B1(A-B)	EPB	0.0	-14.05	-1.5
	B1(C-D)	EPB	5.1	-14.05	-1.5
	B1(E-G)	EPB	61.0	-14.05	-1.5
4	B2(A-D)	B2	90.0	-17.24	-4.37
5	B3(A-D)	EPB	90.0	15.18	1.69
6	B4(A-B)	EPB	90.0	0.0	-0.92**

**NOTE: This value of current is for 14 mr bend, 9.2 kG field with use in the NBB option only.

Table 2.1: Nominal Dipole Strengths for Wide Band Beam

The pre-target hall is located $\approx$ 110 m (360 feet) downstream of the MI-60 extraction stub. The average elevation of the beamline at the entrance to the pre-target enclosure is 204.35 m (670.27 feet), 11.2 m (36.83 feet) below the extraction stub beamline elevation. The arrangement of magnetic elements in the pre-target hall will allow their configuration to satisfy the constraints of the WBB and NBB geometries. Only one configuration is installed at any time. The configuration of the elements in the pre-target hall for both beam lines is shown in Figure 2.3. In this figure, the last two bends (unshaded rectangles) before the target are used only for the NBB and will not be installed in the WBB configuration.

For the WBB, the beam enters the pre-target hall at an elevation 204.2 m (669.80 feet) and a vertical pitch of -104.59 mr (-5.99 degrees). This pitch is reduced to $\approx$ -58.36 mr, the required pitch to Soudan, by a string of 4 vertically bending EPB dipoles. This dipole string runs at $\approx$ 1700 Amps (Table 2.1). There are no other bending elements (with exception of dipole trim magnets) in the WBB beamline. The target for the WBB is at an elevation of 199.6 m (654.8 feet) and installed at the same -58.36 mr pitch. All subsequent optics and decay tunnel follow this same pitch. This places the dump (800 m or 2625 feet downstream of the target) at a depth of $\approx$ 73.2 m (240 feet) and the experiment at a depth of $\approx$ 82.3 m (270 feet).

The NBB beamline enters the pre-target hall at an elevation of 204.5 m (670.74 feet) and a vertical pitch of -102.59 mr (-5.88 degrees). This pitch is reduced to $\approx$ -58.36 mr by the same set of 4 EPB dipoles as used in the WBB. The last quadrupole Q10, used for establishing the final focus of the beam on target, follows this bend center. In order to produce the -14 mr vertical angle on target, an independent bend circuit (circuit 6) is installed as close to the target as possible (still leaving room for the target shield and diagnostics). For the NBB option the target is raised to 199.9 m (655.67 feet) (26.52 cm or 10.44 in above the location of the target in the WBB). The position of this circuit must allow the secondary beamline to remove the offset and angle with respect to the WBB, such that the resultant secondaries end up following the same trajectory into the decay pipe as the WBB. There is no change

to the targeting optics between the WBB and the NBB option. There is no change to the decay pipe, dump, or experimental hall locations.

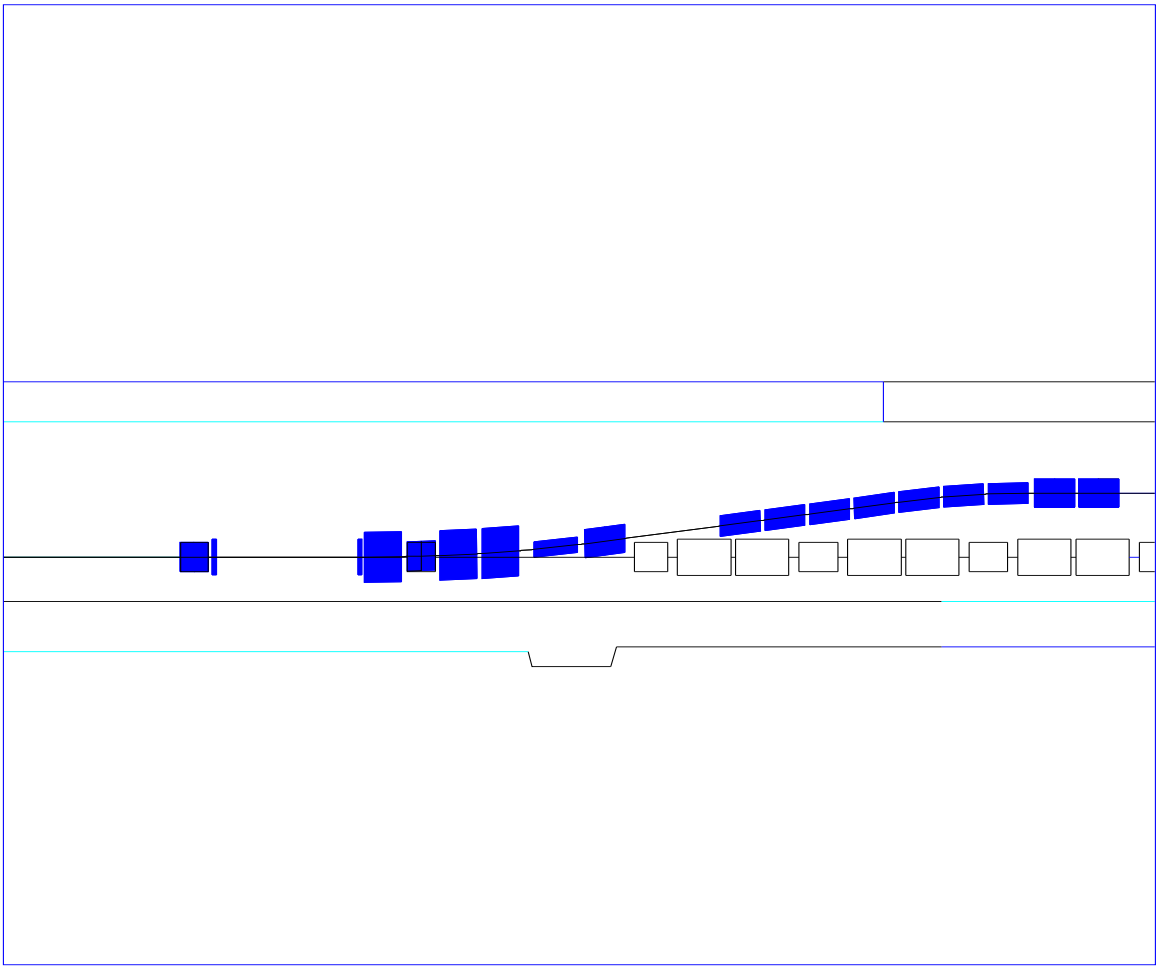

Figure 2.1: Elevation view of the NuMI extraction beamline (top) and the MI ring. The MI quadrupole 608 is located between the first two (of three) extraction lambertsons (large boxes). Vertical scale is exaggerated.

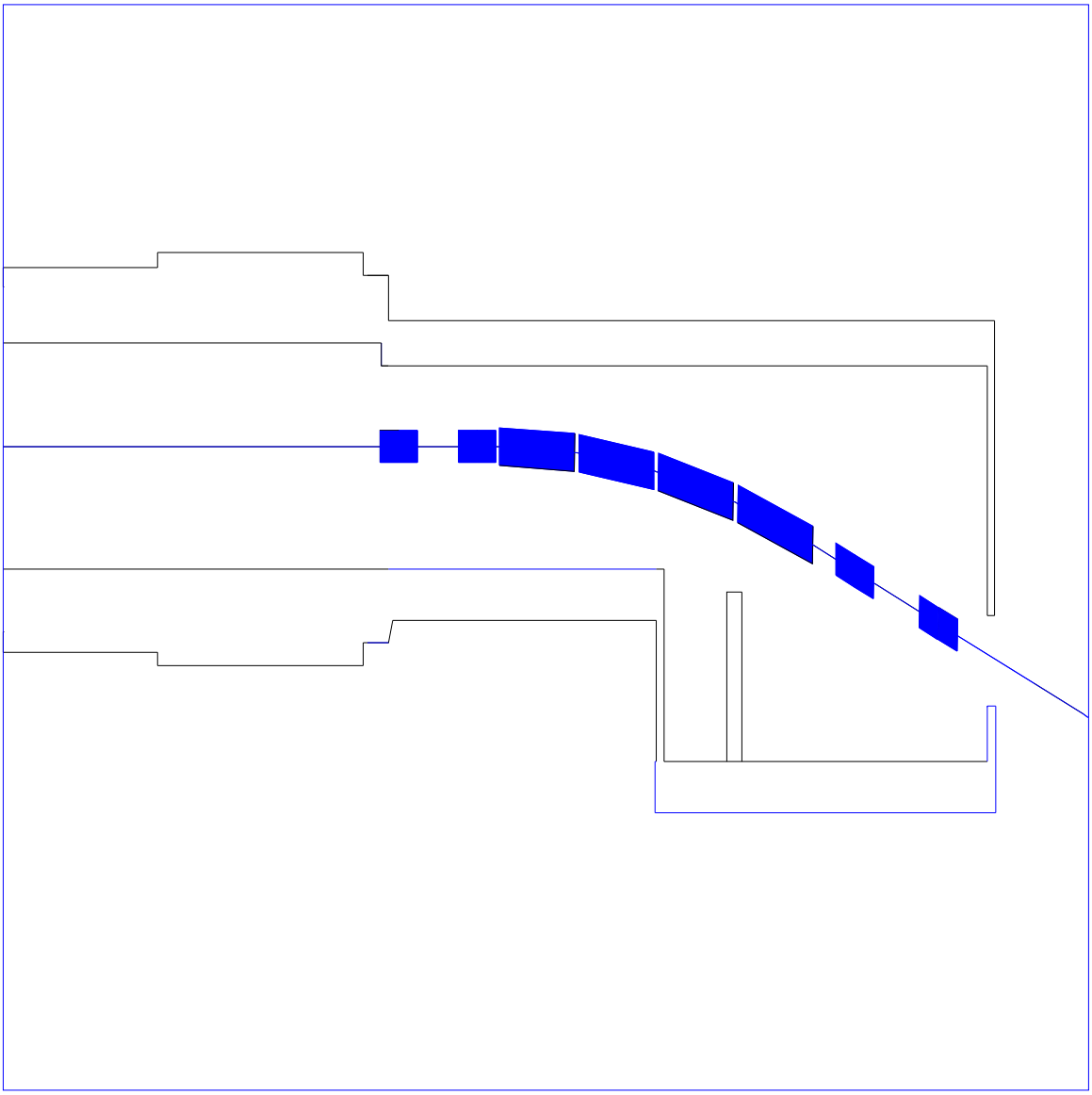

Figure 2.2: Elevation view of the NuMI beamline in the Extraction Stub. Vertical scale is exaggerated.

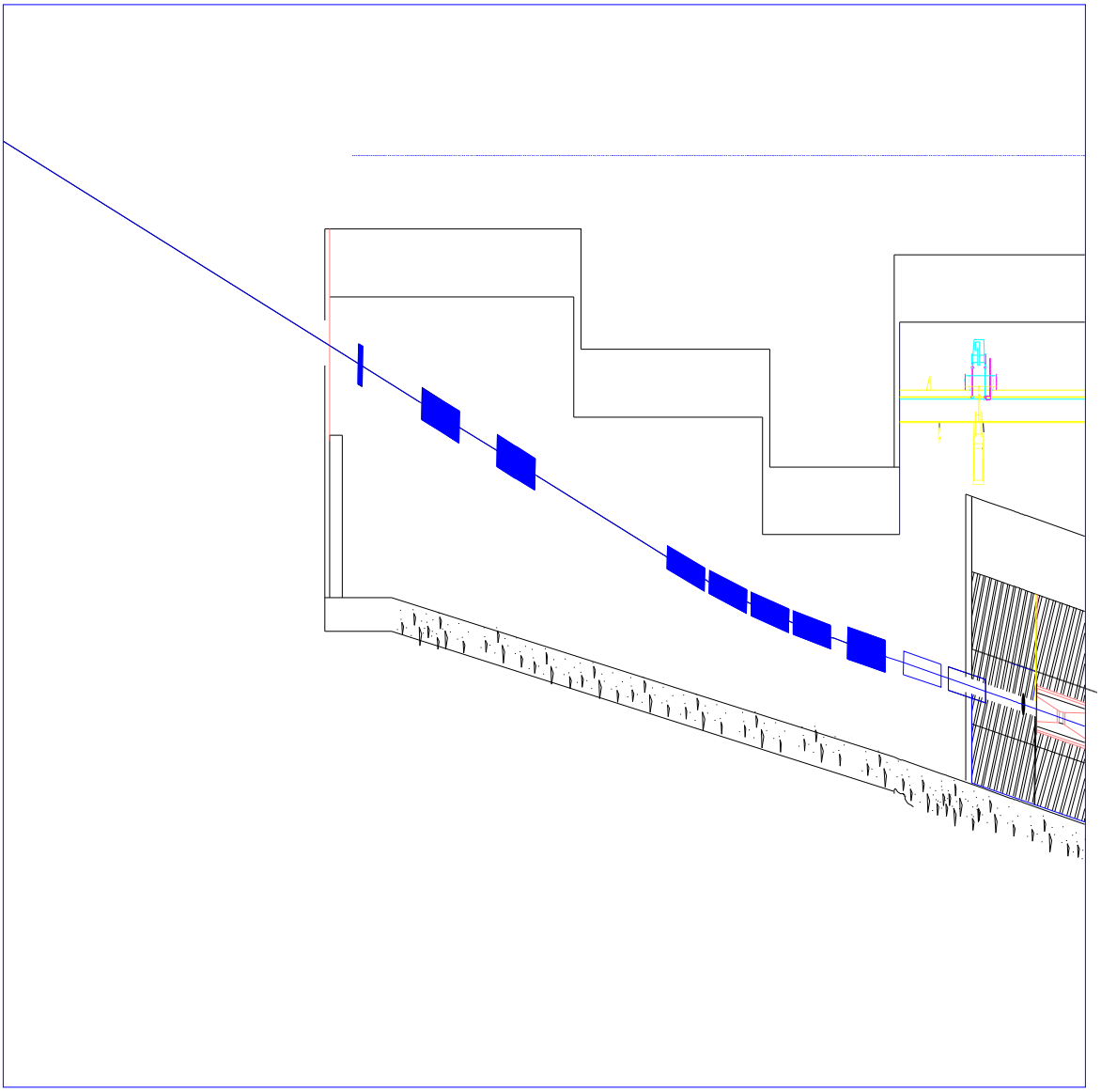

Figure 2.3: Elevation view of the Pre-target area showing the WBB primary beamline (shaded). The last two (unshaded) magnets, B6(A,B), before the target are included in the NBB option and are not installed in the WBB beamline. Vertical scale is exaggerated.

2.3 Beamline optics

Preliminary modeling of the extraction utilized the same 53rd harmonic quadrupole family (with opposite polarity) as used in MI-52 resonant extraction for test beams [15]. The air-core Quadrupole Extraction Regulation (QXR) circuit is pulsed in a half-sine wave to produce a spill of roughly 1 ms in duration as shown in Figure 2.4 [16].

For this design, an initial normalized emittance at 120 GeV/c prior to extraction is assumed to be 30 π-mm-mr in both planes. An ensemble of 1000 particles has been tracked through the MI during extraction [16]. Figure 2.5 shows the normalized phase space of the the beam midway through extraction at the septa and the entrance to the first Lambertson in the extraction channel. The momentum spread for this data set was assumed to be zero. This is a good approximation since the contribution to the beam size due to the momentum spread is small compared to the transverse beam size. For an RF voltage of 400 kV and a longitudinal emittance of 0.25 eV-sec the momentum spread ($\Delta p/p$) is approximately $\pm 0.04\%$.

The septa wires are assumed to be 16 mm to the inside of the MI centerline. The closed orbit offset of the extracted phase space at the entrance to the extraction channel is removed and the resultant taken as the initial phase space distribution for the beamline. This phase space is tracked through the beamline to the target and dump with the program MAD [17] to determine the resultant beam distribution on the target and dump.

The extracted phase space distribution is matched to a phase space ellipse of the nominal MI optics, determined by the Courant-Snyder parameters, at the entrance to the first Lambertson. This phase space ellipse is transported through the beamline to determine the minimum aperture requirements. The phase space of the extracted beam (from tracking), nominal MI Courant-Snyder lattice functions, phase space ellipse (corresponding to a 95% normalized horizontal and vertical emittance, ϵ_x^N and ϵ_y^N, of 15 and 30 π-mm-mr, respectively), and the square root of the sigma ($\sqrt{\sigma_{i,j}}$) and correlation ($r_{i,j}$) matrices for the extracted beam at the face of the first extraction Lambertson are shown in Figure 2.6.

The horizontal beam distribution resulting from the resonant extraction is smaller in both x and x' because the septa wires and finite step size create a hard edge in these dimensions. The resultant vertical extracted phase space remains a gaussian matched to the nominal MI optics phase space, as expected.

The calculation of the beam optics for the transport line utilizes a gaussian beam with ϵ_x^N and ϵ_y^N of 15 and 30 π-mm-mr, respectively. This assures that the horizontal beam size everywhere will be less than that predicted by $\sigma(11) = \sqrt{\epsilon_x \beta_x}$ due to hard edge aspect of resonant extraction.

The lattice functions for the transport line to the target are shown in Figure 2.7. Beam sizes are easily scaled from this using $\sigma(11) = \sqrt{\epsilon_x}\sqrt{\beta_x}$. Examination of the horizontal lattice functions shows that for $\epsilon_x^N = 15\pi$-mm-mr ($\epsilon_x = .117\pi$-mm-mr) the maximum horizontal beam size of ± 8 mm occurs at Q9 where $\sqrt{\beta_x}$=$23m^{1/2}$ The quadrupole gradients for this nominal tune, which produce an $\approx \pm 1$ mm spot size on target, are listed in Table 2.2.

The final target optics consist of three 3Q120 quadrupoles to focus the beam both horizontally and vertically. The distance between the last quadrupole, Q10, and the target is $\approx$ 10 m (33 feet). The spot size on the target is not only a function of the gradients in these quadrupoles, but also the x,x',y, and y' at the entrance to the triplet. Therefore, in addition

Magnet	Type	Strength kG/m
Q1	3Q60	-144.7
Q2	3Q60	139.9
Q3	3Q60	-107.4
Q4	3Q60	-107.4
Q5	3Q60	107.4
Q6	3Q60	53.8
Q7	3Q60	-69.2
Q8	3Q120	-84.8
Q9	3Q120	103.3
Q10	3Q120	-113.0

Table 2.2: Nominal Quadrupole Strengths for Wide Band Beam.

to the triplet, the last two quadrupoles in the extraction stub enclosure, Q6 and Q7, are adjusted. Beam half-sizes $\sqrt{\sigma_{11}}$ and $\sqrt{\sigma_{33}}$ through the pre-target hall for various spot sizes on target are shown in Figure 2.8. The six cases are labeled by the resultant Courant-Snyder parameters at the midpoint of the target. The target beam sizes are simply given by $\sqrt{\epsilon\beta}$. This parameterization gives maximum expected beam sizes and shows the behavior at the final focus.

The minimum focus is determined by the available quadrupole strength (in Q6), and by the x,y beam divergence after the target. Assuming a ± 0.5 meter spot size on the the face of the dump is acceptable, the maximum divergence allowed for the primary beam is $\approx 625\mu$r. Based upon this criterion, the minimum vertical spot size on target, is $\approx \pm 0.4$ mm. In Figure 2.8, the bottom row of configurations keep the vertical beam size constant while varying the horizontal beam size showing the independent control of the x,y beam size on target. The hatched rectangle represents the location on the segmented target (1.56 meters overall length). The target beam sizes, the vertical beam size at the face of the dump, and the required gradients in the last five quadrupoles corresponding to these beam sizes are shown in Table 2.3.

For each of these quadrupole settings, the extracted phase space was tracked through the beamline. The resultant beam size on the 2 mm radius target (dashed circle) are shown in Figure 2.9. The beam sizes resulting from tracking the extracted phase space range from ± 0.4 mm to ± 2 mm at the longitudinal center of the target. The beam sizes at the dump 800 meters downstream of the target, for the scenarios shown in Figures 2.8 and 2.9 vary from ± 0.5 meter to ± 0.07 meter in the vertical dimension and are well contained within the 2 meter diameter decay pipe.

Magnet	Strength [kG/m]					
$\beta_x : \beta_y[m]$	1.5:0.6	7.5:2.5	15:5	15:30	50:30	150:30
Beam size [mm]	±(.4 x .4)	±(.7 x .7)	±(1 x 1)	±(1 x 2)	±(1.2 x 2)	±(2 x 2)
Dump σ_y [m]	±0.50	±0.25	±0.175	±0.07	±0.07	±0.07
Q6	18.8	33.5	53.8	68.1	67.3	56.9
Q7	-57.9	-46.6	-69.2	-82.4	-82.4	-76.3
Q8	-72.6	-75.6	-84.8	-96.7	-97.7	-98.7
Q9	101.4	99.2	103.3	105.7	100.6	99.6
Q10	-130.8	-107.4	-113.0	-54.6	-57.7	-55.2

Table 2.3: Quadrupole Strengths verses beam size [mm] on target.

Figure 2.4: Distribution of particles during 1 ms resonant extraction.

Figure 2.5: Normalized phase space of circulating and extracted beam midway through extraction.

```
 momentum:  120.000000 [gev/c]
 hor emit:  15.000000 [pi-mm-mr]
 ver emit:  30.000000 [pi-mm-mr]
 sig p: 0.400000 [E-3]
 betax: 41.320000  alphax: -2.080000  etax: 0.100000  etaxp: 0.003000
 betay: 16.350000  alphay: 0.900000  etay: 0.000000  etayp: 0.000000
 OUTPUT:
 Normalized emittance: HOR 0.117282   VER 0.234564
 Sigma matrix:

2.201748
0.493958 0.122963
0.000000 0.000000 1.958347
0.000000 0.000000 0.459464 0.161143
0.000000 0.000000 0.000000 0.000000 0.000000
0.126491 0.021909 0.000000 0.000000 0.000000 0.400000

 Correlation matrix:

0.901238
0.000000  0.000000
0.000000  0.000000  -0.668965
0.000000  0.000000  0.000000  0.000000
0.018167  0.009759  0.000000  0.000000  0.000000
```

Figure 2.6: Comparison between resonant extraction beam distribution and nominal MI lattice optics at the face of the first extraction Lambertson.

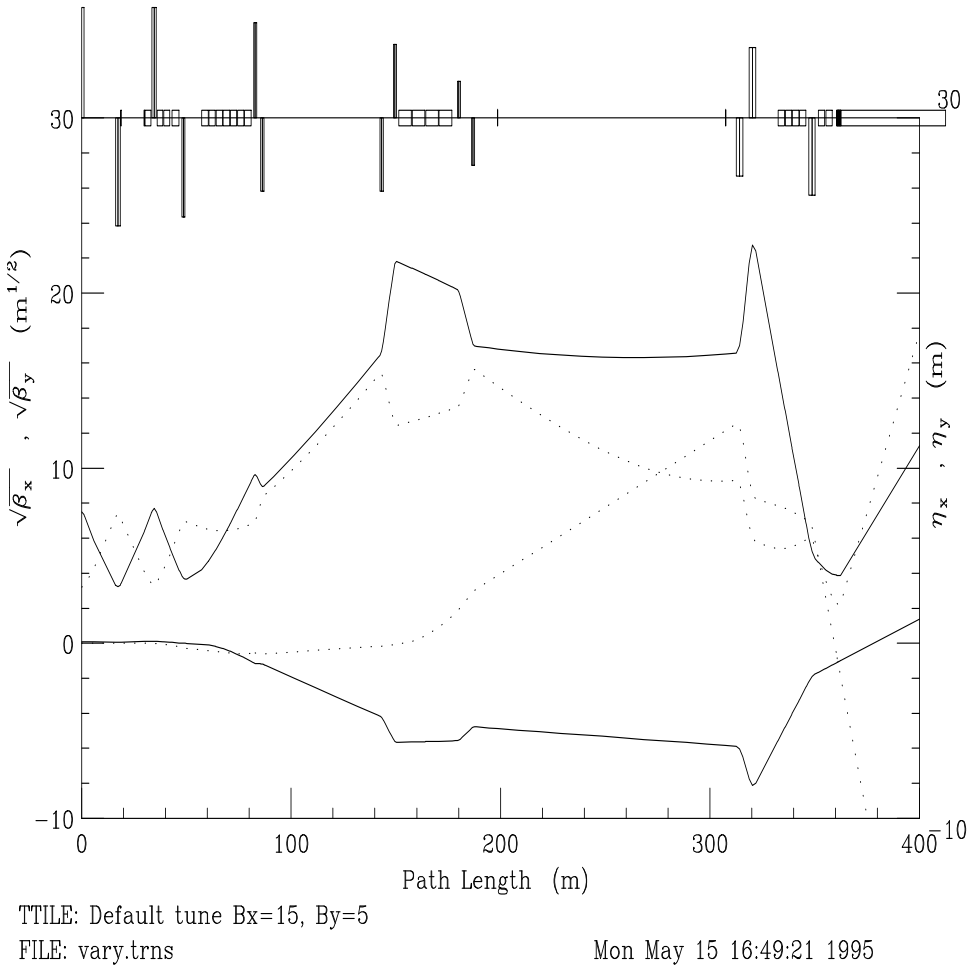

Figure 2.7: Lattice functions of primary beamline to target. Target is located at 360 m.

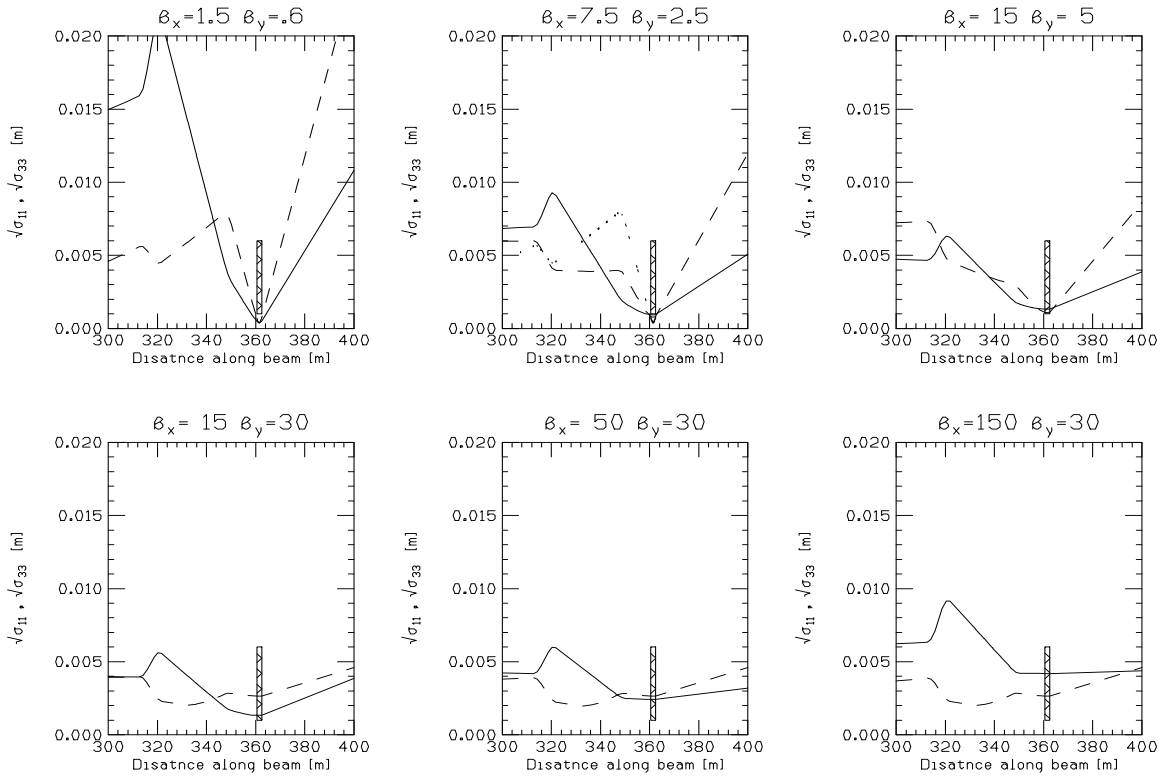

Figure 2.8: Beam sizes through the pre-target hall corresponding to various Courant-Snyder parameters. The first two quadrupoles in the triplet are located at s = 320 meters with the third quadrupole at s = 350 meters. The vertical beam size is shown as the dashed line.

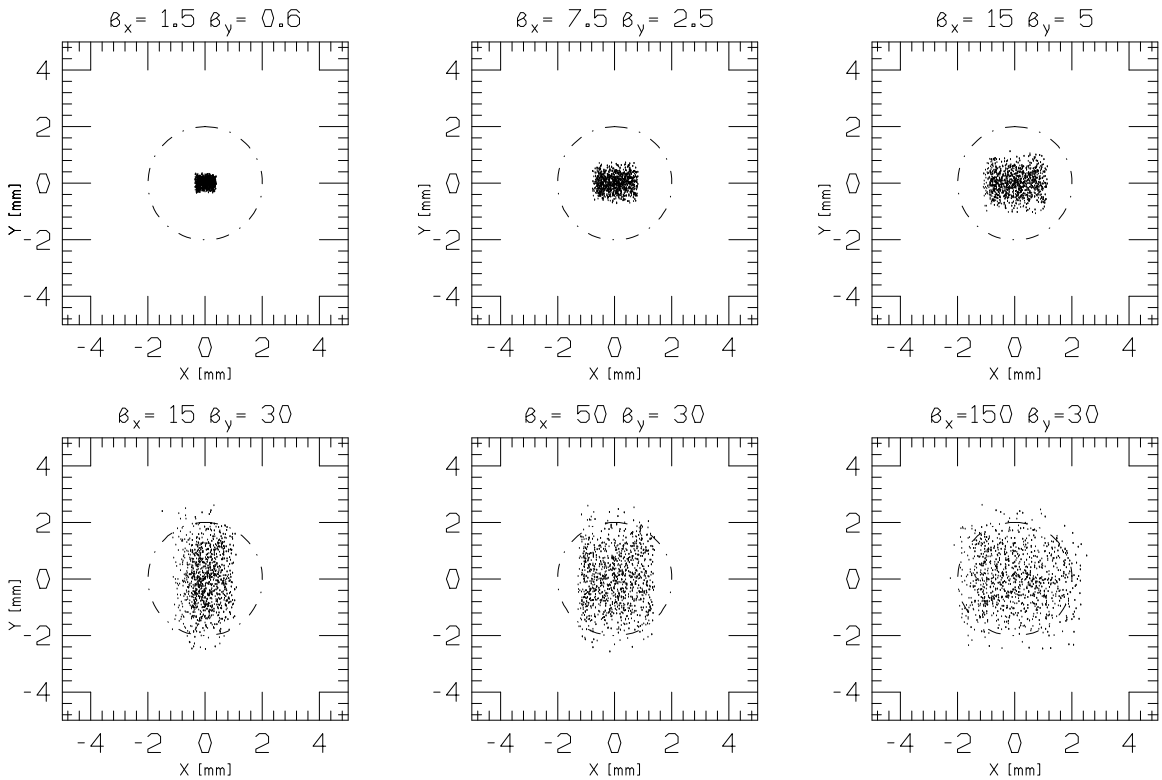

Figure 2.9: Beam size at the longitudinal midpoint of the target from tracking an extracted phase space distribution of roughly 1000 particles through six optical solutions. The dashed circle represents a 2 mm radius target.

Appendix A: Coordinates of Beamline elements for the Wide-Band Beam primary transport.

```
Program ces (A Construction Engineering Survey format) (11/26/91)   Tue Apr 18 15:46:57 1995
 Site coordinates for beamline:  input_ces_v2
 NOTES: Coordinates are given for the entrance of the device in DUSAF coordinate system.
        Site +x-axis (EAST); site +y-axis (NORTH);  Site z-axis (ELEVATION)
        Positive bearing is counter clockwise with respect to site EAST.
        Pitch is the vertical angle about the x-y plane.
```

line	location	typ_code	distance [ft]	x [ft]	y [ft]	z [ft]	brng [deg]	pitch [deg]	yaw [deg]
0000	S1_BHL	marker	0.00000	101468.34139	97163.81440	715.72409	148.76849	0.00000	0.00000
0001	Q606D	3Q84-2	0.00000	101468.34139	97163.81440	715.72409	148.76849	0.00000	0.00000
0002	Q607	3Q84-2	53.22115	101422.83308	97191.40942	715.72409	148.76849	0.00000	0.00000
0003	Q607	3Q84-2	56.72115	101419.84034	97193.22415	715.72409	148.76849	0.00000	0.00000
0004	C_607	HIVC	61.22114	101415.99248	97195.55738	715.72409	148.76849	0.00000	0.00000
0005	C_608	HIHC	97.58931	101384.89480	97214.41420	715.72409	148.76849	0.00000	0.00000
0006	B900A	HILAH	99.25597	101383.46967	97215.27834	715.72409	148.80602	0.16759	0.00000
0007	Q608	3Q84-2	109.94230	101374.32793	97220.81232	715.75979	148.84355	0.33518	-0.00000
0008	Q608	3Q84-2	113.44229	101371.33285	97222.62311	715.78026	148.84355	0.33518	-0.00000
0009	B900B	HILAH	118.10895	101367.33939	97225.03750	715.80759	148.86045	0.50649	-0.00000
0010	B900C	HILAH	128.62865	101358.33570	97230.47693	715.90457	148.88366	0.84941	-0.00057
0011	B901A	CHG_1	141.58958	101347.24078	97237.17367	716.10802	148.87248	1.26108	-0.00057
0012	Q1	3Q60-2	156.84431	101334.18664	97245.05846	716.46159	148.85501	1.50115	0.00000
0013	Q1	3Q60-2	159.34430	101332.04773	97246.35101	716.52708	148.85501	1.50115	0.00000
0014	B1A	EPB	188.19848	101307.36097	97261.26932	717.28301	149.16154	1.50115	0.00000
0015	B1B	EPB	199.36515	101297.77319	97266.98621	717.57553	149.77461	1.50086	-0.01604
0016	B1C	EPB	210.53186	101288.12482	97272.60017	717.86805	150.38652	1.52779	-0.03209
0017	B1D	EPB	221.69854	101278.41716	97278.11073	718.16631	150.99730	1.58194	-0.04813
0018	B1E	EPB	232.86525	101268.65160	97283.51741	718.47514	151.45108	1.34072	-0.06532
0019	B1F	EPB	244.03193	101258.84387	97288.85001	718.73091	151.74759	0.80443	-0.07219
0020	B1G	EPB	255.19864	101249.00702	97294.13268	718.88222	152.04409	0.26814	-0.07620
0021	Q2	3Q60-2	269.31774	101236.53063	97300.74211	718.92904	152.19249	0.00000	-0.07792
0022	Q2	3Q60-2	271.81773	101234.31932	97301.90835	718.92904	152.19249	0.00000	-0.07792
0023	Q3	3Q60-2	280.31771	101226.80093	97305.87363	718.92904	152.19249	0.00000	-0.07792
0024	Q3	3Q60-2	282.81771	101224.58964	97307.03990	718.92904	152.19249	0.00000	-0.07792
0025	Q4	3Q60-2	467.43282	101061.29401	97393.16355	718.92914	152.19249	0.00000	-0.07792
0026	Q4	3Q60-2	469.93282	101059.08272	97394.32982	718.92914	152.19249	0.00000	-0.07792
0027	Q5	3Q60-2	488.27530	101042.85845	97402.88666	718.92914	152.19249	0.00000	-0.07792
0028	Q5	3Q60-2	490.77530	101040.64716	97404.05289	718.92914	152.19249	0.00000	-0.07792
0029	B2A	B2	496.69195	101035.41374	97406.81303	718.92914	152.19134	-0.74914	-0.07792
0030	B2B	B2	517.77580	101016.76722	97416.64785	718.63829	152.18934	-2.24714	-0.07792
0031	B2C	B2	538.85968	100998.13413	97426.47641	717.79637	152.18733	-3.74514	-0.07792
0032	B2D	B2	559.94353	100979.52724	97436.29200	716.40401	152.18533	-5.24342	-0.07792
0033	Q6	3Q60-2	588.46122	100954.42030	97449.53781	713.68607	152.18447	-5.99257	-0.07792
0034	Q6	3Q60-2	590.96122	100952.22126	97450.69801	713.42508	152.18447	-5.99257	-0.07792
0035	Q7	3Q60-2	610.67647	100934.87933	97459.84747	711.36688	152.18447	-5.99257	-0.07792
0036	Q7	3Q60-2	613.17646	100932.68029	97461.00764	711.10589	152.18447	-5.99257	-0.07792
0037	HERR	HIHC	651.49430	100898.97514	97478.79018	707.10567	152.18447	-5.99257	-0.07792
0038	PRETAR	HIHC	1008.83220	100584.65359	97644.62354	669.80115	152.18447	-5.99257	-0.07792
0039	Q8	3Q120-2	1025.73637	100569.78433	97652.46844	668.03643	152.18447	-5.99257	-0.07792
0040	Q8	3Q120-2	1030.73636	100565.38624	97654.78884	667.51445	152.18447	-5.99257	-0.07792
0041	Q9	3Q120-2	1045.78049	100552.15313	97661.77052	665.94391	152.18447	-5.99257	-0.07792
0042	Q9	3Q120-2	1050.78048	100547.75504	97664.09089	665.42193	152.18447	-5.99257	-0.07792
0043	B3A	EPB	1091.00677	100512.37119	97682.75913	661.22246	152.18475	-5.66140	-0.07792
0044	B3B	EPB	1102.17348	100502.54237	97687.94462	660.12762	152.18561	-4.99906	-0.07792
0045	B3C	EPB	1113.34019	100492.70295	97693.13552	659.16128	152.18647	-4.33672	-0.07792
0046	B3D	EPB	1124.50687	100482.85422	97698.33111	658.32358	152.18733	-3.67466	-0.07792
0047	Q10	3Q120-2	1139.03775	100470.02701	97705.09767	657.41840	152.18790	-3.34378	-0.07792
0048	Q10	3Q120-2	1144.03774	100465.61213	97707.42657	657.12677	152.18790	-3.34378	-0.07792
0049	B4A	EPB	1153.89139	100456.91159	97712.01619	656.55207	152.18790	-3.34378	-0.07792
0050	B4B	EPB	1165.76145	100446.43060	97717.54505	655.85978	152.18790	-3.34378	-0.07792
0051	TAR	TAR	1182.73976	100431.43916	97725.45320	654.86952	152.18790	-3.34378	-0.07792
0052	TAR	TAR	1183.36312	100430.88874	97725.74352	654.83317	152.18790	-3.34378	-0.07792
0053	TAR	TAR	1183.98648	100430.33831	97726.03388	654.79682	152.18790	-3.34378	-0.07792
0054	TAR	TAR	1184.60984	100429.78792	97726.32423	654.76047	152.18790	-3.34378	-0.07792
0061	TAR	TAR	1188.97334	100425.93504	97728.35668	654.50597	152.18790	-3.34378	-0.07792
0062	TARTUB	TAR_TUBE	1189.30143	100425.64534	97728.50946	654.48681	152.18790	-3.34378	-0.07792
0063	DECAY	DECAY	1353.34309	100280.80039	97804.91676	644.91925	152.18790	-3.34378	-0.07792
0064	DUHP	DUHP	3813.96809	98108.12616	98951.02579	501.40579	152.18790	-3.34378	-0.07792
0065	SHIELD	SHIELD	3836.93393	98087.84785	98961.72281	500.06632	152.18790	-3.34378	-0.07792
0066	EXP	EXP	4361.86726	97624.34402	99206.22606	469.45011	152.18790	-3.34378	-0.07792

Appendix B: Coordinates Beamline elements for the Narrow-Band Beam primary transport.

Program ces (A Construction Engineering Survey format) (11/26/91) Tue Apr 18 16:18:06 1995
Site coordinates for beamline: input_ces_v2
NOTES: Coordinates are given for the entrance of the device in DUSAF coordinate system.
Site +x-axis (EAST); site +y-axis (NORTH); Site z-axis (ELEVATION)
Positive bearing is counter clockwise with respect to site EAST.
Pitch is the vertical angle about the x-y plane.

line	location	typ_code	distance [ft]	x [ft]	y [ft]	z [ft]	brng [deg]	pitch [deg]	yaw [deg]
0000	S1_BHL	marker	0.00000	101468.34139	97163.81440	715.72409	148.76849	0.00000	0.00000
0001	Q606D	3Q84-2	0.00000	101468.34139	97163.81440	715.72409	148.76849	0.00000	0.00000
0002	Q607	3Q84-2	53.22115	101422.83308	97191.40942	715.72409	148.76849	0.00000	0.00000
0003	Q607	3Q84-2	56.72115	101419.84034	97193.22415	715.72409	148.76849	0.00000	0.00000
0004	C_607	HIVC	61.22114	101415.99248	97195.55738	715.72409	148.76849	0.00000	0.00000
0005	C_608	HIHC	97.58931	101384.89480	97214.41420	715.72409	148.76849	0.00000	0.00000
0006	B900A	HILAH	99.25597	101383.46967	97215.27834	715.72409	148.80602	0.16759	0.00000
0007	Q608	3Q84-2	109.94230	101374.32793	97220.81232	715.75979	148.84355	0.33518	-0.00000
0008	Q608	3Q84-2	113.44229	101371.33285	97222.62311	715.78026	148.84355	0.33518	-0.00000
0009	B900B	HILAH	118.10895	101367.33939	97225.03750	715.80759	148.86045	0.50649	-0.00000
0010	B900C	HILAH	128.62865	101358.33570	97230.47693	715.90457	148.88366	0.84941	-0.00057
0011	B901A	CHG_1	141.58958	101347.24078	97237.17367	716.10802	148.87248	1.26108	-0.00057
0012	Q1	3Q60-2	156.84431	101334.18664	97245.05846	716.46159	148.85501	1.50115	0.00000
0013	Q1	3Q60-2	159.34430	101332.04773	97246.35101	716.52708	148.85501	1.50115	0.00000
0014	B1A	EPB	188.19848	101307.36097	97261.26932	717.28301	149.16154	1.50115	0.00000
0015	B1B	EPB	199.36515	101297.77319	97266.98621	717.57553	149.77461	1.50086	-0.01604
0016	B1C	EPB	210.53186	101288.12482	97272.60017	717.86805	150.38652	1.52779	-0.03209
0017	B1D	EPB	221.69854	101278.41716	97278.11073	718.16631	150.99730	1.58194	-0.04813
0018	B1E	EPB	232.86525	101268.65160	97283.51741	718.47514	151.45108	1.34072	-0.06532
0019	B1F	EPB	244.03193	101258.84387	97288.85001	718.73091	151.74759	0.80443	-0.07219
0020	B1G	EPB	255.19864	101249.00702	97294.13268	718.88222	152.04409	0.26814	-0.07620
0021	Q2	3Q60-2	269.31774	101236.53063	97300.74211	718.92904	152.19249	0.00000	-0.07792
0022	Q2	3Q60-2	271.81773	101234.31932	97301.90835	718.92904	152.19249	0.00000	-0.07792
0023	Q3	3Q60-2	280.31771	101226.80093	97305.87363	718.92904	152.19249	0.00000	-0.07792
0024	Q3	3Q60-2	282.81771	101224.58964	97307.03990	718.92904	152.19249	0.00000	-0.07792
0025	Q4	3Q60-2	467.43282	101061.29401	97393.16355	718.92914	152.19249	0.00000	-0.07792
0026	Q4	3Q60-2	469.93282	101059.08272	97394.32982	718.92914	152.19249	0.00000	-0.07792
0027	Q5	3Q60-2	488.27530	101042.85845	97402.88666	718.92914	152.19249	0.00000	-0.07792
0028	Q5	3Q60-2	490.77530	101040.64716	97404.05289	718.92914	152.19249	0.00000	-0.07792
0029	B2A	B2	496.69195	101035.41374	97406.81303	718.92914	152.19134	-0.73482	-0.07792
0030	B2B	B2	517.77580	101016.76716	97416.64788	718.64384	152.18934	-2.20417	-0.07792
0031	B2C	B2	538.85962	100998.13350	97426.47670	717.81802	152.18733	-3.67352	-0.07792
0032	B2D	B2	559.94347	100979.52504	97436.29309	716.45224	152.18533	-5.14316	-0.07792
0033	Q6	3Q60-2	588.46116	100954.41367	97449.54112	713.78614	152.18447	-5.87797	-0.07792
0034	Q6	3Q60-2	590.96115	100952.21417	97450.70155	713.53010	152.18447	-5.87797	-0.07792
0035	Q7	3Q60-2	610.67640	100934.86860	97459.85288	711.51114	152.18447	-5.87797	-0.07792
0036	Q7	3Q60-2	613.17640	100932.66910	97461.01331	711.25514	152.18447	-5.87797	-0.07792
0037	HERR	HIHC	651.49424	100898.95693	97478.79946	707.33113	152.18447	-5.87797	-0.07792
0038	PRETAR	HIHC	1008.83214	100584.56953	97644.66642	670.73744	152.18447	-5.87797	-0.07792
0039	Q8	3Q120-2	1025.73630	100569.69719	97652.51290	669.00634	152.18447	-5.87797	-0.07792
0040	Q8	3Q120-2	1030.73629	100565.29818	97654.83379	668.49430	152.18447	-5.87797	-0.07792
0041	Q9	3Q120-2	1045.78042	100552.06228	97661.81688	666.95369	152.18447	-5.87797	-0.07792
0042	Q9	3Q120-2	1050.78041	100547.66327	97664.13774	666.44168	152.18447	-5.87797	-0.07792
0043	B3A	EPB	1091.00671	100512.27201	97682.80975	662.32223	152.18475	-5.56113	-0.07792
0044	B3B	EPB	1102.17339	100502.44155	97687.99609	661.24654	152.18561	-4.92744	-0.07792
0045	B3C	EPB	1113.34010	100492.60105	97693.18752	660.29382	152.18647	-4.29375	-0.07792
0046	B3D	EPB	1124.50677	100482.75179	97698.38338	659.46417	152.18733	-3.66034	-0.07792
0047	Q10	3Q120-2	1139.03765	100469.92442	97705.15003	658.56151	152.18790	-3.34378	-0.07792
0048	Q10	3Q120-2	1144.03764	100465.50957	97707.47893	658.26988	152.18790	-3.34378	-0.07792
0049	B4A	EPB	1153.89129	100456.80903	97712.06855	657.69517	152.18762	-3.54432	-0.07792
0050	B4B	EPB	1165.76135	100446.33064	97717.59607	656.95485	152.18704	-3.94539	-0.07792
0051	TAR	TAR	1182.73969	100431.35088	97725.49838	655.76234	152.18676	-4.14592	-0.07792
0052	TAR	TAR	1183.36305	100430.80098	97725.78847	655.71729	152.18676	-4.14592	-0.07792
0053	TAR	TAR	1183.98641	100430.25107	97726.07856	655.67221	152.18676	-4.14592	-0.07792
0054	TAR	TAR	1184.60977	100429.70117	97726.36865	655.62717	152.18676	-4.14592	-0.07792
0061	TAR	TAR	1188.97328	100425.85184	97728.39929	655.31168	152.18676	-4.14592	-0.07792
0062	TARTUB	TAR_TUBE	1189.30136	100425.56244	97728.55198	655.28796	152.18676	-4.14592	-0.07792
0063	DECAY	DECAY	1353.34309	100280.80039	97804.91676	644.91925	152.18790	-3.34378	-0.07792
0064	DUMP	DUMP	3813.96809	98108.12616	98951.02579	501.40579	152.18790	-3.34378	-0.07792
0065	SHIELD	SHIELD	3836.93393	98087.84785	98961.72281	500.06632	152.18790	-3.34378	-0.07792
0066	EXP	EXP	4361.86726	97624.34402	99206.22606	469.45011	152.18790	-3.34378	-0.07792

Chapter 3

The Neutrino Beam Lines

The designs of the neutrino beams for the NuMI project are described in this chapter. Two types of beams have been designed: (a) a wide-band beam (WBB) where a pair of focusing horns are used to decrease the angular dispersion of a charged particle beam before a decay pipe in which a broad spectrum of neutrinos are produced; and, as a later addition, (b) a narrow-band beam (NBB) where the charged particles are focused by a lithium lens and undergo momentum selection so that the resulting neutrinos are quasi-dichromatic (different energies coming from π and K decay).

The NuMI neutrino beams are designed to share a common civil facility which is described in detail elsewhere[13]. Figure 3.1 shows the approximate layout of the neutrino beam facility. As described in the previous chapter, protons from the Main Injector are extracted at an angle of $\sim$ 104 (102) milliradians and enter the pre-target enclosure where they are bent to 58 (72) milliradians for the WBB (NBB) beam and strike the target at the middle of the pre-target/target hall. The resulting mesons are focused and subsequently decay to neutrinos within either the 50 m long target hall or in the 750 m long, 1 m radius decay pipe. A dump at the end of the 800 m decay region absorbs the non-interacting protons in the WBB and the mesons which have neither decayed nor interacted with the decay pipe walls. There is a rock shield of 150 m to absorb the muons that accompany the neutrinos and then the experimental hall where the E–803 (COSMOS) detector and the E–875 (MINOS) near detector are located. The dimensions shown on Figure 3.1 are approximate but show the relative distances involved in the neutrino facility.

We will discuss the design criteria for the two beams, the calculation of neutrino flux used to meet the design criteria, the detailed design of the WBB and NBB, including installation and replacement of failed components, and then the radiation shielding needs for the target and the two beams. The chapter will end with a description of our plans for operations, switching between the two beams and maintenance of the neutrino facility.

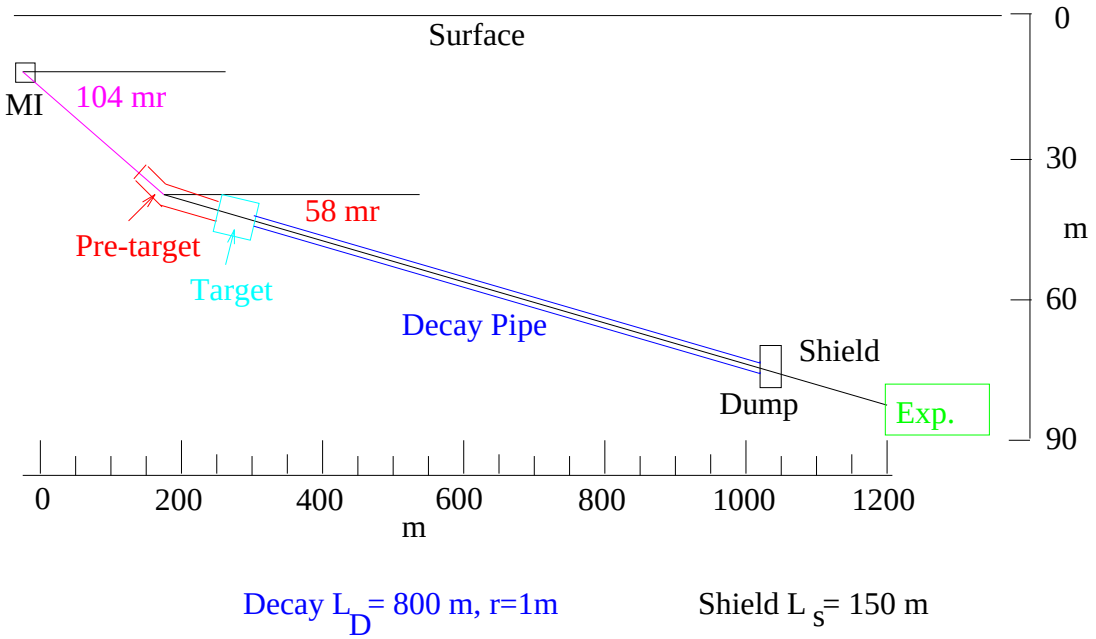

Figure 3.1: The approximate layout of the NuMI neutrino facility for E–803 (COSMOS) and E–875 (MINOS).

3.1 Beam Design Criteria

The goal for the design of the WBB is to simultaneously maximize the exposure of the short baseline experiment E–803 and the long baseline experiment E–875 to neutrinos with energies above the ν_τ charged current threshold of $\sim$ 5 GeV. The short baseline experiment requires a low and well understood background from $\overline{\nu}_\mu$[18] since $\overline{c}$ production and subsequent decay is a major background for the COSMOS experiment. Similarly, the long baseline experiment requires a low and well understood background from $\nu_e + \overline{\nu}_e$ which is a background in ν_e "appearance" experiments. The beam elements used to provide the neutrino flux should be reliable, capable of providing several million pulses of operation, and the cost should be reasonable.

The WBB as presently conceived is a double horn beam with horn currents of 160–170 kAmp. This provides a neutrino beam from sign selected parent mesons with minimal background. The CERN experience with horns has shown that horns satisfy the criteria of reliability and cost if properly designed. The detailed horn design is chosen to maximize the neutrino flux at a specific energy. For a neutrino oscillation search experiment one maximizes the product of the secondary particle production energy spectrum (which yields a corresponding neutrino energy spectrum) and the neutrino cross section. Figure 3.2a shows a sample secondary particle energy spectrum, Figure 3.2b illustrates the charge current (CC) ν_τ cross section as a function of energy and Figure 3.2c presents their product. For an exponentially falling spectrum the maximum of the product with the ν_τ cross section occurs at $\sim$ 20 GeV. So for neutrinos from kaons where the maximum neutrino energy $E_\nu^{max} = 0.96 \times E_K$ a selection of momentum at 25 GeV is desired and for neutrinos from pions where $E_\nu^{max} = 0.43 \times E_\pi$ a selection of momentum at 50 GeV is desired.

After the momentum ranges for the horns are chosen the desired magnetic field determines the shape of the horn, the length of the horn and the current in the horn. The interplay among these will be described in Section 3.3. However, the ν_μ flux from the final horn design folded in with the ν_τ cross section (see Figure 3.2b) is shown in Figure 3.3. The ν_τ event rate is enhanced at the energies of interest to COSMOS and MINOS, $E_{\nu_\tau} \geq 7$ GeV.

The design goals for the NBB are to maximize the event rate from the beam with a well understood ν_μ energy distribution and a minimized low-energy tail. The NBB needs a device which focuses a divergent beam into a parallel beam just as the WBB does. However, since the NBB has a minimized momentum spread, the chosen focusing device may have a smaller momentum range (compared to the WBB horn) over which it has good acceptance. A lithium lens satisfies the initial focusing requirements of the NBB and, as has been shown in the Fermilab anti-proton source, satisfies the other design criteria concerning reliability and cost. An additional design criteria for the NBB is that it has a tunable central beam energy. The NBB currently designed has a plan for changing the energy of the beam with minimal effort. The details of this will be described in Section 3.4.

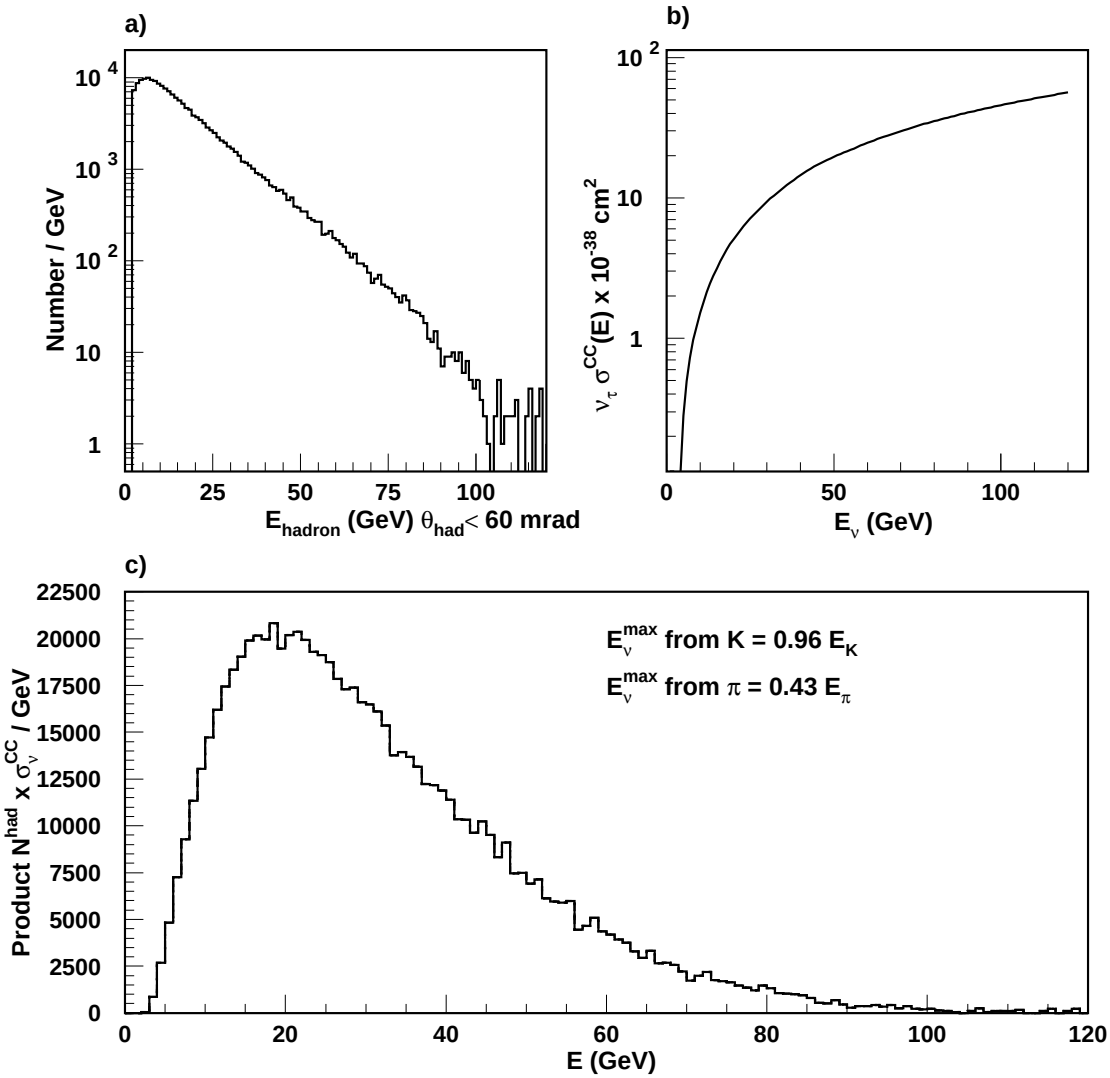

Figure 3.2: a) A sample secondary particle energy spectrum, b) the CC ν_τ cross section and c) the product of a) and b).

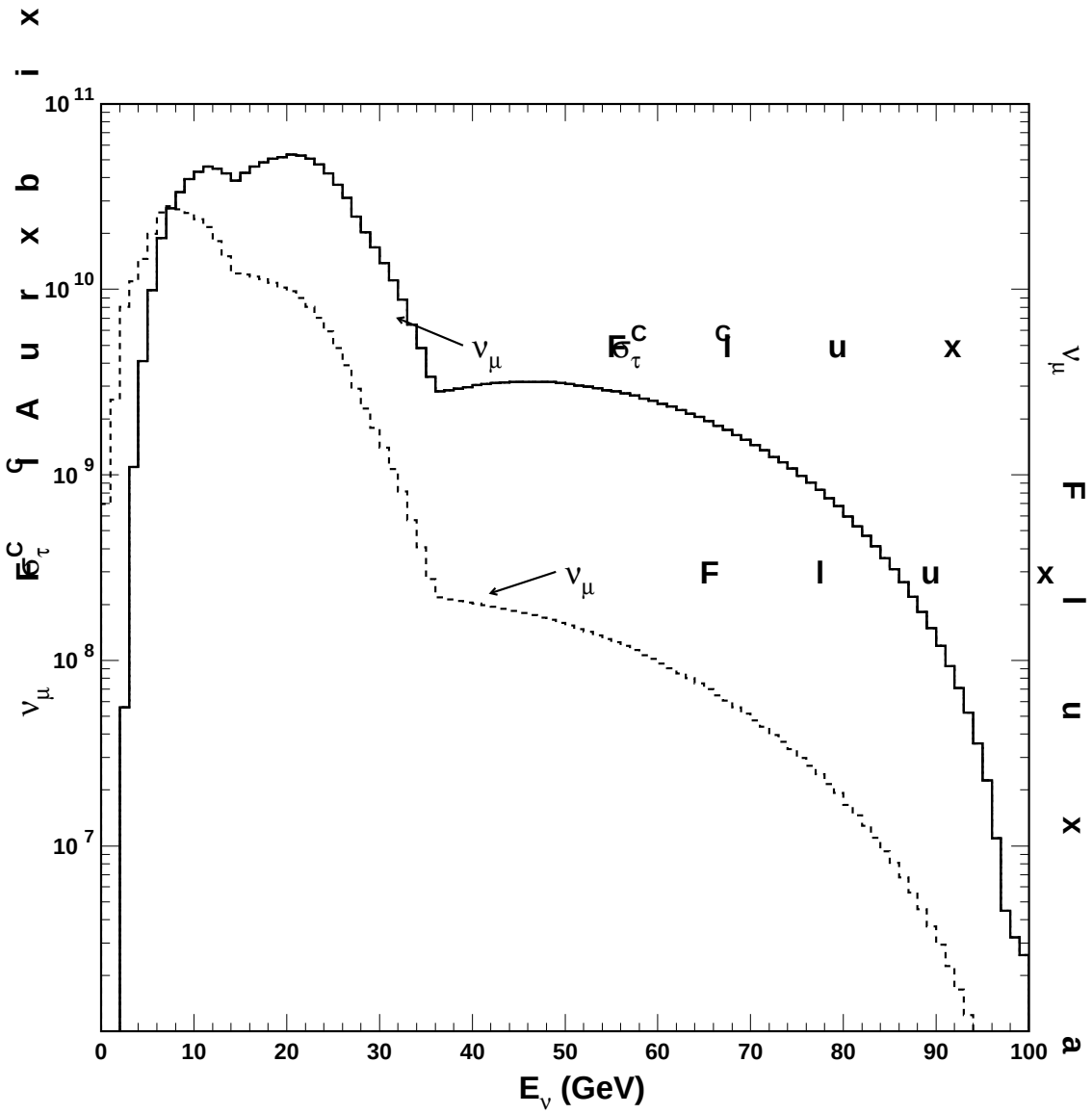

Figure 3.3: The CC ν_τ event rate shape (solid) obtained by multiplying the WBB ν_μ flux (dashed) by the ν_τ CC cross section shape.

3.2 Calculation of Neutrino Flux

We have used two programs with different capabilities and limitations to calculate neutrino flux. The use of two programs allows us to perform some cross checks of the results of our calculations. In this Section, we give a brief description of the calculational strategy of each program and summarize their strengths and weaknesses for our purposes.

The Fermilab neutrino beam program NUADA[19] is an analytic calculation using a parametrization of secondary hadron production[20] and decay kinematics which also includes absorption in the target and horns. Only the two-body decays of π^+ and $K^+ \rightarrow \mu^+\nu_\mu$ are used to calculate the neutrino flux at the near and far detectors. The charged current ν_μ cross section for $\nu_\mu N$ is used to determine the ν_μ event rate at the detectors. NUADA is used for both WBB and NBB flux calculations.

The E–803 Monte Carlo[21] (PBEAM) follows each particle produced in the target and traces it through the horn focusing elements. The secondary particle production is a parameterization of data from A.E. Brenner, *et al.*[22] and D. S. Barton, *et al.*[23] and the absorption cross sections are from S.P. Denisov, *et al.*[24]. The particles $\pi^\pm$, $K^\pm$ and K_L^0 are produced in the target and if they successfully exit the target are then allowed to decay with distances consistent with each particle's lifetime and momentum. The μ from the π and K two-body decays are also allowed to decay. Absorption by the horn and multiple scattering in the horns is modelled. This Monte Carlo allows realistic determination of the backgrounds to the ν_μ flux but requires huge amounts of computer time for studies in the far detector.

We have used these programs in the following way. Fermilab Main Injector 120 GeV protons strike either a carbon target (WBB) or a nickel target (NBB) to produce secondaries that are focused either by the WBB or by the NBB[25] optics. The WBB target is a half–density two interaction length carbon pencil 1.0 m long with a radius of 2 mm while the NBB target is a more standard one interaction length nickel plug. Multiple scattering and absorption are modelled in the target. The secondary π and K exiting the target are allowed to decay with the appropriate lifetimes. The surviving π and K pass through the focusing elements and decay within an evacuated decay pipe. The ν_μ are projected to a far detector of 4 m radius at a distance of L_F where

$$L_F = \text{decay pipe length} + 150\ m \text{ shielding} + 732\ km \tag{3.1}$$

or to a near detector of 1 m radius at a distance of L_N where

$$L_N = \text{decay pipe length} + 150\ m \text{ shielding} + 40\ m \text{ air.} \tag{3.2}$$

The programs are the primary tools for optimizing the beam designs according to the design criteria specified in Section 3.1. NUADA is used to study how different beam designs affect the flux into near and far detectors. PBEAM is used to monitor how the design changes raise or lower other neutrino species populations in the beam.

A third beam program NUANL is being developed for the MINOS collaboration[26] and will be used by the NuMI beam group. NUANL uses as input the secondary particle production of the E–803 Monte Carlo. It is then an analytical calculation of the ν flux at both the near and far detectors. The NUANL program will include all leptonic decays of the

$\pi^{\pm}$, $K^{\pm}$ and K_L^0 and the subsequent decays of the muons in those decays. It also will include decays of the secondary $\pi^{\pm}$ in the K_{e3} and $K_{\mu 3}$ decays and of the $\pi^{\pm}$ in the $K^+ \rightarrow \pi^+\pi^0$ and $\pi^+\pi^-\pi^+$ decays. This program will offer the best determination of the ν_e, $\overline{\nu}_e$ and $\overline{\nu}_\mu$ backgrounds to the ν_μ events in each detector.

A fourth program using the GEANT package is under development. This program will enable us to answer detailed questions about neutrino backgrounds from the secondary particles' interactions with materials such as the horns, shielding, beam pipe, or decay pipe.

3.3 Wide Band Beam

3.3.1 Focusing Devices

Two types of focusing devices have been designed. Horns are used to provide the nominal NuMI beam, the wide-band beam (WBB), and a lithium lens followed by dipoles and quadrupoles is used for the auxiliary narrow-band beam (NBB). In the WBB a pair of horns collects a large momentum spectrum of secondary pions and kaons. The toroidal magnetic field of the horns varies as 1/r between the inner and outer conductors; B=0 inside (outside) the inner (outer) conductor. In our case the field goes out as far as r = 15 cm with the first horn and r = 20 cm for the second horn. As a result, a large size parallel secondary beam emerges into the decay region where the secondaries subsequently decay into neutrinos.

In the NBB a lithium lens close to the target accomplishes a similar purpose. Its magnetic field varies as r in the region containing the lithium and is zero outside. In our design, the field is confined to $r \leq 1$ cm. The dipoles and quadrupoles downstream of the lithium lens serve to select the desired momenta of pions and kaons. A collimator at an intermediate focus selects p and dp/p. Some of the secondary pions and kaons are absorbed; in the WBB absorption takes place primarily in the wall thickness of the horn inner conductors, while for the NBB the absorption happens mainly in the lithium itself.

Horns have been successfully operated at Fermilab, CERN and BNL for a number of years. Experience with lithium lens comes from the $\overline{p}$ targets at Fermilab and CERN. Both the WBB and NBB have been studied and designed to maximize the event rate while maintaining overall reliability.

The depth of field is different for every horn focusing system. For the nominal double horns, the depth of field is shown in Figure 3.4. (z = 0 is the upstream end of Horn 1.) The fact that the acceptance is over 90% over a longitudinal distance of 1.4 meters means that one can take advantage of a long target. For our case the target begins at z = -1.6 meters and ends 4 cm before the beginning of Horn 1. This means there is no interference between the target and the horn, since the target does not protrude inside. For a one horn system, the optics has "one stage"–point to parallel. For a system of 2 horns, Horn 1 focuses lower momenta secondaries point to point while Horn 2 focuses all momenta point to parallel. For three horns, the low momentum particles are focused point to point twice by Horn 1 and Horn 2, then Horn 3 focuses them all point to parallel (see Figure 3.5). It is an inherent property of multi-horn systems that the radii of the horns and the distances between them increases as one moves downstream. From a practical point of view, a two horn system is adequate since a third horn ends up far downstream with a large radius (and therefore with

Horn 1	Horn 2
Inner Conductor:	Inner Conductor:
r1=6.2 cm, r2=1.0 cm, r3=6.2 cm	r1=15.6 cm, r2=2.6 cm
z1=0.0 m, z2=2.0 m, z3=4.0 m	z1=19.0 m, z2=22.0 m
Outer Conductor:	Outer Conductor:
r1=15 cm, r2=15 cm	r1=20 cm, r2=20 cm
z1=0.0 m, z2=4.0 m	z1=19.0 m, z2=22.0 m
Wall Thickness: 2mm	Wall Thickness: 2mm
Length=4.0 meter	Length=3.0 meter
I = 170 kAmp	I = 170 kAmp
PS Design, I= 200 kAmp	PS Design, I=200 kAmp

Table 3.1: Dimensions of the two horns and design values of the power supplies.

a small field). It does not increases the event rate because its absorption is about equal to the amount it gains by collection. This same argument does not hold in going from one to two horns since the event rate for a single horn is about 2/3 that of the two horn system. Therefore, we concentrate on the double horn design for the focusing system. This system has been extensively studied and, to date, meets all the design criteria.

3.3.2 Double Horn Design

The horn design consists of two cylindrically symmetric current sheets having the properties given in Table 3.1. The two horn beam line is shown in Figure 3.6 with the shaded area representing the magnetic field of the horns. This is a graphic illustration that the horn magnetic field only exists between the inner and outer conductors. The dimensions of the horns and the distance between them are also shown.

The inside diameters of the inner conductors at the neck of the horns are made relatively large for two reasons. First, to allow for small excursions in the position of the primary proton beam, and second to reduce the severe stresses at small radii where the forces are maximum. The trade-off between the material required to withstand the forces and the desire to minimize multiple scattering and interactions determines the wall thickness. The magnetic field between the conductors is described by

$$B(kG) = \frac{I(kAmp)}{5 \cdot r(cm)}. \tag{3.3}$$

The trajectory of a charged particle in such a field cannot be expressed by an analytical function, but can be easily determined by numerical methods. The bending angle is given by,

$$\frac{\int Bdl}{p} = \frac{10^{10}}{c}\theta = \frac{\theta}{3}; \quad \int Bdl = \frac{p_T}{3}. \tag{3.4}$$

where B is in kGauss, l in meters, and p_T in GeV/c.

The region between Horn 1 and Horn 2 and between Horn 2 and the beginning of the 2 meter diameter decay pipe will contain a pipe filled with helium. Both horns will be in air. After leaving the target, the secondaries that make it to the beginning of the decay pipe will have traveled through about 10 meters of air and 40 meters of helium. The vacuum for the primary proton beam as well as the decay pipe is being designed for 1×10^{-4} Torr which is the vacuum of most primary and secondary beams at Fermilab and requires nothing but standard pumps to maintain.

Inner and Outer Conductors

If the inner conductor is shaped like a cone, the integral of B dl will be constant, to first order, since B is varying as 1/r and the shape like r. From the equations above, a constant integral of B dl results in a constant p_T, and since secondary particle production has an average of $p_T = 0.3$ GeV/c, one would like a design that collects as much p_T as possible. Horn 1 is constructed of two cones, each with a length of 2 meters and r = 6.2 cm. Horn 2 is one cone with a length of 3 meters and r = 15.6 cm. Together the double horn system focuses $p_T \approx 0.9$ GeV/c. The efficiency of the system compared to "perfect focus", where all of the hadrons are on the beam axis with no angular divergence, is shown in Figure 3.7.

With the horns pulsing every 1.9 seconds they will accumulate about 15 million cycles in a year. At this level, the strength of materials decreases significantly as the metal fatigues. For this reason the inner conductors will be made of aluminum Type 7075. A small percentage of other elements (Cu 1.5%, Mg 2.5%, and Zn 5.5%) added to the aluminum greatly improves the mechanical structural strength. Aluminum(7075) is about 1.6 times as strong as aircraft aluminum(6061). The inner conductors will be machined from a solid block of the material, and because this will require many hundreds of hours, it is essential that the original block be ultrasonically tested to assure there are no internal flaws before machining starts. It is also necessary that the inner conductor be centered on the outer conductor to maintain symmetry. This requires that the inner wall of the outer conductor be machined, but the outermost wall can be left "as manufactured". An adjustment system is also included to move the inner conductor with respect to the outer. The outer conductor is equipped with a system of external pipes by which water is sprayed onto the inner conductor for cooling.

Secondary particle absorption losses in the horn material are considerable because the angle of the horn inner conductor is small relative to the particle trajectories it focuses. Making the wall thickness of the inner conductor as thin as possible is essential for keeping the event rate high. The distributions of axial, circumferential and radial stresses produced by a current pulse of 200 kAmp have been calculated with the finite element program ANSYS[27]. The results show that for our design, the largest stress at the neck of Horn 1 is 8700 psi. Aluminum(7075) is listed as having 23000 psi of strength after 1×10^8 cycles. We expect on the order of 1.5×10^7 cycles per year.

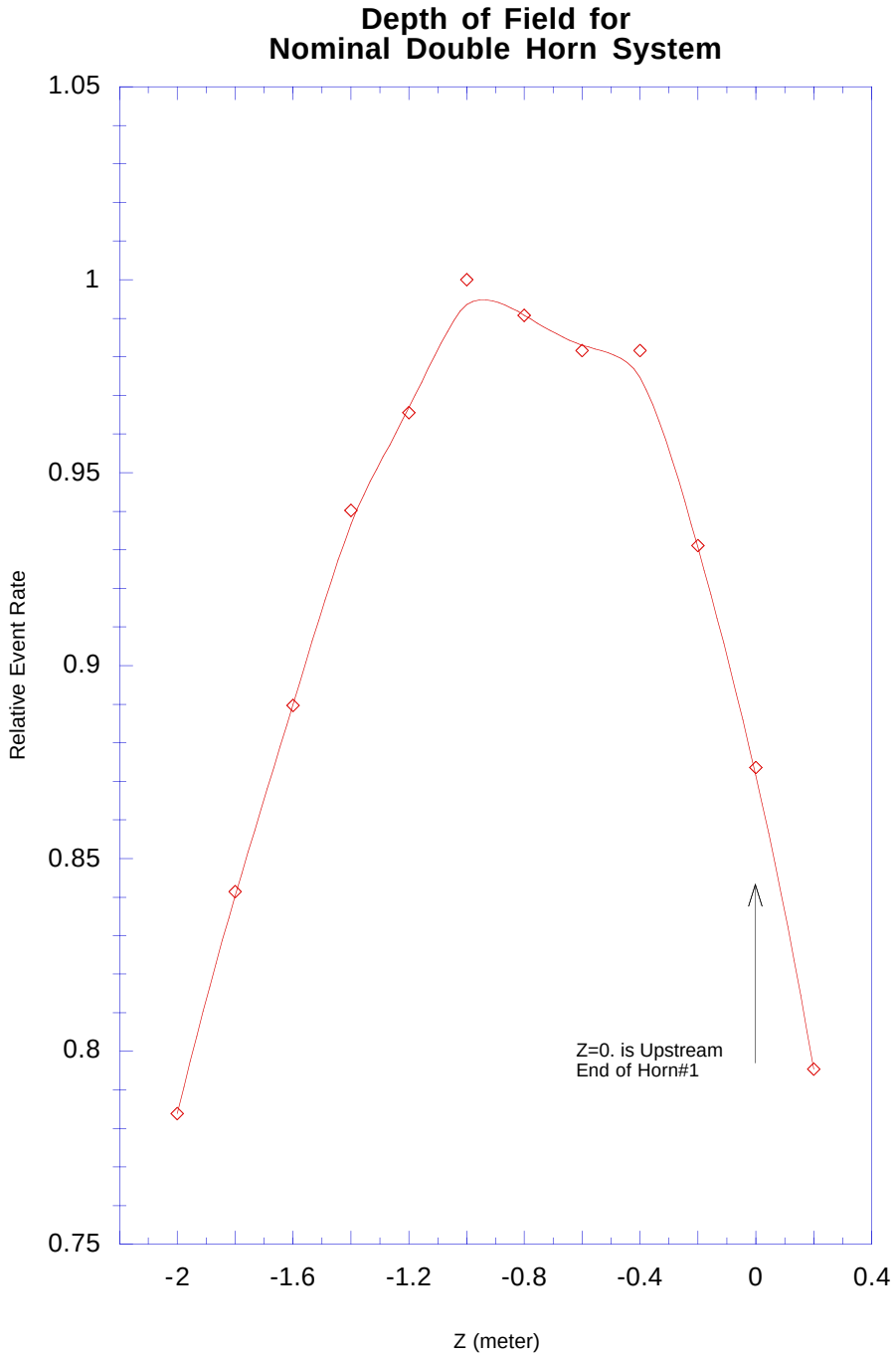

Figure 3.4: Depth of focus for the nominal double horn system.

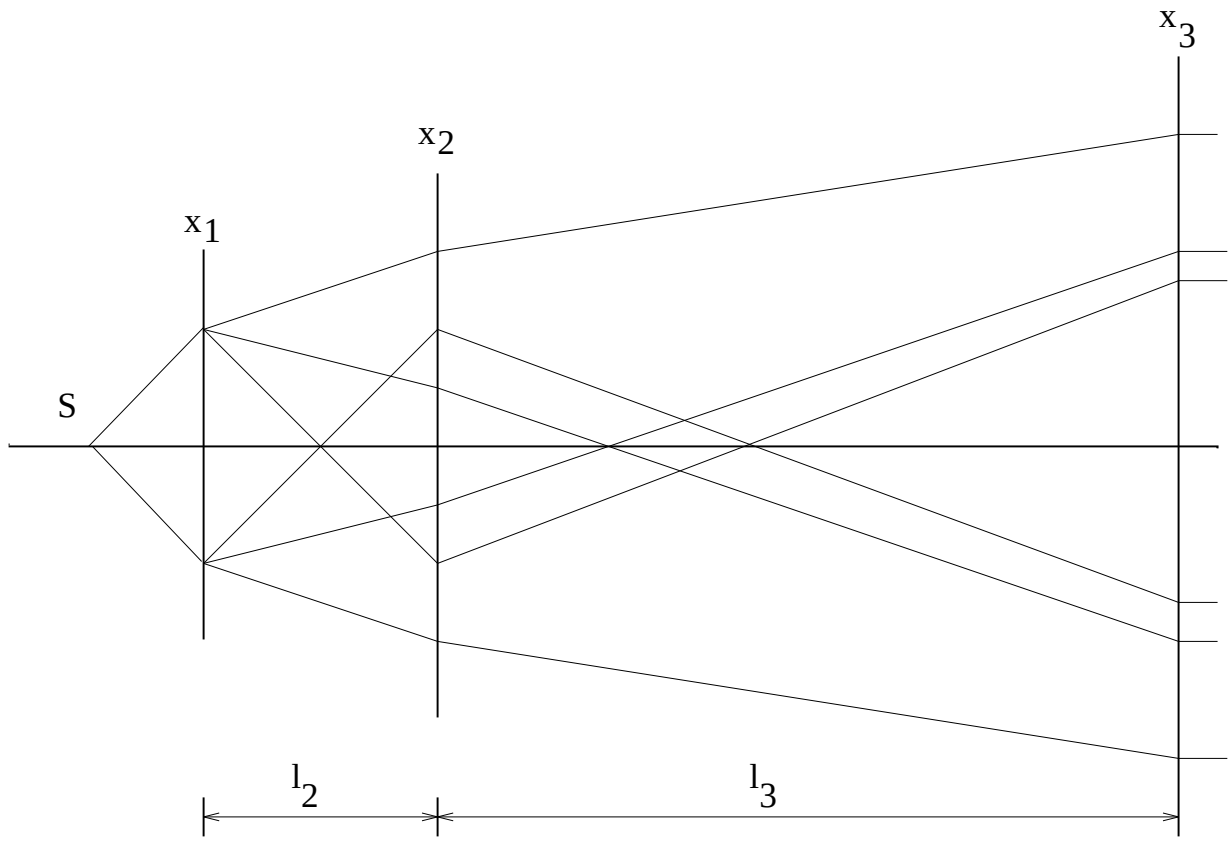

Figure 3.5: The optics of the triple horn system.

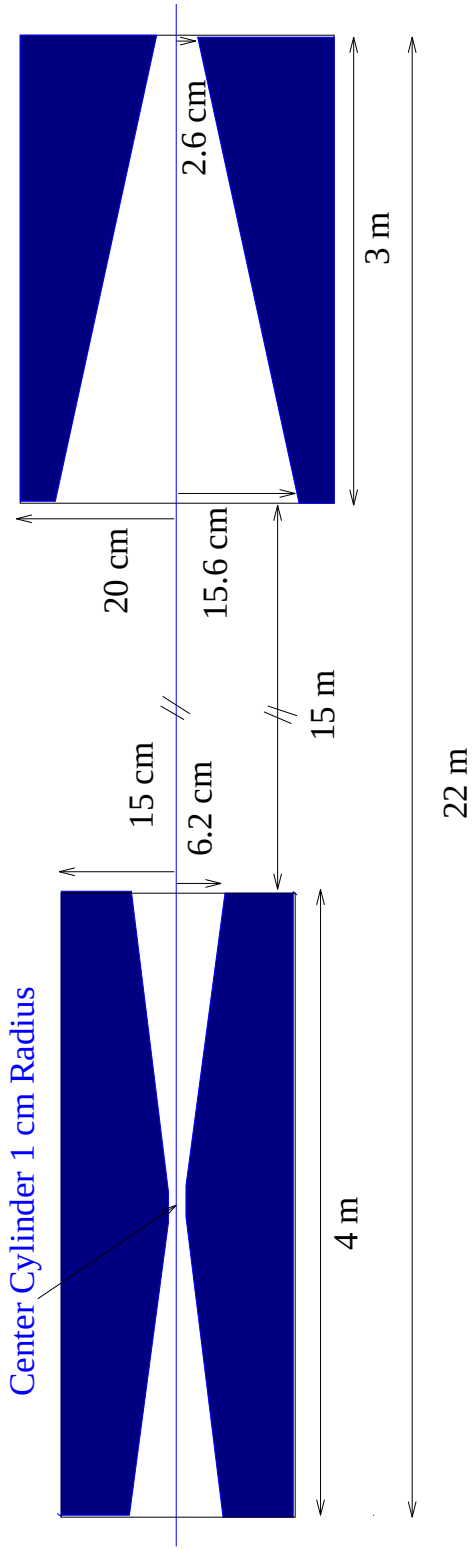

Figure 3.6: Schematic diagram of the wide–band beam illustrating the regions of magnetic field and the dimensions of the beam line.

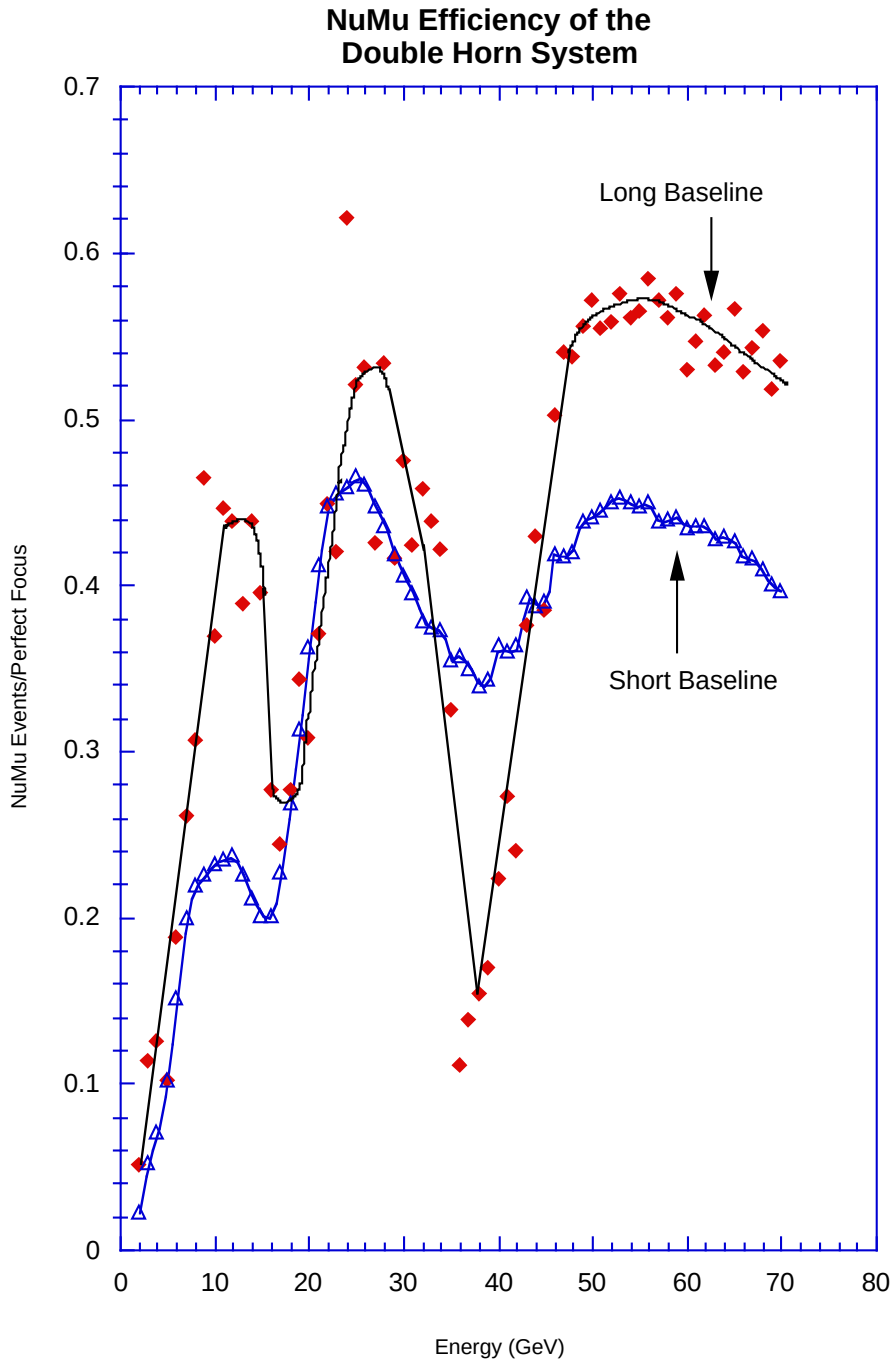

Figure 3.7: Comparison of the double horn beam focus to "perfect" focus. The lines are solely to guide the eye.

3.3.3 Horn Design Parameter Variations

Several parameters of the double horn design have been investigated. Among these have been (1) inner conductor shapes, (2) outer conductor radii, (3) horn lengths, (4) distance between horns, (5) depth of field for the double horns, and (6) comparison with a different number of horns.

There have been three studies of the horn shapes. (a) Variation of the neck position in Horn 1, keeping the same angles for the cones. As the neck moves downstream, the average neutrino energy goes up, but the charge current (CC) ν_τ event rate goes down. (b) Changing from a first order cone shape to a second order parabolic shape did not give an improvement in the event rate. (c) Adding extra lengths of various shapes upstream and downstream of the original two horns only changed the event rate and the energy spectrum slightly. With respect to the radius of the outer conductor, the event rate reaches a maximum for Horn 1 at r = 15 cm, and for Horn 2 at r = 25 cm.

The length of Horn 1 was varied while the distance between horns and the shape of Horn 2 was maximized. The results for various lengths of Horn 1 are shown in Table 3.3.3, as well as Figure 3.8. The number of events remains relatively constant, but the average energy increases as the length increases; i.e.. the low energies are being over-focused as the length increases, while the high energies that were under-focused are being made parallel. The distance between horns is not an overly sensitive parameter. Both the event rate and the average energy change less than 5% over a distance change of $\pm$ 2 meters.

Length	Relative Event Rate	Average Energy
2.0 m	0.91	22.7 GeV
2.4 m	1.01	23.1 GeV
2.8 m	1.02	23.6 GeV
3.2 m	1.02	24.1 GeV
3.6 m	1.04	24.6 GeV
4.0 (nominal)	1.00	25.1 GeV
4.4 m	0.96	25.6 GeV
4.8 m	0.91	26.1 GeV

Table 3.2: Variation of ν_τ event rates and average energy for changes in Horn 1 length.

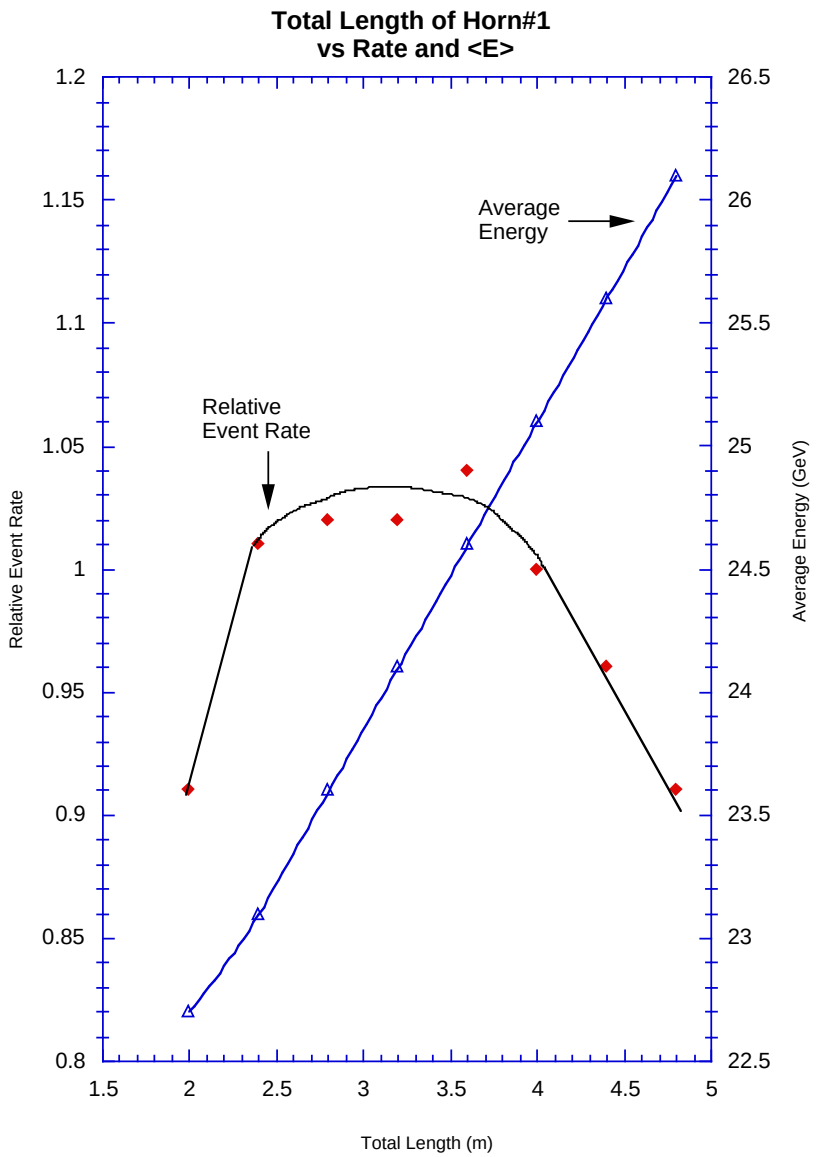

Figure 3.8: Comparison of the relative ν_τ event rate and average event energy as the length of the horn is varied.

3.3.4 Horn Electrical Design

Two electrical circuits, each with its own set of advantages, are being pursued to deliver 200,000 amperes to the horns. The first is a conventional "transformer solution" in which a transformer, a power supply, and a modest capacitor bank need to be purchased. The schematic is shown in Figure 3.9a and details discussed in the 1991 Conceptual Design Report[11]. One power supply will operate both horns with a stripline connecting them to each other and to the power supply. Because the target is very close to the upstream end of the horn, the stripline will physically connect from the power supply to the outer conductor of Horn 1 at its downstream end. A conducting upstream flange on Horn 1 will take current from the outer to the inner conductor. From the inner conductor of Horn 1, it will flow to the outer conductor of Horn 2 via a stripline, then to the inner conductor of Horn 2 back to the power supply through the stripline. The current will be put onto the conductors from the stripline at four points so symmetry can be maintained. The stripline will be air cooled.

The second circuit does not use a transformer and the power supply is the standard supply used by Fermilab to power magnets. In addition to a much larger capacitance than the first option, it also uses a number of SCRs and a high current solid state polarity reversing switch which recovers most of the discharge back into the capacitor bank. Only a small power supply is then needed to bring the voltage up its full value for the next beam pulse. The schematic for this option is shown in Figure 3.9b and the details are described in TM-1924[28]. Further computer simulation work is continuing on these two circuits to check their performance and to determine sets of voltages, currents, and capacitance to be able to effectively compare the cost of the two designs. Because the first option uses a transformer and power supply unique to this project, it is prudent to have a spare unit for each.

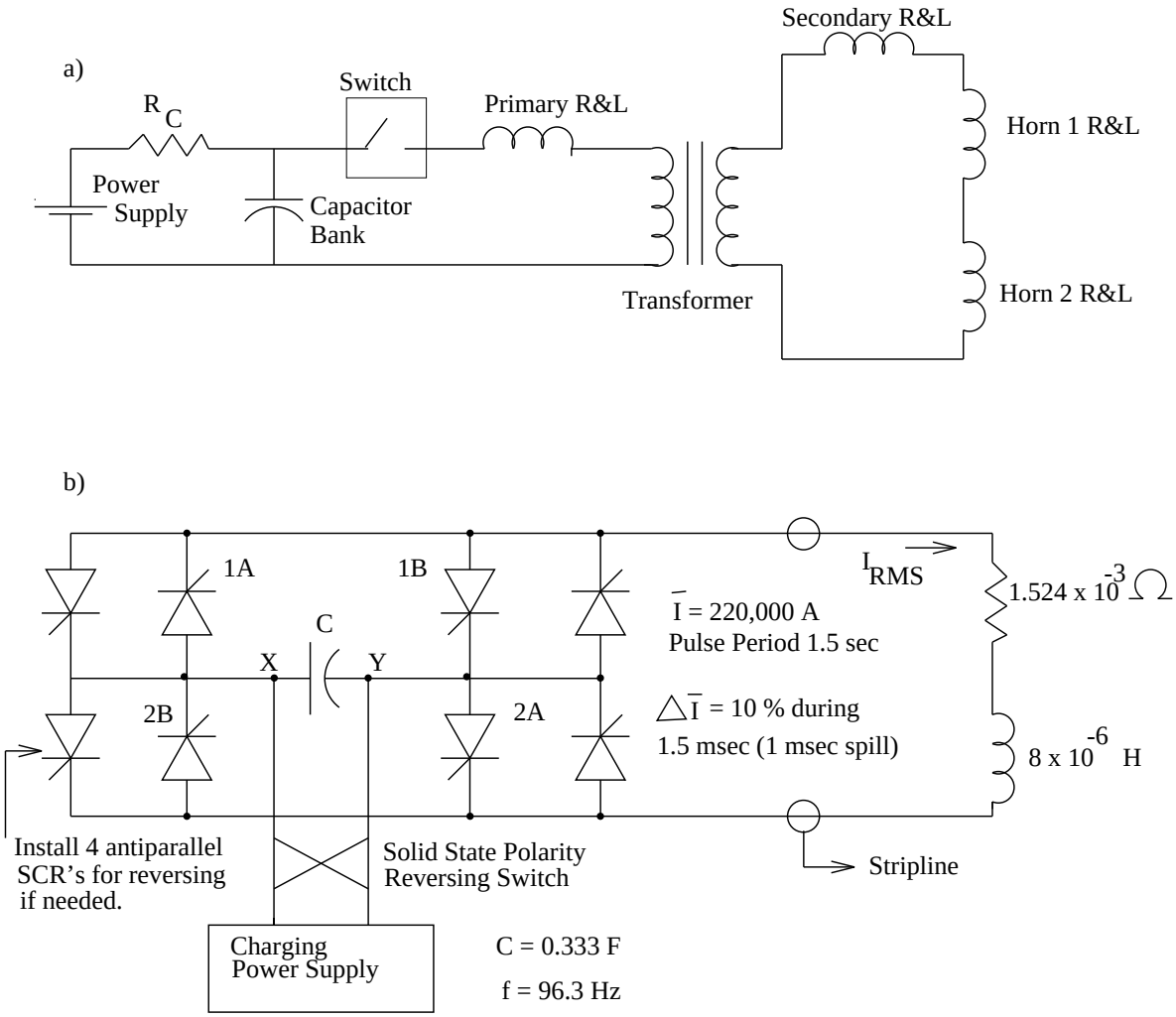

Figure 3.9: The horn electrical circuits for a) the transformer option and b) the no transformer option.

3.3.5 Horn Support Design

The need for accurate alignment of the horns and the high radiation environment within the target hall place constraints on the mechanical design of the horn support elements. The horns must be secured in the target hall and be aligned to an accuracy of about 0.1 mr i.e. 0.4 mm over the length of the horn. This accuracy must be maintainable even as the target hall cavern deforms as underground caverns do. A method of installing the horn that allows remote alignment is necessary because of the high radiation environment of the target hall. The outer conductor of the horn is a rigid aluminum cylinder and is used to secure the horn to a mounting base as shown in the inset in Figure 3.10. An insulator, such as the material Arclex, is placed around the outer radius of the outer conductor and an aluminum bracket is installed around the insulator. The bracket is designed to hold the horn assembly to a mounting base. The mounting base has alignment pins for placing the horn on its upper side and alignment pins on its lower side for placing the horn-base assembly on an alignment table in the target hall. The complete horn assembly is shown in Figure 3.10 including the horn, mounting base, alignment table, special horn lifting fixture, the current transmission line and the all metal hydraulic clamps for holding the horn assembly onto the alignment table.

The alignment table is designed to be remotely adjusted. At its initial installation the table will be aligned onto the beam axis and its position tracking system set to zero. The tracking system will be designed to have an automatic return to the starting position to recover from mishaps when remotely adjusting the table. The conceptual design of the table adjustment system is shown in Figure 3.11. There will be four positioning drives for vertical adjustment of the table and two for horizontal adjustment. These will be connected using standard linkages passing through channels in the steel block that has the table mounted to it. The linkages exit the shielding where they are connected to drive motors remotely controlled. The motors are well shielded by the beam line shielding so they should not have excessive radiation exposure and damage. In any event, placing them outside the shielding makes them accessible for replacement or repair. A similar concept is used at CERN in the CHORUS and NOMAD neutrino beam for positioning the target and has worked well.

The horn assembly excluding the alignment table has a mass of approximately 400 kg. Gravity is insufficient to ensure that the horn does not move around as the current pulses through it. Therefore an active hydraulic system is envisioned for holding the horn to the alignment table. Careful design of an all metal hydraulic system will aid in installing or replacing the horns. A system that is all metallic should not experience disastrous radiation damage. The system will need to have a push–pull design so that it is actively closed and actively opened. There will be redundancy built into the system so that it does not lock a damaged horn to the alignment table nor does it let a horn move about on the table. The hydraulic fluid will be in a closed system of metallic lines and fixtures. Leaks are less likely to occur and the fluid will remain in the system for the lifetime of the facility.

All of the connections for power, water and instrumentation will be made on top of the shielding. There will be quick disconnects for the water and instrumentation leads and cable connections between parts of the strip line. For example, the strip line for the horn will rise vertically from the contact points on the horn to the height of the shielding (2 m) and be connected to the power supply through flexible connections to the rest of the strip

line. The path for the strip line, cooling water piping and instrumentation leads is shown in Figure 3.11. The horn cooling water will be brought through the shielding in metal piping to the distribution system in the horn. The water system will be a closed loop system that has rows of nozzles in the outer conductor spraying water into the inner conductor continuously (the water system will not be pulsed on and off during the spill). The horn is mounted at an angle of 58 mr so that the water will be collected at the bottom of the outer conductor of the horn. From there it will be filtered and recirculated.

The design of the connections brought out at the top of the shielding is inspired by the successful design and operation of the Fermilab anti-proton source beam line. Personnel will be able to disconnect each element from the rest of the world with minimal radiation exposure. The activated elements may be placed in a protected container using the target hall's overhead crane and then moved to a remote location.

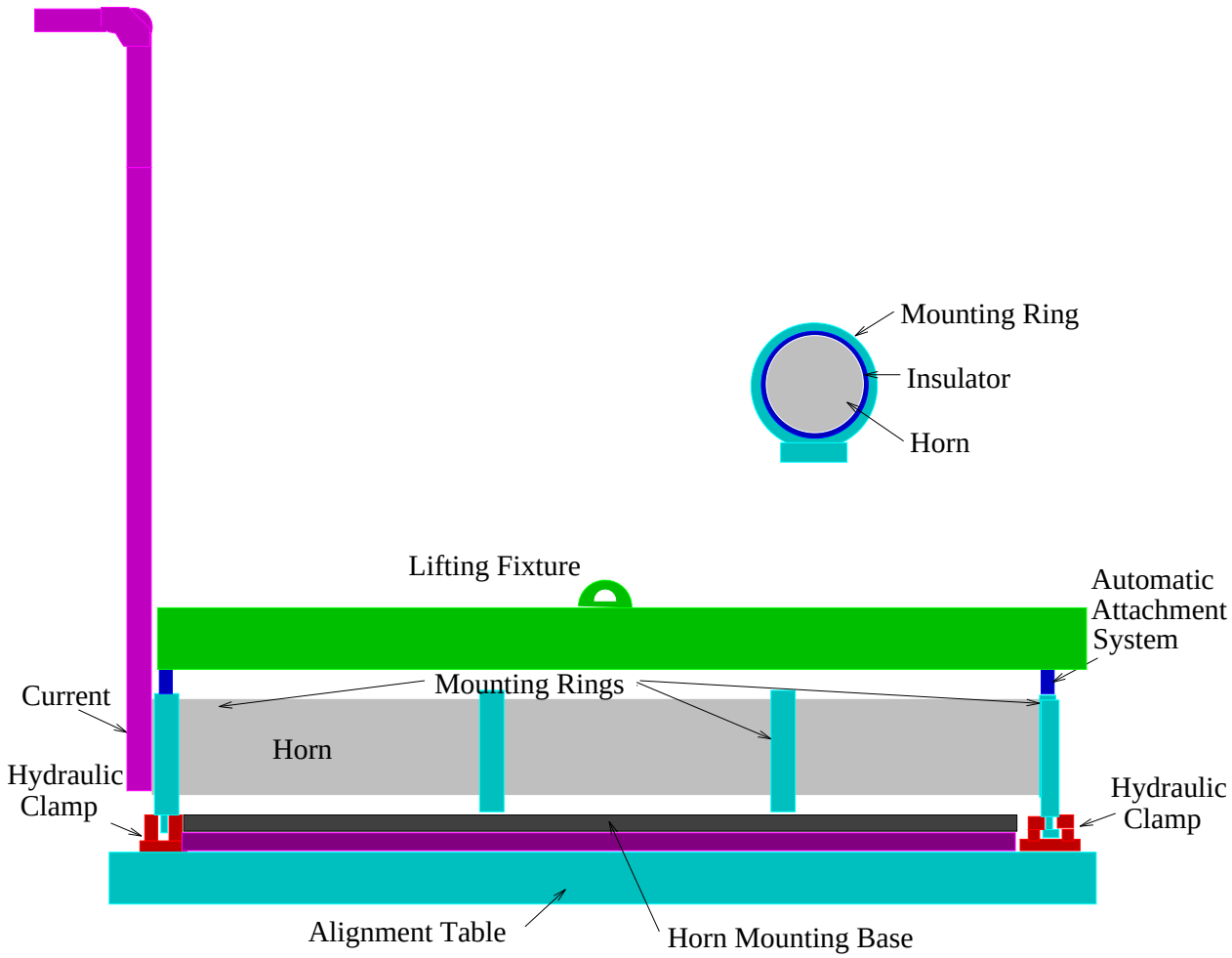

Figure 3.10: A representation of the complete horn assembly viewed from the side of the horn.

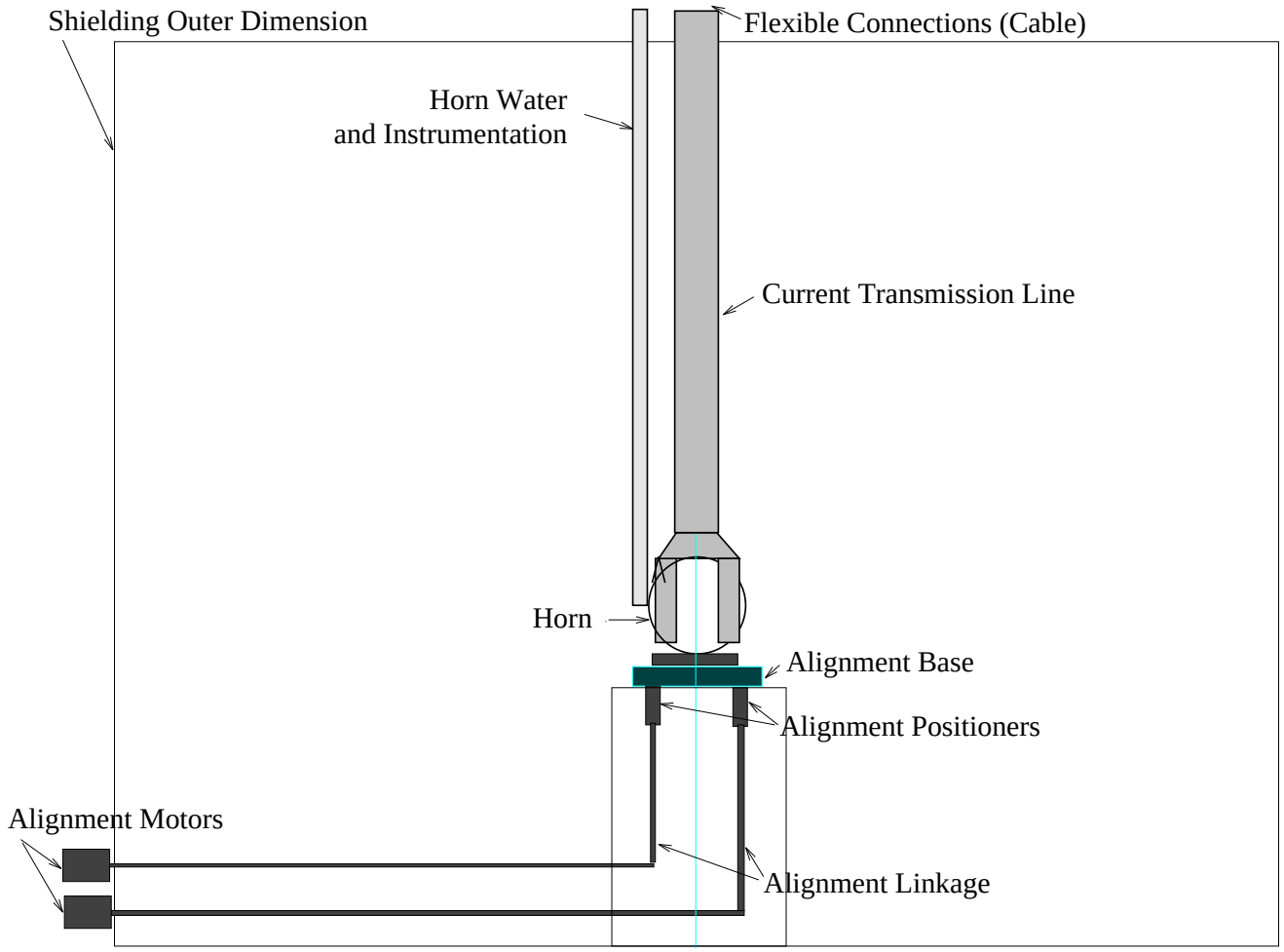

Figure 3.11: A conceptual design for the alignment table position adjusting system viewed from the downstream end of the first horn.

Δm^2	CC ν_μ	CC ν_τ	QE ν_τ
0	2585	0	0
1×10^{-1}	1243	419	48
8×10^{-2}	1517	322	39
6×10^{-2}	1319	393	45
4×10^{-2}	983	536	53
2×10^{-2}	930	475	63
1×10^{-2}	1625	221	41
5×10^{-3}	2241	67	14

Table 3.3: Expected number of muon and tau neutrino events in a kiloTon-year at Soudan for $\sin^2 2\theta = 1.0$ and various values of Δm^2.

3.3.6 Neutrino Event Rates

A kiloton-year (kT-yr) is defined to be 3.7×10^{20} protons on target with the resulting neutrino flux interacting in a 1 kiloton detector. The muon neutrino event rate spectrum for the nominal double horn beam is shown in Figure 3.12 and Figure 3.13 for the short and long baseline detectors in the absence of $\nu_\mu \rightarrow \nu_\tau$ oscillations. Figure 3.14 illustrates the oscillation probability as a function of energy for six different Δm^2's with $\sin^2 2\theta = 1.0$. The expected CC ν_μ and CC and quasi-elastic (QE) ν_τ event rates at Soudan for a kT-yr are listed in Table 3.3 for the Δm^2 values in Figure 3.14 with $\sin^2 2\theta = 1.0$ and for the no oscillation case, $\Delta m^2 = 0$. Figure 3.15a has the ν_μ flux at Soudan and the expected ν_τ flux for three values of Δm^2. The oscillation maxima and minima evident in Figure 3.14 are also visible in the flux distribution. Figure 3.15b shows the CC ν_τ event rate at Soudan for three values of Δm^2 and the ν_μ flux from the double horn design described in this chapter. The ν_τ spectra vary significantly over the range of Δm^2 covered by Figure 3.15. Detector resolution has not been included for the ν_τ event energy spectra.

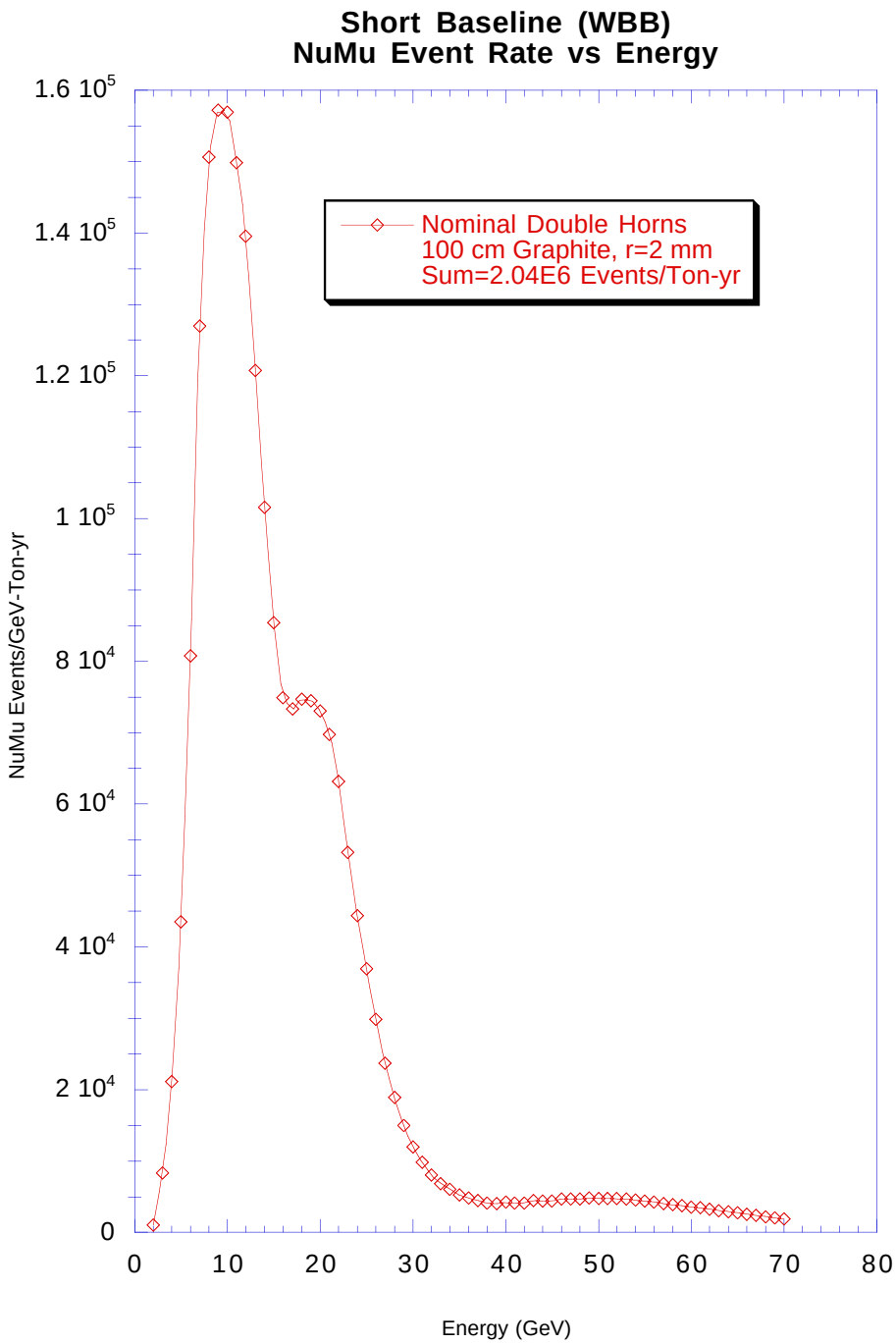

Figure 3.12: The CC ν_μ event rate at the near detector.

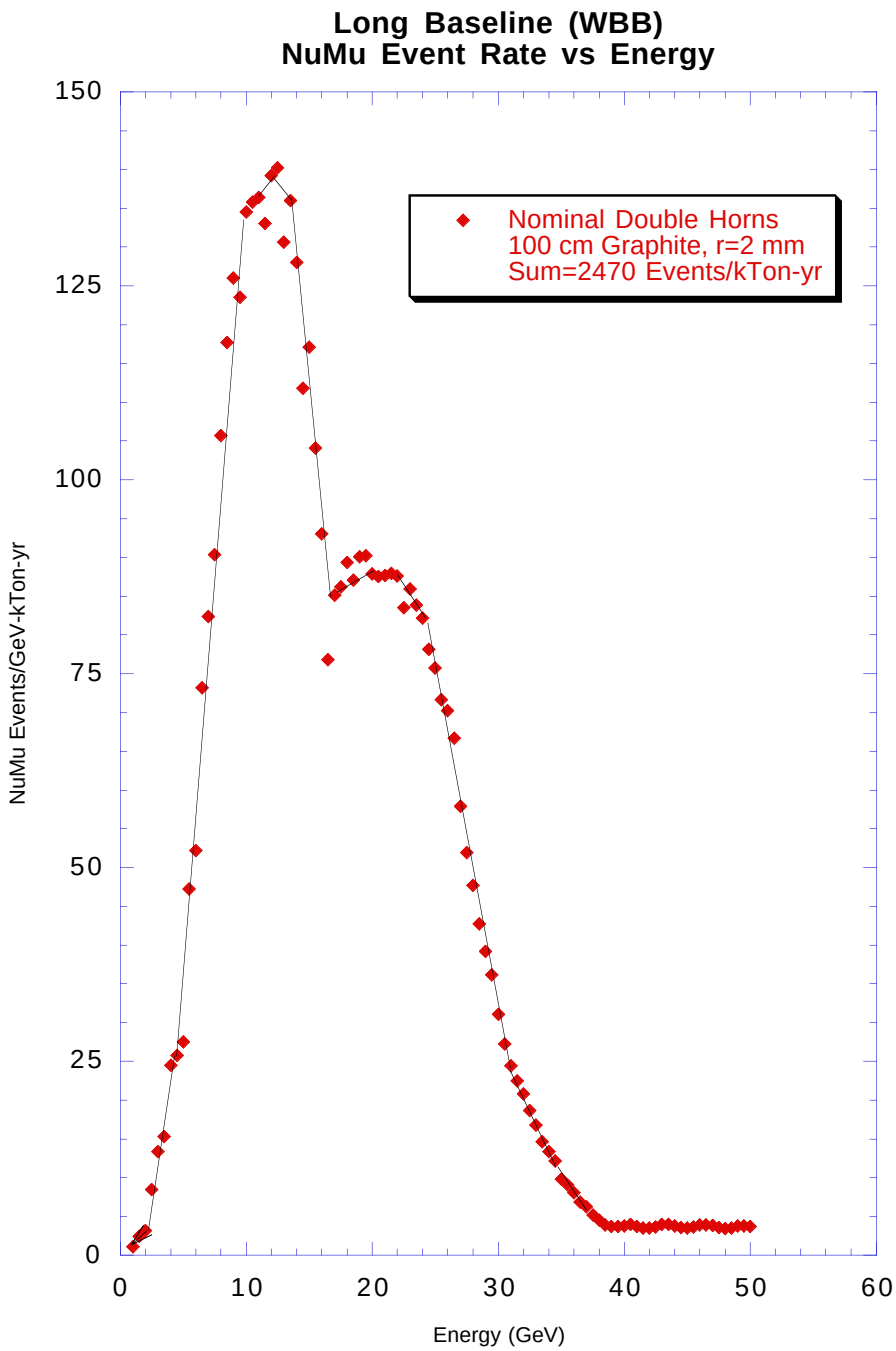

Figure 3.13: The CC ν_μ event rate at the far detector.

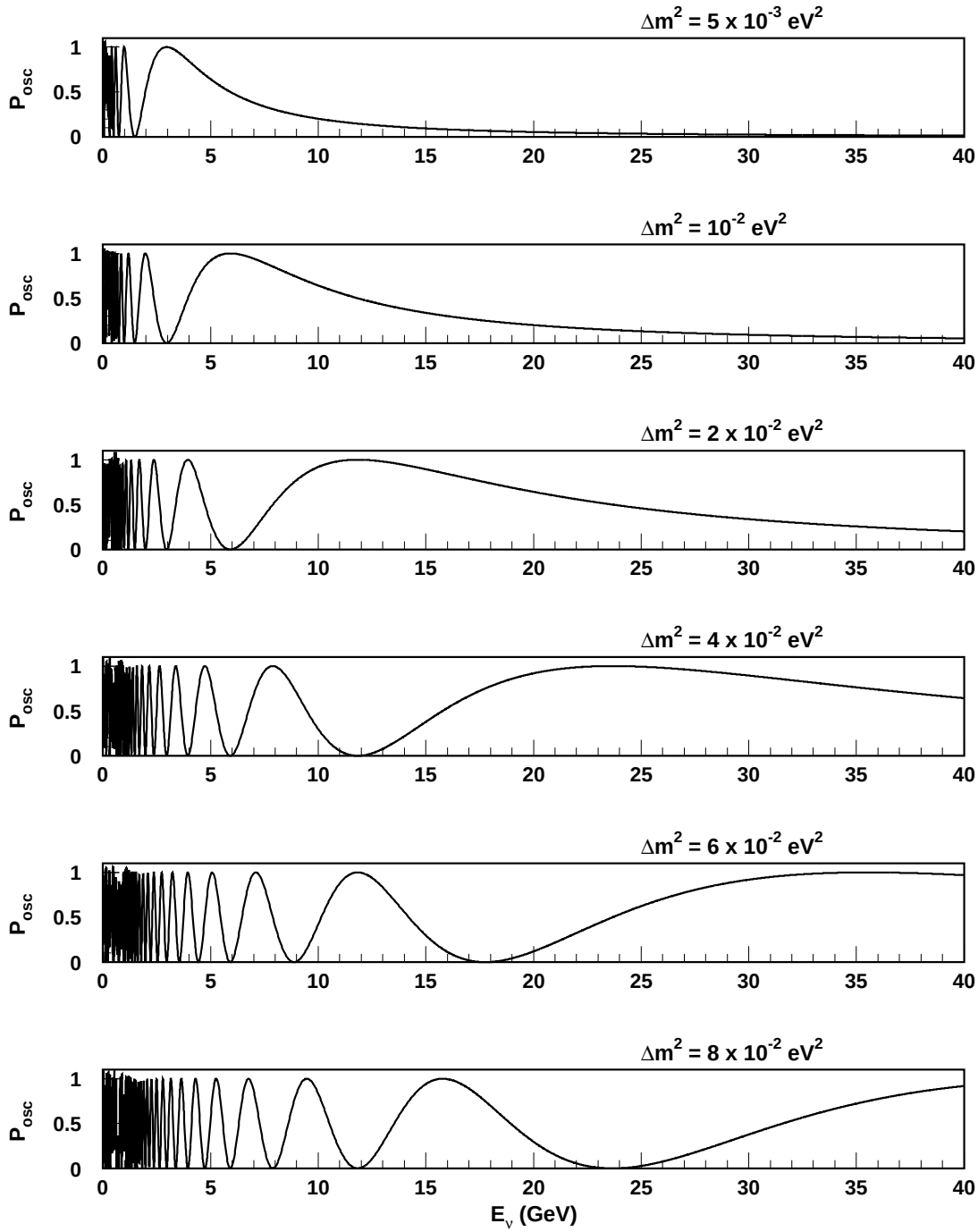

Figure 3.14: The $\nu_\mu \rightarrow \nu_\tau$ oscillation probability curves at the far detector for various Δm^2 with $\sin^2 2\theta = 1.0$.

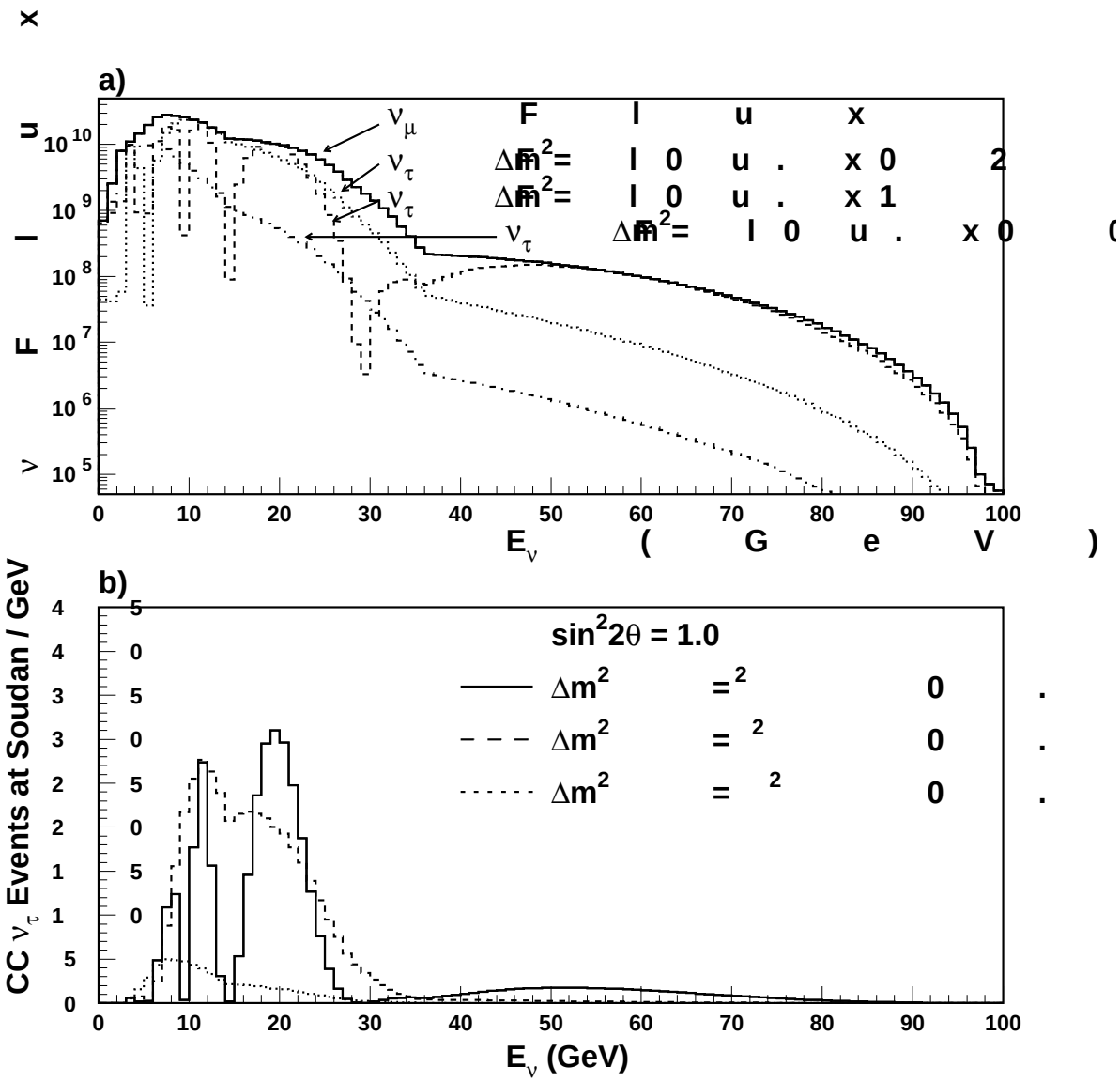

Figure 3.15: a) The ν_τ flux at Soudan for $\sin^2 2\theta = 1.0$ and $\Delta m^2 = 0.005,\ 0.02$ and 0.1 with the ν_μ flux shown for comparison. b) The CC ν_τ event rate at the far detector for $\sin^2 2\theta = 1.0$ and $\Delta m^2 = 0.005,\ 0.02$ and $0.1\ eV^2$.

3.3.7 Neutrino Backgrounds

Figure 3.16 shows the expected WBB ν backgrounds for the full near detector from PBEAM. The most important background for the MINOS experiment is from the $\nu_e + \overline{\nu}_e$ component, which we calculate to be $0.682 \pm 0.0124\%$(statistical error only) of the ν_μ event rate at the far detector. The ν_e and $\overline{\nu}_e$ have a 37% contribution from μ decay, a 30% contribution from $K_L^0 \rightarrow \pi^\pm e^\mp \nu_e$ decays, a 30% contribution from $K^\pm \rightarrow \pi^0 e^\pm \nu_e$ decays and a 0.8% contribution from $\pi^+ \rightarrow e^+ \nu_e$.

The most important background for the COSMOS experiment is the $\overline{\nu}_\mu$ component of the beam. The fraction of $\overline{\nu}_\mu$ CC events to ν_μ CC events is calculated to be $0.710 \pm 0.0129\%$(statistical error only).

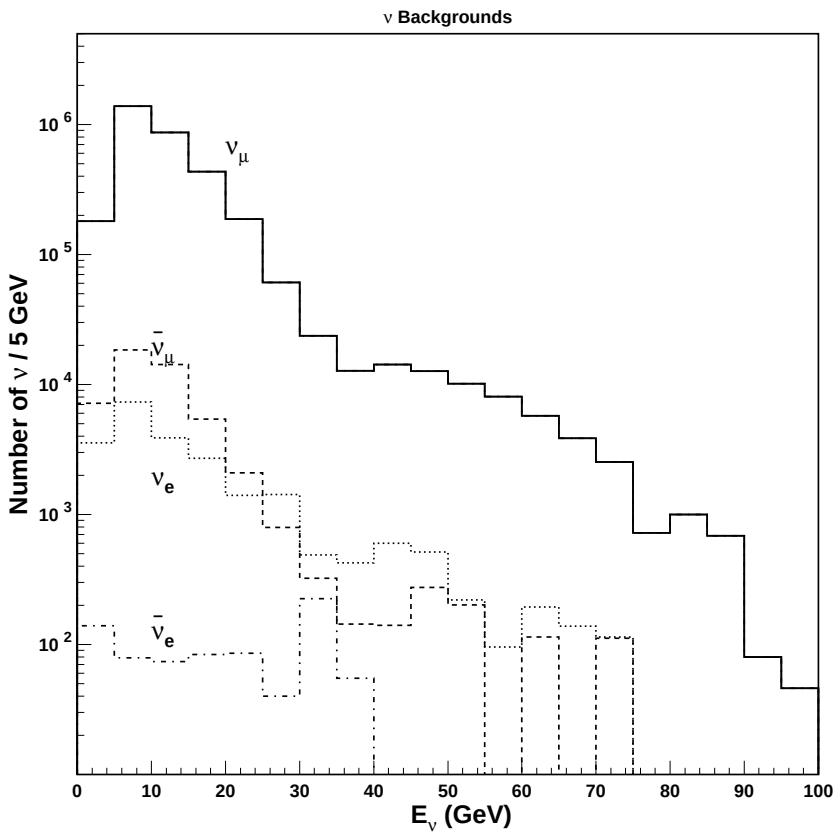

Figure 3.16: The ν_μ, ν_e, $\overline{\nu}_\mu$, and $\overline{\nu}_e$ flux for the 800 m nominal decay pipe. The absolute value of the vertical scale is arbitrary. Only the relative values for each ν type are important.

3.4 Narrow Band Beam

The NuMI target hall has been designed to accommodate both the WBB and the NBB. The layouts of each beam are schematically illustrated in Figure 3.17. The components are placed to scale along the beam direction but not in the orthogonal direction.

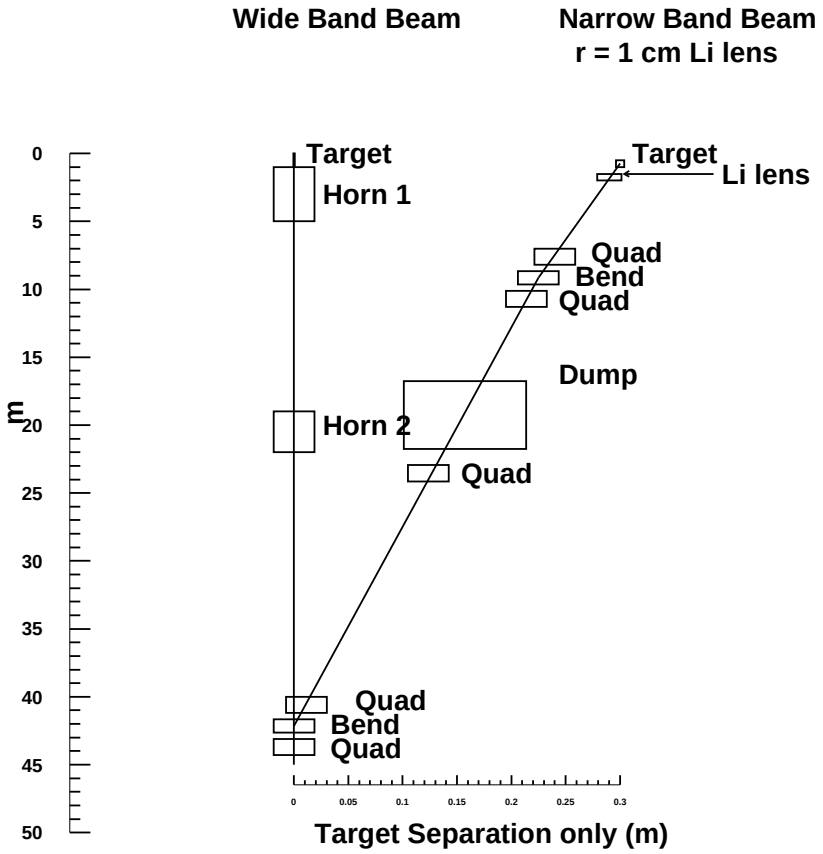

Figure 3.17: Schematic diagram of the wide–band and narrow–band beams. The figure is not to scale in the direction perpendicular to the beamline.

3.4.1 Physical Layout

The NBB beam follows a different trajectory than the horn beam. To make the final beam position and direction the same after it passes through either the horn or a bending dichromatic, compensating bends are needed in the primary proton beam. In our case this is done with an upstream bend point (at the MI-60 stub) that gives the position and a downstream bend point (in the Pre-Target Enclosure just upstream of the target) that gives the angle. Since the beamline naturally bends vertically to get onto the -58 milliradians line to Soudan, changing from the WBB trajectory to the NBB trajectory is accomplished by decreasing the vertical bend at MI-60 from -104 mr to -102 mr. This results in a relative displacement of less than 1 foot as the beam enters the Pre-Target Enclosure, but both the NBB and the WBB enter the decay pipe with the same angle and at the same position (see Figure 3.18).

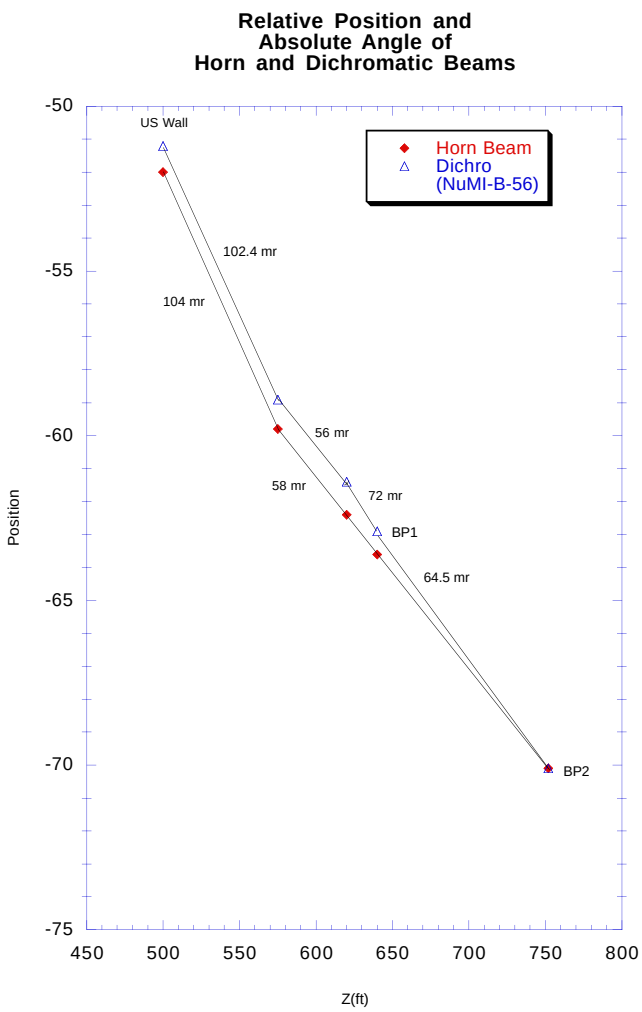

Figure 3.18: The angular paths of the wide and narrow band beams.

3.4.2 Lithium Lens Design and Operation

A conventional lithium lens is a cylinder of solid lithium carrying current. A charged particle passing through the lens with some angle with respect to the lens axis will feel a radial Lorentz force. A lens with radius r, length l carrying a current I, will produce an azimuthal magnetic induction $B(r) = \mu_0 I r / 2\pi r_0^2$. An ideal lens is in focus when the distance from a point source of particles to the upstream face of the lens is z = 1/(k tan(kl)) where k=$(0.3G/p)^{1/2}$, G = lens gradient and p = particle momentum.

The style of lithium lens used for antiproton collection at Fermilab has a diameter of 2 cm and a length of 15 cm. A 640 kAmp 350 μs damped half sine wave current pulse passing through the lithium in this lens produces a peak magnetic field gradient of 1000 T/m. The lens completes the secondary of an 8:1 step up current transformer making it feasible to use a power supply which generates less than 100 kAmp of current. This is the mode of operation intended to be used in the Fermilab Narrow Band Neutrino beamline during Main Injector running.

A cross section of the lens in the plane of the beam is shown in Figure 3.19. The lithium is encased in a water cooled Ti-6Al-4V can. The lens, can and water cooling conduits all reside in a steel cylinder. The steel is divided into two halves separated spatially and electrically by ceramic ring standoffs. The current input is attached to one half and the output to the other. The two halves are bolted together(with electrical isolation). The Be endcaps are designed to be just thick enough to sustain the axial forces generated by the thermal strains and magnetic forces.

The design of the Fermilab lithium lens is constrained by a number of electrical and mechanical considerations. First, to make sure that the lithium receives adequate cooling, the inner Ti cooling jacket has been made as thin as is structurally sound (1 mm). Second, a Ti-6Al-4V material was chosen because of its poor electrical conduction relative to lithium as well as its lack of chemical interaction. Third, the beryllium endcaps have been made thin so that they will be as transparent to the beam as possible[29].

During the filling process, lithium is pumped under pressure into an evacuated titanium can. The lithium is heated to 200° C, introduced into the lens at 500 psi (for Li, T_{melt} = 180° C) and then allowed to cool to 160° C before the fill continues. As the lithium cools to room temperature, more and more pressure is applied. The final fill pressure is 2300 psi when the stopcock is closed.

Fermilab lithium lenses of more recent design have survived up to 7 million pulses at a lens gradient of 750 T/m. Even lenses run at 800 T/m experience a failure of the titanium jacket encasing the lithium, which typically occurs after 1-2 million pulses. A recent breakthrough, described below, in lens design will permit this style of lens to be run at 1000 T/m with the same reliability that one gets now at 750 T/m.

According to the data on alternating stress versus number of cycles to fatigue stress failure for Ti-6Al-4V, a small stress decrease on the titanium cooling jacket will result in a great increase in the life of the lens to be used in the proposed narrow band beamline. A recent ANSYS analysis reveals that it is possible to lower the lithium preload by 15% or more without sacrificing lens focusing power. The preload serves only to insure that the lithium cylinder maintains its shape at mid-pulse when significant magnetic pinch forces are present. The original lens design preload insured that the lithium would maintain its shape

on the first pulse when the lithium is at 20° C. At steady state, the lens is at 65° C and the additional thermal stress on the titanium is close to the magnitude of the preload. Thus, at steady state almost no preload is needed. If one reduced the lithium preload from 2300 psi to 500 psi, then the lens could easily operate at 1000 T/m without deformation of the lithium cylinder. Lenses with lower preload are currently being built at Fermilab[30].

3.4.3 NBB Optics

A narrow-band beam can be designed so its elements are, (1) lithium lenses and collimators, (2) dipoles, quadrupoles, and collimators, or a combination of both. The proposed design uses a lithium lens in the first stage and dipoles, quadrupoles and collimators in the second stage. By itself, the lithium lens produces a large angular divergence as well as a large momentum acceptance. The second stage is added to select dp/p, to dump the primary protons, and to decrease the angular divergence. The schematic of the design is given in Figure 3.20. The optics consists of:

- point to parallel; target through lithium lens,
- parallel to point; first doublet to momentum slit,
- point to parallel; momentum slit through 2nd doublet.

The first bending magnet separates the secondary beam from the primary protons and also gives a dp/dx correlation at the momentum slit. Even at 60 GeV/c, the primary protons are separated from the secondaries by more than an inch outside the acceptance. The second bending magnet, along with the quadrupole near the slit recombine the momenta. The dipoles bend in the same direction giving a total of 14 mr.

A NBB focusing system of conventional dipoles and quadrupoles was initially tried but had only one stage and yielded fewer events[31]. Similarly, a system of lithium lenses and collimators was investigated[32]. It had the advantage of being very short, but the collimator apertures and the plug where the primary proton beam was dumped were small enough (a few millimeters) to cause operational concerns.

3.4.4 NBB Element Support Design

The philosophy for the design of the NBB element support is identical to that for the horn supports. All of the connections will be made at the top of the shielding. The lithium lens will be held in place by gravity and a properly designed stand since it weighs about five tons. The most likely beam elements to fail will have quick disconnects for all of their connections.

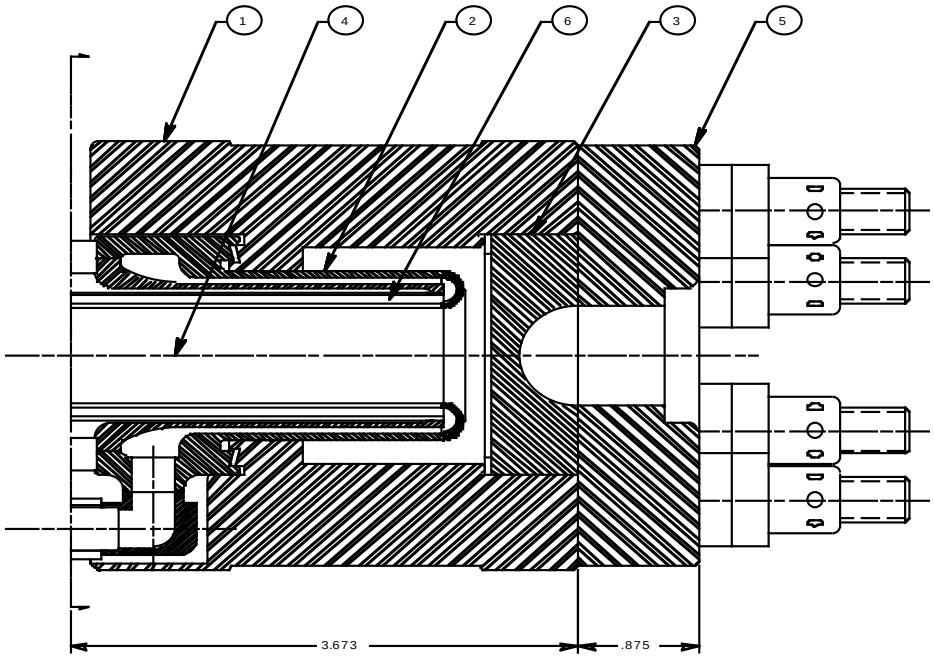

Lithium Collection Lens(half symmetry): 1-Electrical Contact; 2-Water Septum; 3-Be End Cap; 4-Li Cylinder Axis; 5-End Flange; 6-Inner Cooling Jacket.

Figure 3.19: A cutaway view of the Fermilab $\overline{p}$ source lithium lens.

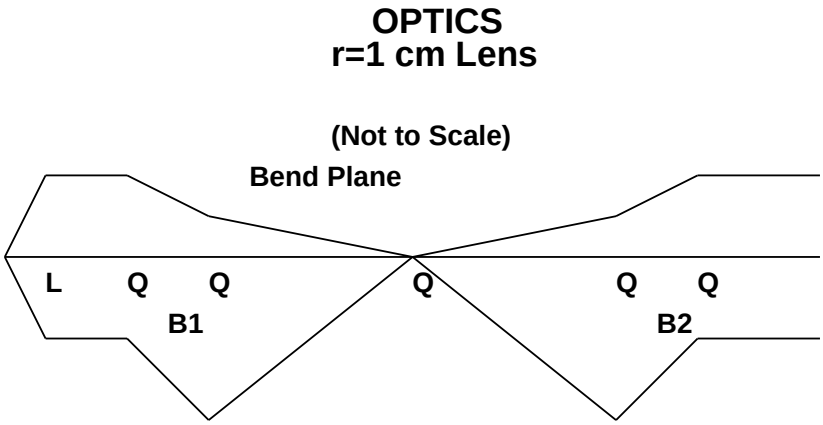

Figure 3.20: The Narrow Band Beam design optics. L is the Li-lens, Q are quadrupoles and B1 and B2 are the two bends. The upper trajectory is the vertical (bend plane) while the bottom is the horizontal trajectory.

3.4.5 NBB Tunes and Neutrino Event Rates

The NBB can be tuned to various momenta, by changing the focal length of the lithium lens, keeping its gradient constant, and then scaling the currents in the dipoles and quadrupoles. This retains the highest acceptance while moving only the target position, keeping the lithium lens and downstream magnets at fixed positions. The optics of the primary protons are adjusted to move the waist in z as the target location moves. In a design that is tuned for 30, 45 and 60 GeV/c parent particles, the corresponding distances (target to the upstream end of the lithium lens) are 0.605 m, 0.934 m, and 1.253 m, respectively. Since the depth of field for a lithium lens is very short compared to the Double Horn System, the NBB target will be different from the WBB design. It will be a shorter and higher density–about one interaction of nickel, like the Fermilab $\overline{p}$ target. The lithium lens is 15 cm long with a 1 cm radius; the gradient is 1000 T/m. Both of these are practical values based on the existing $\overline{p}$ lens at Fermilab. At 60 GeV/c, the bending magnets run at a comfortable 1.5 T, and the field at the quadrupole tip is ~1.2 T. NUADA runs at 30, 45 and 60 GeV/c give the muon neutrino event rates and are plotted in Figure 3.21. Absorption in the lithium has been taken into account.

Tables 3.4, 3.5, 3.6 and 3.7 list the expected CC ν_μ and CC and QE ν_τ event rates at Soudan for a kT-yr for no oscillations and oscillations with $\sin^2 2\theta = 1.0$ and the Δm^2's of Figure 3.14. As is expected from the oscillation probability curves of Figure 3.14 the NBB is very powerful for specific combinations of energy and Δm^2.

Δm^2	CC ν_μ	CC ν_τ	QE ν_τ
0	109	0	0
1×10^{-1}	82	1	0
8×10^{-2}	80	1	0
6×10^{-2}	68	2	0
4×10^{-2}	68	2	0
2×10^{-2}	82	1	0
1×10^{-2}	12	4	5
5×10^{-3}	56	2	2

Table 3.4: Expected number of muon and tau neutrino events in a kiloTon-year at Soudan for $\sin^2 2\theta = 1.0$ and various values of Δm^2 for the 15 GeV π^+ NBB.

Δm^2	CC ν_μ	CC ν_τ	QE ν_τ
0	394	0	0
1×10^{-1}	149	59	10
8×10^{-2}	270	32	5
6×10^{-2}	92	75	12
4×10^{-2}	326	18	2
2×10^{-2}	29	91	15
1×10^{-2}	212	43	8
5×10^{-3}	339	12	2

Table 3.5: Expected number of muon and tau neutrino events in a kiloTon-year at Soudan for $\sin^2 2\theta = 1.0$ and various values of Δm^2 for the 30 GeV π^+ NBB.

Δm^2	CC ν_μ	CC ν_τ	QE ν_τ
0	506	0	0
1×10^{-1}	126	133	12
8×10^{-2}	252	87	8
6×10^{-2}	401	38	3
4×10^{-2}	118	136	12
2×10^{-2}	164	114	11
1×10^{-2}	389	38	4
5×10^{-3}	474	10	1

Table 3.6: Expected number of muon and tau neutrino events in a kiloTon-year at Soudan for $\sin^2 2\theta = 1.0$ and various values of Δm^2 for the 45 GeV π^+ NBB.

Δm^2	CC ν_μ	CC ν_τ	QE ν_τ
0	419	0	0
1×10^{-1}	247	70	4
8×10^{-2}	330	39	2
6×10^{-2}	174	103	6
4×10^{-2}	44	152	9
2×10^{-2}	225	75	5
1×10^{-2}	360	22	1
5×10^{-3}	403	5	0

Table 3.7: Expected number of muon and tau neutrino events in a kiloTon-year at Soudan for $\sin^2 2\theta = 1.0$ and various values of Δm^2 for the 60 GeV π^+ NBB.

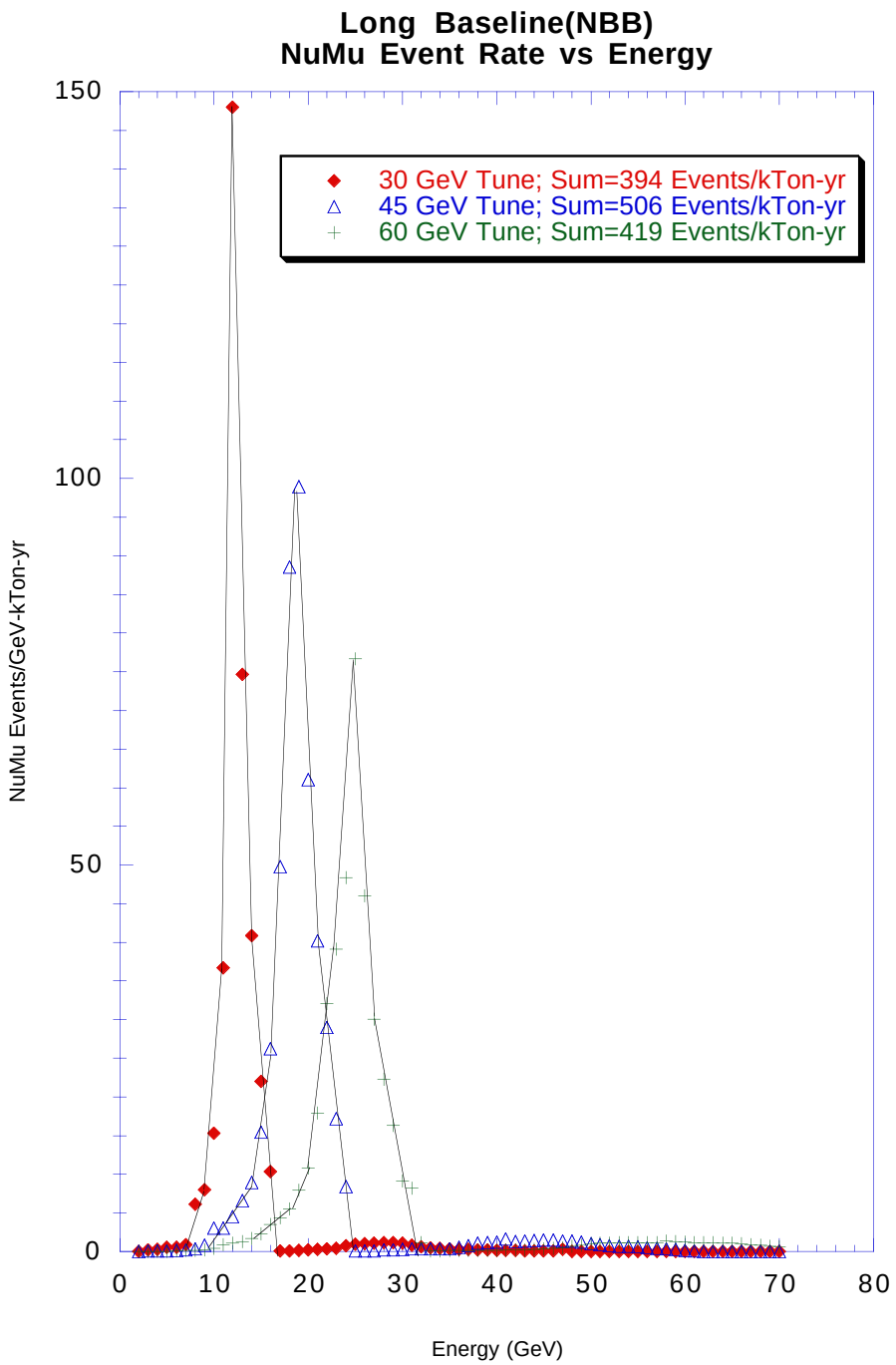

Figure 3.21: The Narrow Band Beam CC ν_μ event rates at the far detector.

3.4.6 NBB backgrounds

For the goals of E–875 the ideal NBB is one that is composed only of ν_μ's with energies close to the nominal value. Low energy ν_μ's or ν's of other species constitute background. Since the NBB is still being optimized, no rigorous quantitative statements can be made at this time about the level of different backgrounds. However, we can make some semi-quantitative statements based on the more mature studies of WBB backgrounds, experience with other NBB designs, and the work to date on the NuMI NBB.

Low energy ν_μ's

One of the MINOS design goals for the NBB is to minimize the low energy tail of the beam energy spectrum. The current design is still not completely satisfactory in that regard, and work is continuing on further optimization. There are several possible sources of low-energy ν_μ in the NuMI neutrino beam:

1. Nonparallel pions, *i.e.* those traveling at a finite angle to the beam axis, constitute the most important source of low-energy ν_μ's. In the NBB, neutrinos, from these pions, that reach the far detector must be produced at a finite angle, and therefore at less than the maximum energy.

2. Low momentum pions in the decay region itself produce low-energy ν_μ. Because the NBB design requires the final hadron beam to point at a finite angle to the proton beam direction, very few ν's from decay of off-momentum mesons should be seen by our detectors.

3. Third generation ν_μ's, coming from processes like $K^+ \to \pi^+\pi^0$ (or $\to \pi^+\pi^+\pi^-$) followed by $\pi^+ \to \mu^+\nu$ also produce low-energy ν_μ.

4. Semileptonic decays of K^+ constitute an irreducible low-energy beam component. This is estimated to be roughly 0.2% of the total ν flux, but only a small fraction of these neutrinos have less than the nominal ν beam energy.

An optimized NBB design will reduce the first three contributions as much as possible, perhaps requiring some trade-offs with the total flux. There appears to be some advantage in keeping the transverse dimensions of the upstream end of the decay pipe as small as possible, so as to be able to provide effective collimation for decay particles (*e.g.* π's from $K \to \pi\pi$). The production target needs to be optimized to provide minimum phase space consistent with a large flux of secondary mesons. Finally, the bending magnets and/or quadrupoles might be mistuned slightly between the two stages of magnetic analysis to make the lower momentum component of the pion beam as parallel as possible.

Neutrinos of other species

Because the NBB direction is at 14 mr with respect to the incident proton beam, ν_τ's coming from the short-lived secondaries made in the target constitute a negligible contamination. Similarly no significant sources of $\overline{\nu}_e$'s exist in the NBB at the 10^{-3} level. Thus we focus here on $\overline{\nu}_\mu$ and ν_e contamination. Probably the principal source of the $\overline{\nu}_\mu$ and ν_e component

is muon decay. The former are not a problem because they will be recognized most of the time by the presence of wrong sign muons, and their cross section is down by a factor of about 2.5 compared to ν_μ. The $\overline{\nu}_\mu$'s will also prove to be a useful monitor of the size of the ν_e component. Another source of $\overline{\nu}_\mu$'s is the decays of π^-'s from $K^+ \rightarrow \pi^+\pi^+\pi^-$. This contribution is also expected to be below the 10^{-3} level.

The ν_e component receives roughly equal contributions, about 0.25% each, from both μ decays and K^+ semileptonic decays. The muon source might be reduced slightly by installing defocusing toroids around the beam at several places in the decay pipe. This method, which is currently under study, would be effective only if the radial π and μ distributions are significantly different.

3.5 Replacement of Failed Components

The location of all connections at the top of the shielding means that, for well designed shielding, there is personnel access to the connections. The two elements most likely to fail are the first horn in the WBB and the lithium lens in the NBB. First, we'll describe replacing the horn and then describe replacing the lithium lens.

The replacement of the horn can be quickly accomplished due to the horn support design described in Section 3.3.5. Radiation safety concerns will be described in the next Section but access to the hall can occur after one day of beam off for the rapid replacement of a failed element. Upon entering the hall the horn power, water, and instrumentation will be disconnected at the top of the shielding. The shielding blocks above the horn will be removed using the target hall overhead crane and placed in a location far enough from the personnel so as to provide minimal radiation exposure. See Figure 3.23 for a drawing of this. The removal of the blocks will be done from a remote location within the hall. The horn lifting fixture will be attached to the horn. A pair of simple J shaped hooks on the lifting fixture and eye bolts on the horn can accomplish this. The hydraulic clamps holding the horn will be retracted and the horn will be lifted out and placed in a coffin. The new horn assembly will then be put onto the alignment table utilizing the alignment pins to accurately place it and then it will be clamped in place, and the shielding blocks replaced. The horn power, water, and instrumentation will be reconnected and tested. After successful tests are carried out and alignment verified the horn will be ready for service.

The replacement of the NBB proceeds in an identical manner except for the hydraulic clamping. The fact that the lens is held in place by its weight and stand implies that one just attaches its lifting fixture to it and lifts the lens out. The lens stand has alignment pins that will guide it back into place when the new lens is installed. The experience of the Fermilab anti-proton source group and their procedures for replacing a lens will guide the NuMI group in its procedures.

3.6 Radiation Handling and Shielding

The protons from the Main Injector produce an average of 7-10 mesons for each proton interacting in the target. These mesons are produced at angles up to $\sim$ 100 mrad. In order

to prevent activation of the target hall the beam lines must be shielded with suitable material. We have modelled a standard year of running for the NuMI beams as having 4×10^{13} protons on target every 1.9 seconds, 39 operating weeks per year with 125 hours of operation per week. This model has 3.7×10^{20} protons on target for a standard operating year. We have used this number of protons on target per year for all of our radiation shielding calculations.

The materials to use for shielding are chosen to minimize the size of the target hall and to allow relatively rapid personnel access to the hall after beam is turned off. Figure 3.22 shows the curves for residual activity as a function of the number of days since beam is turned off after a year of running for Fe (steel), Al, and $CaCO_3$ (calcium carbonate). Steel is very good for radiation shielding since it has a high density and low cost but it takes 85 days for the residual activity to cool by a factor of 10. Calcium carbonate, on the other hand, has residual activity that has cooled by a factor of 30 in 10 days. We have chosen these two materials, steel and calcium carbonate, as the shielding of choice for the NuMI target hall. Wrapping the steel shielding with calcium carbonate, marble or limestone, will allow personnel access to the hall relatively rapidly. The residual activity decreases by a factor of 10 the first day.

The shielding concept for the target and beam lines includes the use of modular shielding blocks of steel and calcium carbonate placed around the beam line elements. Radially out from the calcium carbonate will be one meter of steel and an additional one half meter of calcium carbonate. The WBB will have one meter of calcium carbonate in the area between the horns. These shielding materials and thicknesses will allow personnel access to the target hall with the beam off. The thickness of each shielding material is chosen such that the calculated dose rate will be $\sim$ 10 - 100 mrem/hour with the beam off. The modular design of the shielding allows rapid disassembly in order to replace failed components or switch beams using the overhead crane in the target hall. Figure 3.23 illustrates the design of the shielding and shows how access to the horn is possible with the removal of a few of the shielding blocks.

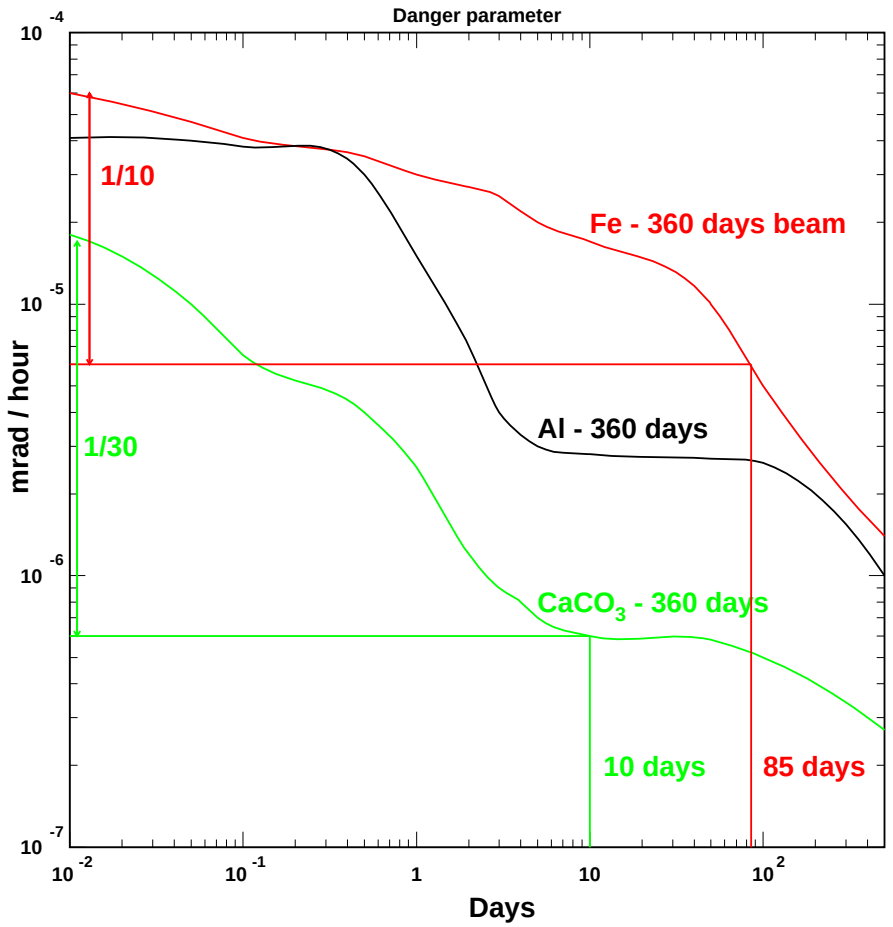

Figure 3.22: The danger parameter curves from the Fermilab Radiological Control Manual for Fe, Al, and $CaCO_3$ for 360 days of beam.

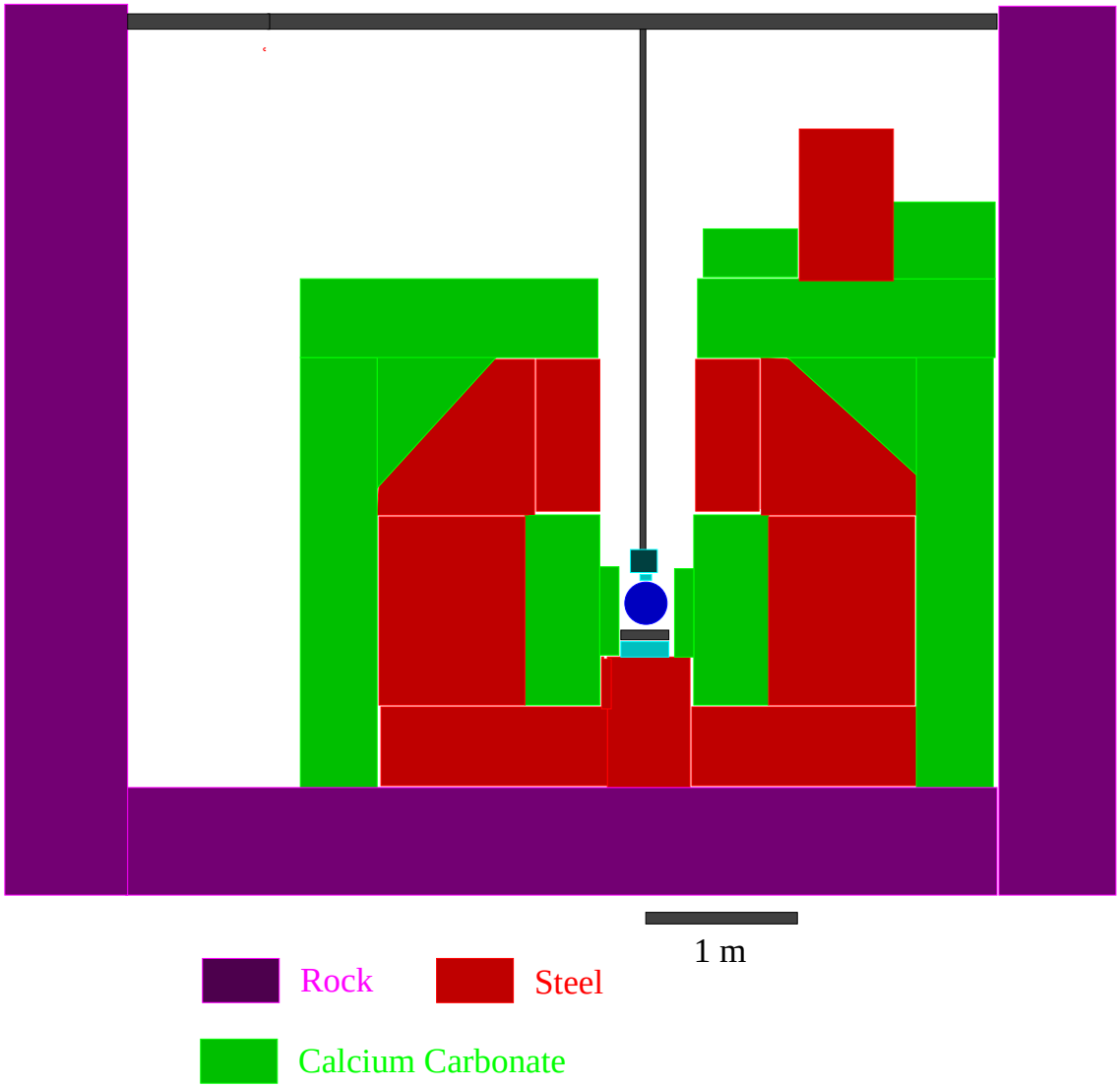

Figure 3.23: The shielding design for the NuMI first horn with pieces removed and stacked showing the access to the horn.

3.7 Switching between Wide–band and Narrow–band beams

The primary proton beam from the Main Injector travels through a two foot diameter beam pipe into the pre-target hall. The WBB primary proton beam must be on the beam axis pointing to Soudan. However, since the NBB has its bend plane in the vertical plane, the NBB primary proton beam has a trajectory that is approximately one foot higher than the WBB at the target. The switch from the WBB to the NBB will require that all of the pre-target dipoles and quadrupoles move up so that the primary protons will strike the NBB target. The magnet stands for the pre-target beam line will be designed so that the vertical movement necessary to switch beams will be to pre-determined locations. The method chosen will allow precise alignment for each beam and the movement and final location will be repeatable within the desired precision.

The targets for the WBB and NBB are different designs. The depth of field for the focus of the horn allows the use of a long thin target while the depth of field for the focus of the lithium lens requires a more conventional target. The target shield, very similar in design to the horn shield, is designed to allow the placement and removal of the NBB target in minimal time and with minimal radiation exposure. Shielding blocks will be rearranged at the target location to accomplish this.

Figures 3.24 and 3.25 illustrate the minor shielding configuration changes necessary to switch from the WBB to the NBB. For ease of switching the beams the calcium carbonate surrounding Horn 1 will be made 0.75 m thick with the inner radius piece 0.25 m thick. The inner piece will be removed and stored in a safe location in order to install the lithium lens, quadrupole Q1 and dipole B1. The alignment base that Horn 1 sits on will be designed to hold the lithium lens and the first quadrupole in a pre-aligned position. The conventional magnet stands will be permanently installed. The supports for the He filled beam pipes present in the WBB will be designed to accept the B1, Q2, Q3, Q4, B2 and Q5 magnet stands as an addition to them. Both the WBB and NBB will need to be installed and aligned before any beam is put on target in order to insure that a switch between them will allow the placement of the beam elements onto pre-determined locations.

When the decision is made to switch from one beam to the other the proton beam will be turned off. The target hall, with calcium carbonate as a component of the shielding, will need to cool off for 7-10 days before personnel will be allowed to enter the hall for the purpose of switching the beams. (The full cool off period is not required for the replacement of a failed horn or lithium lens since the replacement system for them is designed to allow remote handling and minimal radiation exposure to personnel). After the 7-10 day radiation cool off period, it is estimated that 9 shifts over a minimum of 5 days will be necessary to switch the WBB to the NBB. The work will begin at the downstream end of the hall and proceed upstream to allow further radioactive decay to cool off the more highly activated elements closer to the target. The need for additional radiation protection, such as lead curtains over radiation hot spots, is currently being evaluated.

The NBB proton dump will be placed in the initial installation of the beam line and remain there until the line is disassembled. The dump will have a removable core that allows the WBB second horn to fit. The view of the beam lines shown in Figure 3.26 illustrates

why the removable core is necessary. The NBB dump, in the current design, is at the same location as the second horn in the WBB. When the NBB is installed the core will be replaced after removal of the second horn and its alignment base. It may be the last element of the NBB to be installed since with it absent there is line of sight horizontally for alignment. An alignment strategy that will allow verification that the elements are in the proper location will be adopted after discussions with alignment experts.

The design of the beam elements and their supports will allow the neutrino beam to be switched from WBB to NBB in approximately 2-3 weeks of calendar time. Careful engineering of the two beam lines with a design goal which includes ease of installation is critical for adhering to this replacement time estimate. The major stumbling block to a more rapid replacement is the radiation cool off period necessary before extensive personnel access. The choice of calcium carbonate as a shielding material makes the cool off time as short as possible.

3.8 Maintenance of the neutrino beamline

The components of the beamline which have the highest frequency of trips and failures are the power supplies. All supplies will be housed in a sub-basement of the target service building and will be immediately accessible at all times. MOst of the power, water and instrumentation connections to the beam line elements will be made outside of the shielding. The few connections that are within the shielding and, therefore, within a high radiation environment will be designed to be radiation hard. The replacement of a failed beam line element can be accomplished in a timely manner, as has been described for the switching of the WBB to the NBB. There are design criteria for the replacement of the beam elements judged most likely to fail and a well designed beam will be one in which any failure may be quickly rectified.

The ability to keep the beam line operational depends on the reliability of the components. The design specifications for each will include the current knowledge of radiation hard materials and possible failures due to radiation exposure.

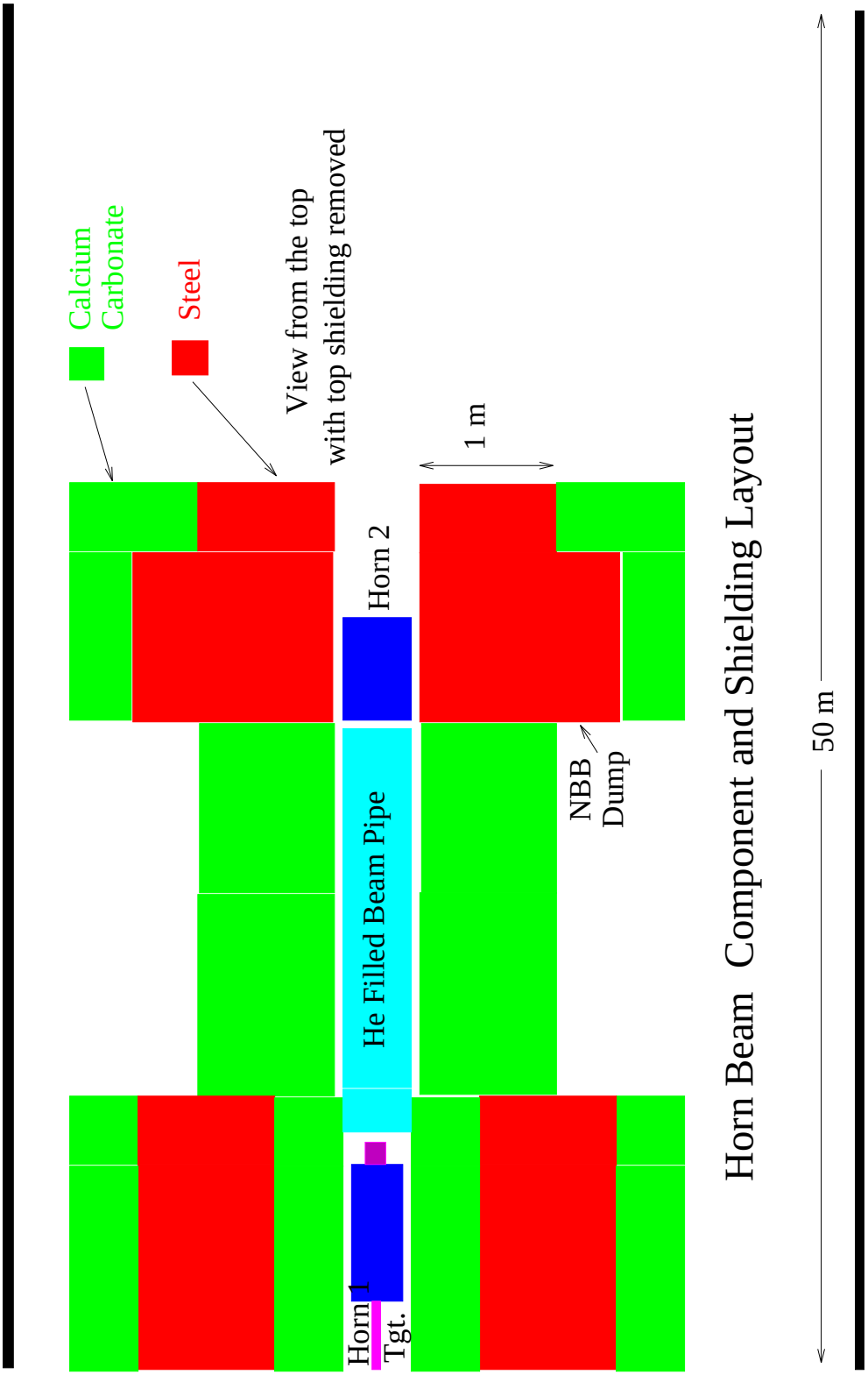

Figure 3.24: The layout of the WBB and the shielding design for it viewed from the top with the top shielding removed.

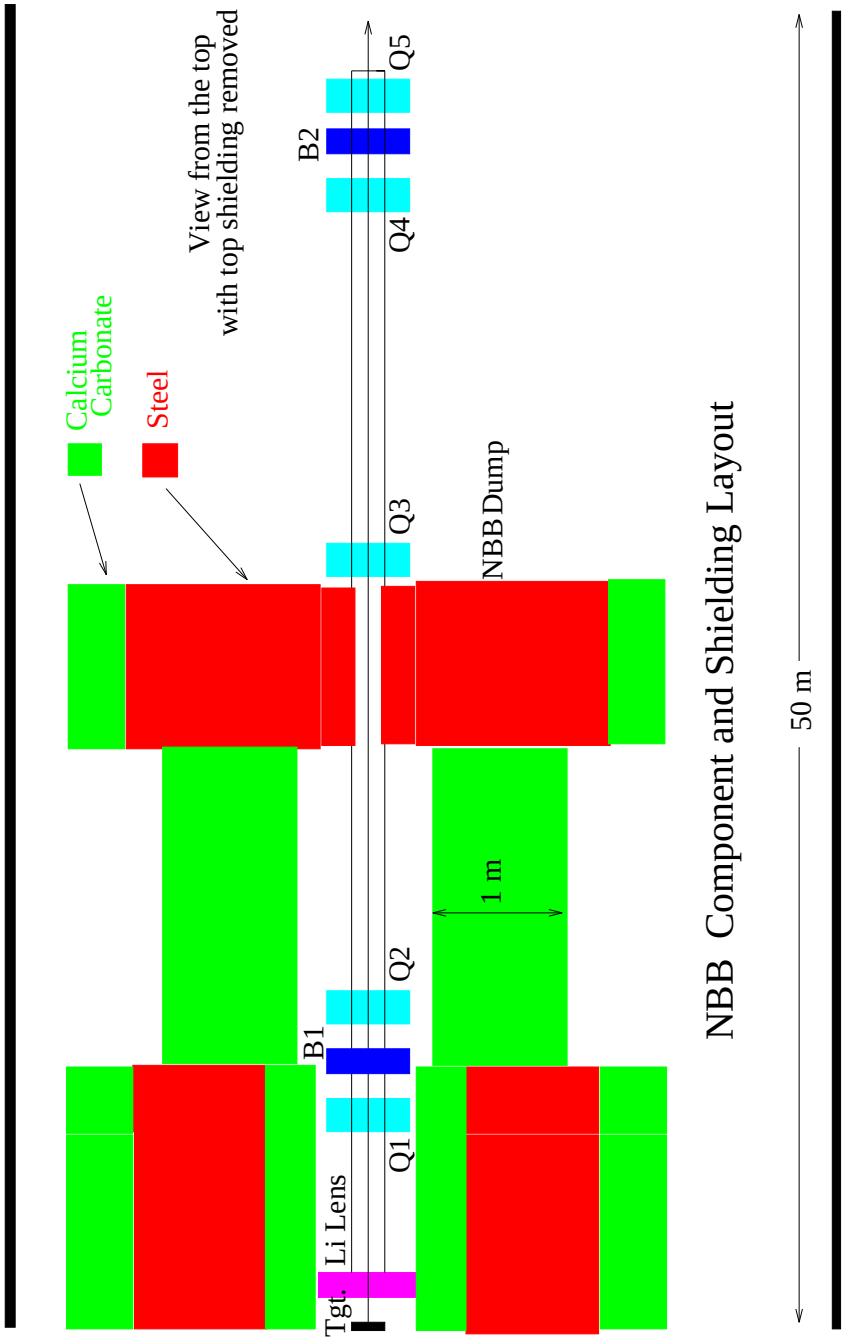

Figure 3.25: The layout of the NBB and the shielding design for it viewed from the top with the top shielding removed.

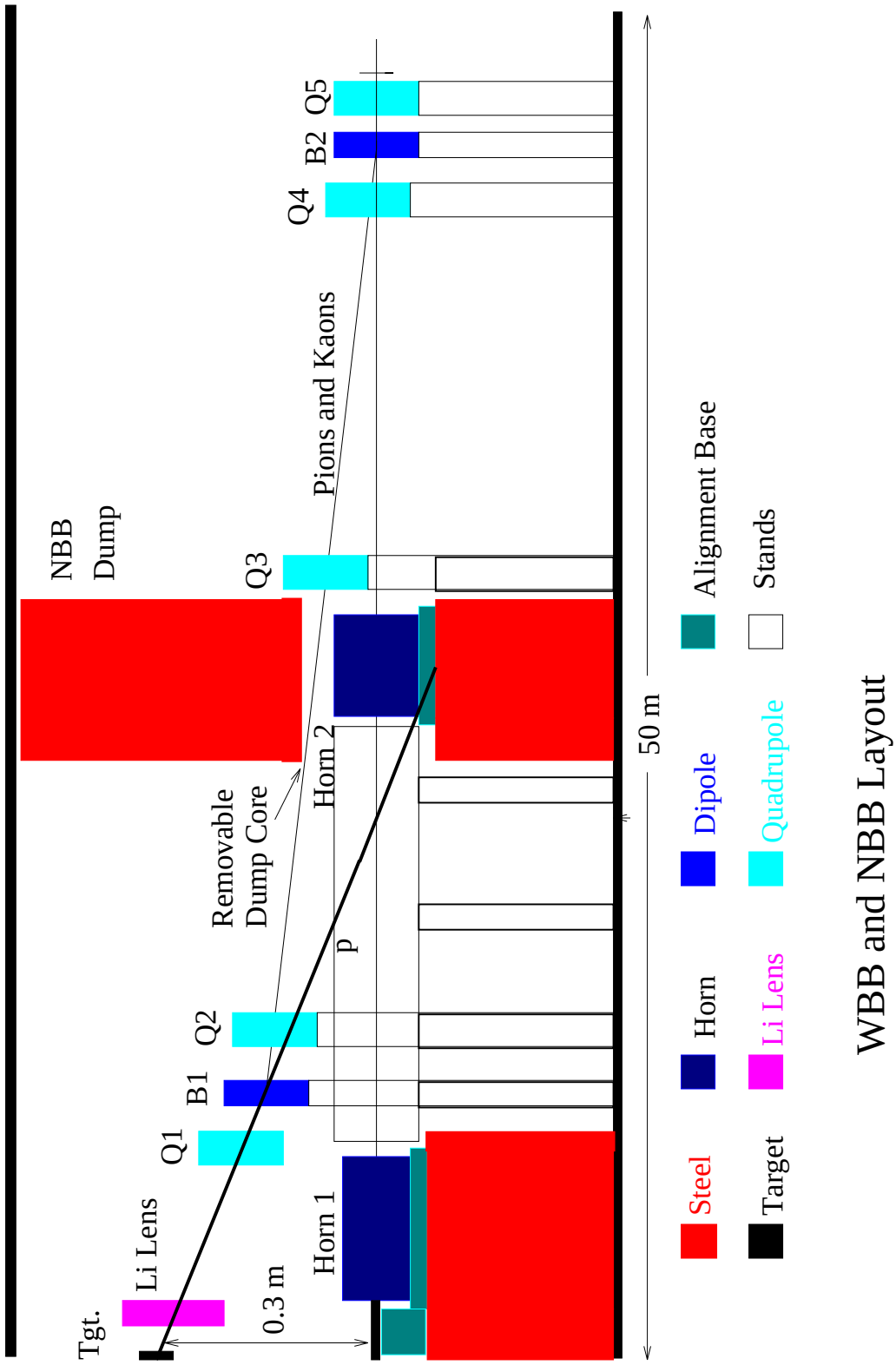

Figure 3.26: The layout of the WBB and NBB with the location of the NBB dump shown.

Chapter 4

The Target for the Wideband Beam

4.1 Secondary Particle Production

Secondary particle production has been investigated for the combined target/double horn system using NUADA and secondary particle production of FN-341. The production target is modeled after a CERN design[33], except the beryllium rods are replaced with graphite rods. Because the double horn system has a large depth of field (see Section 3.3.3), a small radius target extended in z will give the highest rates. Table 4.1 summarizes several different configurations. Each configuration was optimized with respect to the depth of field. Clearly the large radii targets absorb a large fraction of the particles that emerge out the side of the small radii targets. For the 2 mm and 3 mm targets 100 cm long, the configurations with gaps is better than those with no gaps. To some extent, the increased number of particles coming out the side is offset by the decrease which comes about from less average depth of field with the gaps. Non-interacting protons travel the entire length of the decay pipe and end up in the dump where they create backgrounds for the experiments. It is therefore desirable to have a long target to interact as many protons as possible.

z(begin)	Graphite	Gaps	Events	$< E >$
-1.2 m	48 cm; r=2 mm	none	0.78	25.2 GeV
-1.2 m	48 cm; r=10 mm	none	0.66	23.2 GeV
-1.2 m	100 cm; r=2 mm	none	0.90	22.1 GeV
-1.2 m	100 cm; r=3 mm	none	0.76	21.9 GeV
-1.2 m	100 cm; r=10 mm	none	0.50	22.6 GeV
-1.6 m	100 cm; r=3 mm	56 cm	0.89	22.7 GeV
-1.6 m	100 cm; r=2 mm	56 cm	1.00	22.9 GeV
-1.6 m	100 cm; r=1 mm	56 cm	1.20	23.2 GeV

Table 4.1: Event rate for various targets. z = 0 is the upstream end of Horn 1.

Melting temperature	3600° C
Sublimation temperature	3320° C
Density ρ(gm/cc)	1.81
Specific heat c(cal/gm-°C)	0.17
Coefficient of thermal expansion (/°C)	7.7×10^{-6}
Thermal Conductivity (cal/sec-cm-°C)	0.29
Modulus of elasticity Y(psi)	2.1×10^{6}
Flexural strength (psi)	18000
Compressive strength (psi)	28000
Tensile strength (psi)	13000
Strain to failure (%)	0.78
Poisson's Ratio	0.2 @ 1000° C

Table 4.2: Properties of ZXF-5Q Graphite.

4.2 Energy Deposition

Energy deposition by the proton beam in the graphite ZXF-5Q[34] has been calculated using CASIM[35] and properties from Table 4.2. The beam size on the target (σ) is related to the physical radius of the target (R) by, $\sigma = R/2.248$. This value ensures that 92% of the incoming protons strike the target. σ and R are decreased together, so that for $R = 1$ mm, 2 mm, 3 mm, the beam sigmas are 0.45 mm, 0.89 mm, and 1.33 mm. A series of thin graphite cylinders are modeled, separated longitudinally by equal spaces. Eight graphite cylinders, each 12.5 cm long are equally interspersed with seven 8 cm gaps, to give a length of 1.56 meters for the entire system (see Figure 4.1).

The radial energy distribution E(r) as given by CASIM has the characteristic that the density increases as the radius decreases. Of interest is the maximum energy density, usually called E_0. For a cylindrical rod, E_0 is the density at the center of the target. The radial energy deposition is the largest for the first (most upstream) 12.5 cm segment. The values for E_0 are 0.46 GeV/cc, 0.15 GeV/cc, and 0.07 GeV/cc for target radii of 1 mm, 2 mm, and 3 mm respectively.

4.3 Temperature Distribution and Cooling

The maximum temperature rise for one pulse is obtained from E_0 and the properties of the target as found in Table 4.2 according to,

$$T(^\circ C) = 3.82 \times 10^{-11} N_p pp(protons/pulse) \frac{E_0(GeV/cc)}{c\rho} \tag{4.1}$$

For 4×10^{13} incident protons, the maximum temperature rise at the center of the graphite for 1 mm, 2 mm, and 3 mm targets is 2285° C, 745° C, and 350° C. This is an over-estimate because the specific heat for graphite is not constant, but is a function of temperature[34].

It rises from 0.17 cal/gm-°C at room temperature to about 0.4 cal/gm-°C at 700° C to about 0.5 cal/gm-°C at 2000° C. The temperature distribution is schematically represented in Figure 4.2. After several pulses, the steady state has been achieved, and the maximum temperature is just the temperature rise for a single pulse on top of the steady state temperature. The following set of equations is solved to find the temperature as a function of time:

$$\frac{dT}{dt} = \frac{Q}{T_S} - \frac{2K_R}{c\rho R}(T^4 - T_0^4) - \frac{2K_c}{c\rho R}(T - T_0) \quad 0 \leq t \leq T_S \tag{4.2}$$

$$\frac{dT}{dt} = \frac{2K_R}{c\rho R}(T^4 - T_0^4) - \frac{2K_c}{c\rho R}(T - T_0) \quad T_S \leq t \leq T_C \tag{4.3}$$

T = the temperature.

t = time.

Q = heat deposited in one pulse during the spill time.

T_S = spill time.

T_C = cycle time.

c, ρ, R = specific heat, density and radius of the target material.

T_0 = initial temperature.

K_R = radiation constant (emissivity and Stefan-Boltzmann constant).

K_c = convection constant.

Beginning with the boundary conditions that T_0 at t = 0 is room temperature, the first equation gives the temperature at the end of the beam spill, that temperature is used as the boundary condition for the second equation to find the temperature at the end of the cycle. Repeating the process for several cycles (usually less than 20), one arrives at the steady state solution modeled in Figure 4.2. The maximum temperature for black body radiation, radiation plus natural helium convection, and radiation plus forced convection (helium flow at 4 meter/sec) is given in Table 4.3. Following the 1 msec spill, the heat at the center distributes itself uniformly throughout the target volume by thermal diffusion. The time required for the RMS value of the radial temperature distribution to be equal to the radius of the target is 6 msec, 22 msec, and 48 msec for the 1 mm, 2 mm, and 3 mm targets respectively.

4.4 Stresses

Quasi-static and dynamic thermal stresses must also be considered. Dynamic stresses give rise to shock waves which occur when the heating time of the material is comparable to the time it takes sound to propagate along the target. For a 1 msec spill and a target segment length of 12.5 cm, the dynamic stresses are 175 psi (negligible), compared with the

Target Radius	Radiation Only	Radiation and Natural Convection	Radiation and Forced Convection
1 mm	3250 °C	3080 °C	2830 °C
2 mm	1900 °C	1800 °C	1600 °C
3 mm	1510 °C	1420 °C	1250 °C

Table 4.3: Maximum Temperature for various target sizes and forms of cooling where natural and forced convection uses He gas.

strength of the material. Dynamic stresses are inversely proportional to the spill length, and are significant when spill lengths are shorter than several tens of microseconds. Quasi-static stresses come about when a material is heated non-uniformly. A 1 ms fast spill creates a situation where the center material of the target is hotter than the material on the circumference. Using the formulae of [11], the maximum stress inside the target can be as high as 15,400 psi, 5020 psi, and 2360 psi for the 1 mm, 2 mm, and 3 mm radius targets respectively. This is to be compared with a flexural strength of 18,000 psi from Table 4.2.

4.5 Conclusions

Combining the results from secondary yield, and factoring in maximum temperatures and stresses, a reasonable choice for the target is one having a 2 mm radius. The incoming proton beam is tuned to have a waist at the target position. It gives the required $\sigma = 0.89$ mm spot size with a reasonable angular divergence (about 0.2 milliradians). Forced convection with helium reduces the temperature enough to make it worthwhile and is incorporated into the design. Flow interlocks on the helium will be necessary to ensure air is not in contact with the graphite. Using the cooling methods of black body radiation and forced convection with helium, the temperature profile after achieving steady state is shown in Figure 4.2 for the 2 mm target.

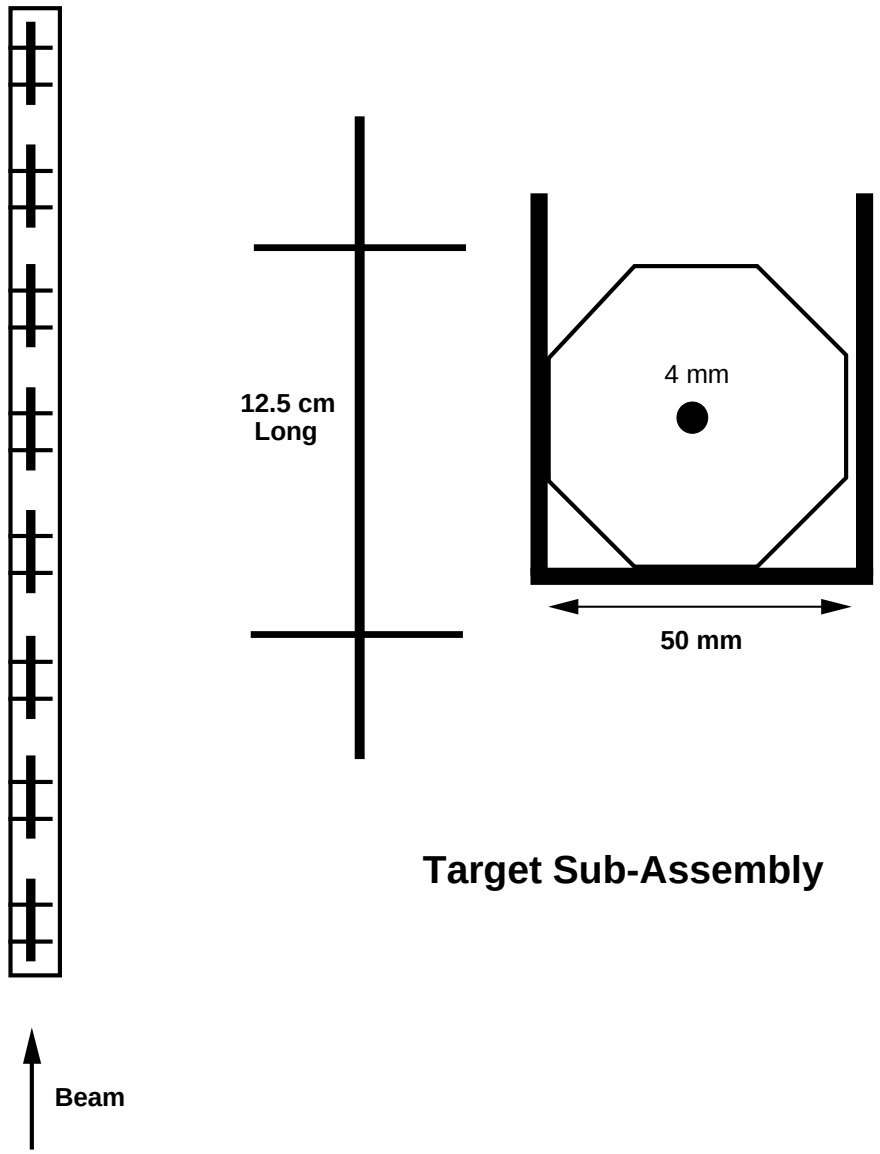

Figure 4.1: The design of the NuMI target.

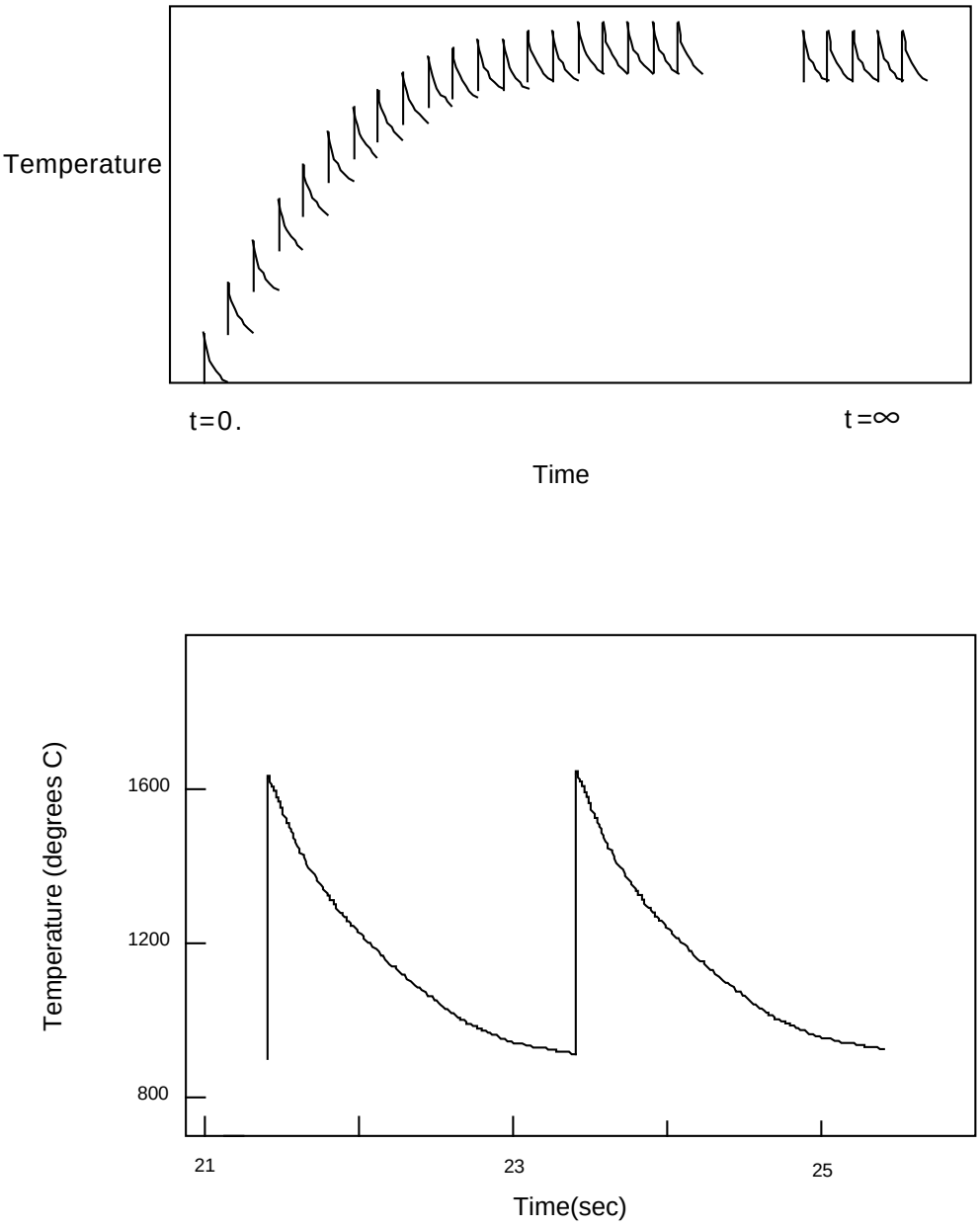

Radiation and Natural Convection using Helium for the 2 mm Target

Figure 4.2: The target temperature profile as a function of time for a) the rise to steady state and b) at steady state for two beam pulses 1.9 seconds apart.

Chapter 5

The Decay Region

The decay pipe radius and length affect the ν_μ and ν_τ event rates for both the near detector at Fermilab and the far detector at Soudan. The ν_τ event rate at the near and far detectors is calculated by assuming that the ν_μ oscillate to ν_τ with maximal mixing, $\sin^2 2\theta = 1$ and the probability for oscillation is 1/2 independent of Δm^2. The result of this assumption is that half of the ν_μ are transformed to ν_τ. However, for the NBB it is possible to tune the beam energy to the appropriate Δm^2 so the ν_τ rate will be twice the maximal mixing assumption rate. The ν_τ event rate at the long baseline detectors is then calculated using the ν_τ charged current (CC) cross section for $\nu_\tau Fe$, including the energy dependence of $\sigma_{\nu_\tau}^{CC}$. This calculation shows that the ratio of ($\nu_\mu \rightarrow$ CC ν_τ) to (CC ν_μ) is $\approx 20\%$ for the WBB.

A beam dump is located at the end of the decay region to absorb the secondaries. For the WBB as well as target-out studies, the dump is used to absorb the non-interacting protons. The dump is similar in construction to present Fermilab designs. A central water-cooled core is surrounded by steel. The outer dimensions of the steel are about 3 m x 3 m x 4.9 m long with an upstream inner core of aluminum 2.45 m long and a similar downstream core of copper. If the core size is 61 cm x 61 cm the power in the materials for standard proton intensity is Al (220 kW), upstream steel (32 kW), Cu (65kW) and downstream steel (2 kW).

5.1 Optimizing the ν_τ rate at the far detector

We studied the question of decay pipe radius by determining the ν_τ event rate at the far detector for various decay pipe radii from 0.25 m to 4 m. At the same time we studied the effect of decay pipe length by varying that parameter between 300 and 1000 m. Figure 5.1 illustrates the variation in the charged current ν_τ event rates at Soudan for different decay pipe radii and lengths for the WBB. The rates show a rapid increase with increasing decay pipe radius until a plateau is reached. The data suggest that the decay pipe radius should be optimized on or near the plateau for each decay pipe length in order to maximize ν_τ events at the far detector.

The variation of ν_τ rates for a NBB is presented in Figure 5.2. (This calculation was done for a different NBB focusing system than those presently under design, but the general dependence on decay pipe parameters should be quite similar.) The rapid event rate increase for increased decay pipe radius up to about 1 m, evident in the WBB case, is also present

for the NBB. The onset of the plateau at larger radius for longer decay pipes in both beam options shows that the decay pipe radius must be optimized for the desired decay pipe length. The number of ν_τ events for any running period and detector mass can be increased by such an optimization. The information presented in this Section indicates that for the long baseline neutrino oscillation search a decay pipe length of 1000 m with a decay pipe radius of 1.5 to 2 m provides more ν_τ events at the 732 km distant detector than for a decay pipe with a smaller radius or a shorter length. A radius of 1 m for the 1000 m long decay pipe results in approximately 10% fewer ν_τ events at Soudan. The optimization of the decay pipe length and radius must ultimately be traded off against the detector mass and cost and event rates for the final NuMI neutrino beam design.

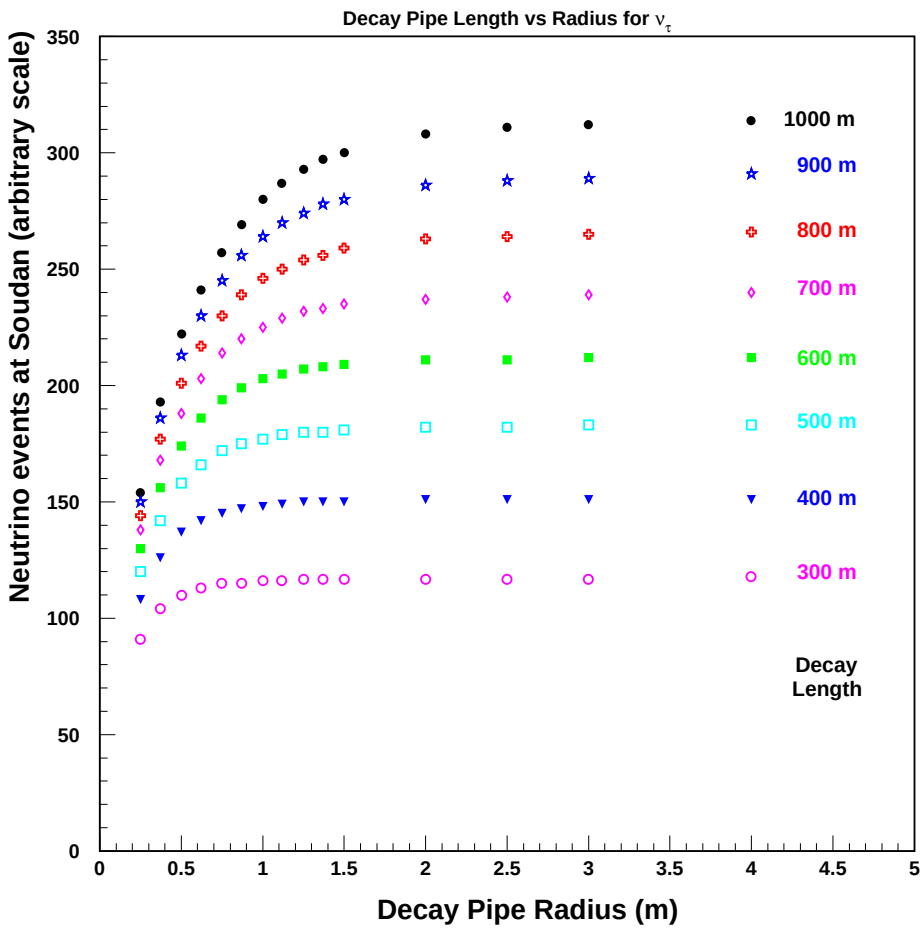

Figure 5.1: Comparison of the ν_τ event rates at Soudan for decay lengths from 300 to 1000 m and decay pipe radii from 0.25 to 4.0 m using the WBB.

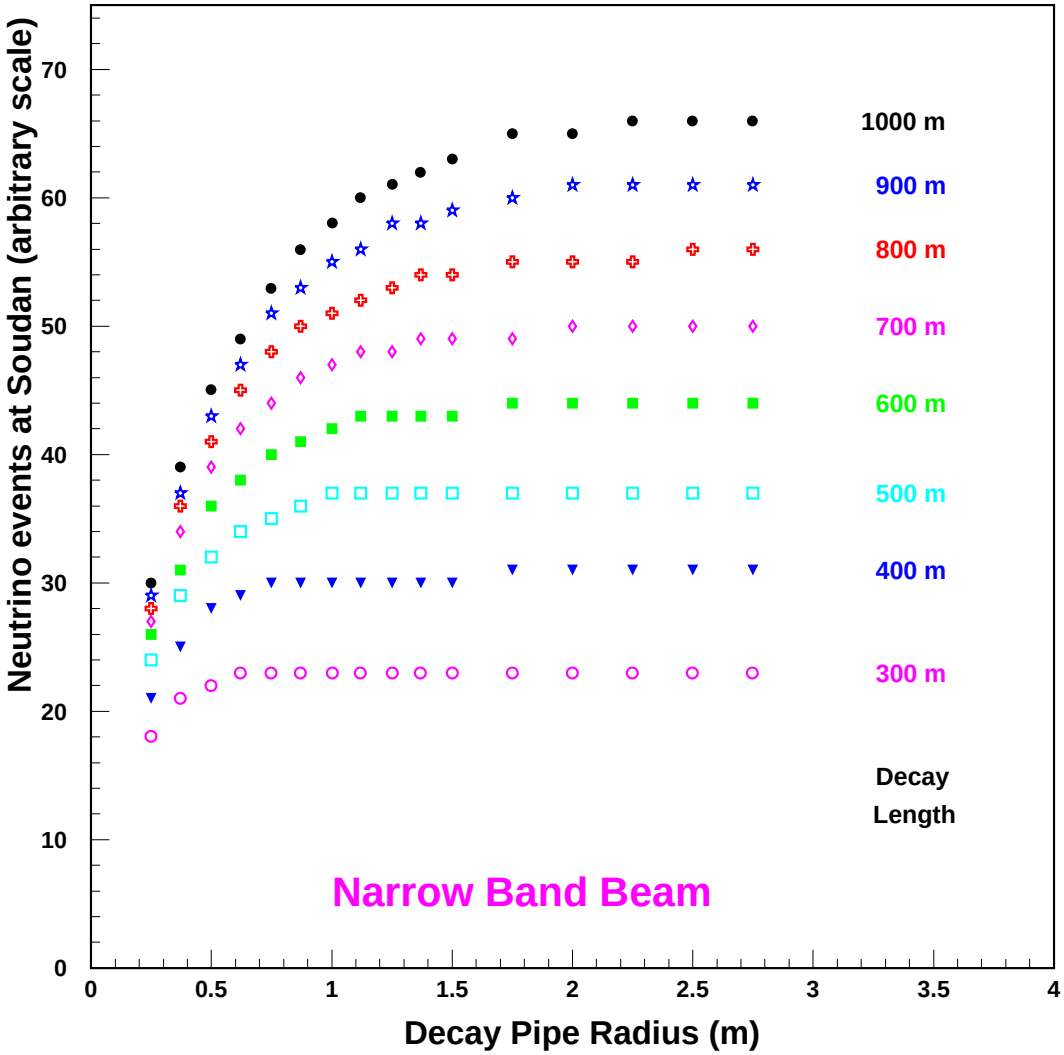

Figure 5.2: Comparison of the ν_τ event rates at Soudan for decay lengths from 300 to 1000 m and decay pipe radii from 0.25 to 3.0 m using a generic 45 GeV/c NBB.

5.2 Variation of the ν_τ rate at the near detector

Event rates for the MINOS near detector are large enough that the rates do not need to be optimized for E–875. But the decay pipe parameters also affect E–803 rates, as we describe briefly in this Section.

We have repeated the rate calculations as a function of the decay pipe parameters using a one kT iron detector with a radius of 1 m located 190 m beyond the end of the decay pipe. The results are shown in Figure 5.3 for the WBB. We continue to assume neutrino mixing with $\sin^2 2\theta = 1.0$ and one half of the ν_μ transformed to ν_τ.

The variation in event rates for the near detector behaves oppositely to that for the far detector as a function of the decay pipe length since the rate is essentially a function of the solid angle subtended by the near detector. The maximum ν_τ event rates occur for a decay pipe length of 400 m and then decrease by approximately 25% for a length of 1000 m. However, the ν_τ event rates do show the same type of dependence on the decay pipe *radius* as do the rates at the far detector but over a smaller range of radius. The optimized pipe radius for the far detector varies from 0.62 to 2.5 m as the length is changed, whereas for the near detector it varies from 1.0 to 1.5 m. The event rates at both the near and far detector suggest that a decay pipe radius of 1.0 to 1.5 m is adequate for a long decay pipe.

Discussions between E–803 and E–875 have resulted in a compromise that is suitable to both E–803 and E–875. The two experiments have agreed to use a decay pipe with a length of 800 m and a radius of 1 m as the working hypothesis. According to E–803, for the region of Δm^2 they are studying, an 800 m decay pipe is the longest pipe that they can tolerate without sacrificing their sensitivity to $\nu_\mu \rightarrow \nu_\tau$ oscillations[36]. Figure 5.4 shows that for $\Delta m^2 \leq 20$ eV^2 the longer decay pipe slightly increases E–803's sensitivity in $\sin^2 2\theta$.

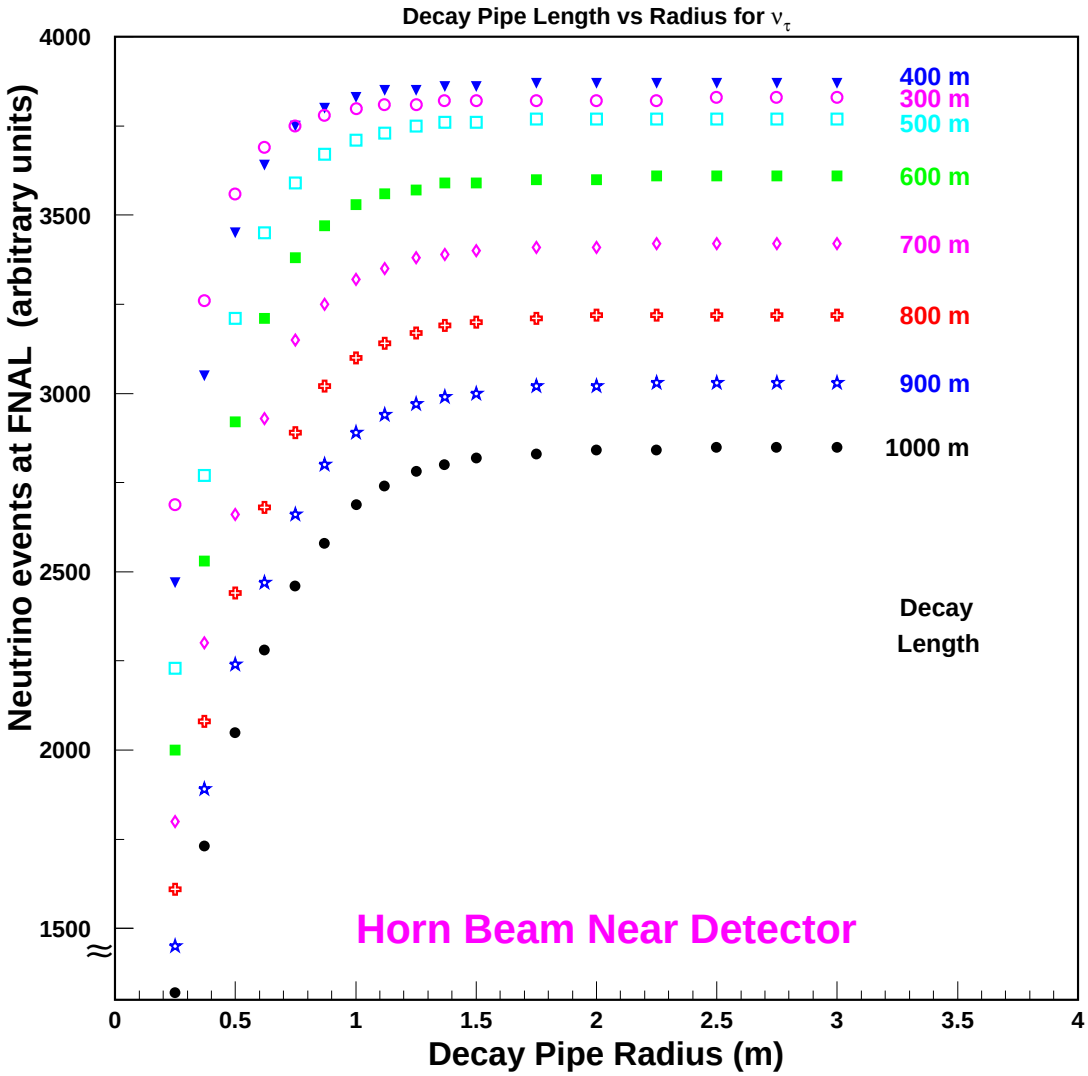

Figure 5.3: Comparison of the ν_τ event rates at Fermilab for decay lengths from 300 to 1000 m and decay pipe radii from 0.25 to 3.0 m for the WBB. Note the suppressed zero on the vertical scale.

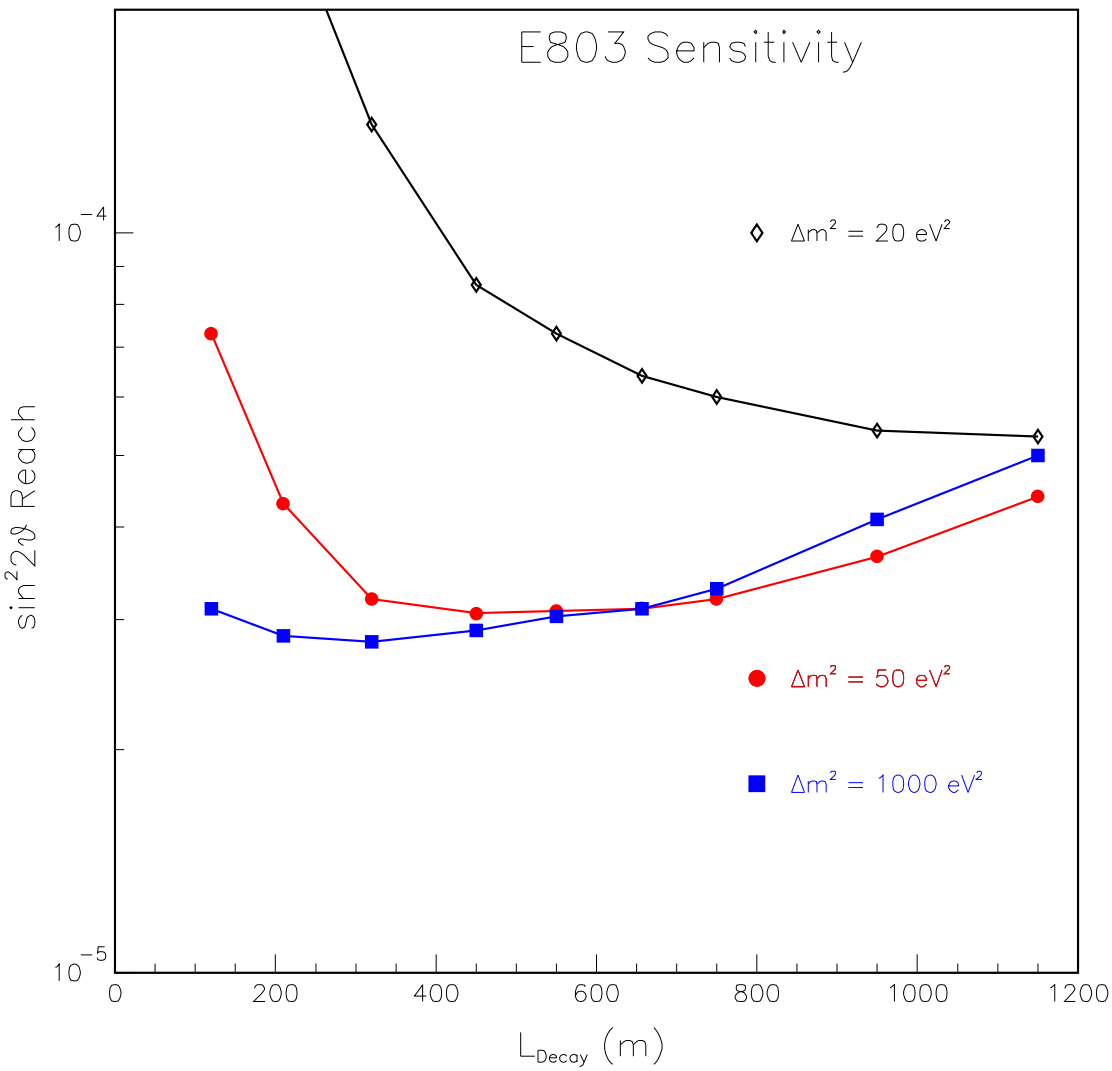

Figure 5.4: Comparison of the $\sin^2 2\theta$ sensitivity of E–803 for decay lengths from 100 to 1200 m for $\Delta m^2 = 20$, 50 and 1000 eV^2.

5.3 Precision of beam pointing to the far detector

The decay pipe must be pointed towards Soudan with high precision in order to:

- Ensure maximum intensity at the far detector,
- Minimize sensitivity to very small changes in steering which might be amplified near the edges of the beam,
- Avoid possible differences in non-ν_μ beam backgrounds from those calculated under the assumption of perfect alignment.

PBEAM and NUADA were used to obtain the profile of neutrino interactions as a function of the distance from the beam center at Soudan, which is illustrated in Figure 5.5 (a). The beam intensity is relatively flat out to about 400 m from beam center, followed by a rapid drop in intensity caused by the finite radius of the decay pipe. Our goal is to point the beam towards Soudan with a transverse precision of 100 m out of 732 km, or 0.14 mr, which should be easily attainable. The flux in the area near beam center is shown in Figure 5.5 (b). The beam spatial profile is flat out to 100 m from beam center for ν_μ events.

We have also used PBEAM to study the ν_e component of the beam as a function of distance from the beam center at Soudan. Figure 5.5 (c) shows that this important background component will not be particularly sensitive to beam steering.

There should be no fundamental difficulty in pointing the Main Injector neutrino beam (*i.e.*, the beamline components and decay pipe) with a precision of 0.14 mr towards Soudan [12]. The fact that road tunnels bored from opposite sides of a mountain (or the Channel) meet routinely with a precision of 10 cm or better is experimental evidence of the capabilities of modern surveying technology. Nevertheless, a skeptical scientific community would like to have some experimental verification of the fact that the NuMI neutrino beam is indeed pointing precisely at the MINOS detector. To address this issue we are actively exploring the possibility of placing several sets of muon counters in the Soudan mine, probably about 400 m to both sides of and also above the detector. These counters would be sensitive to muons produced by beam ν's in the rock. Comparison of these muon rates would give experimental verification of the precision of beam centering on the MINOS detector. Precise verification would require several weeks of data, although gross mis-steering would be detected faster.

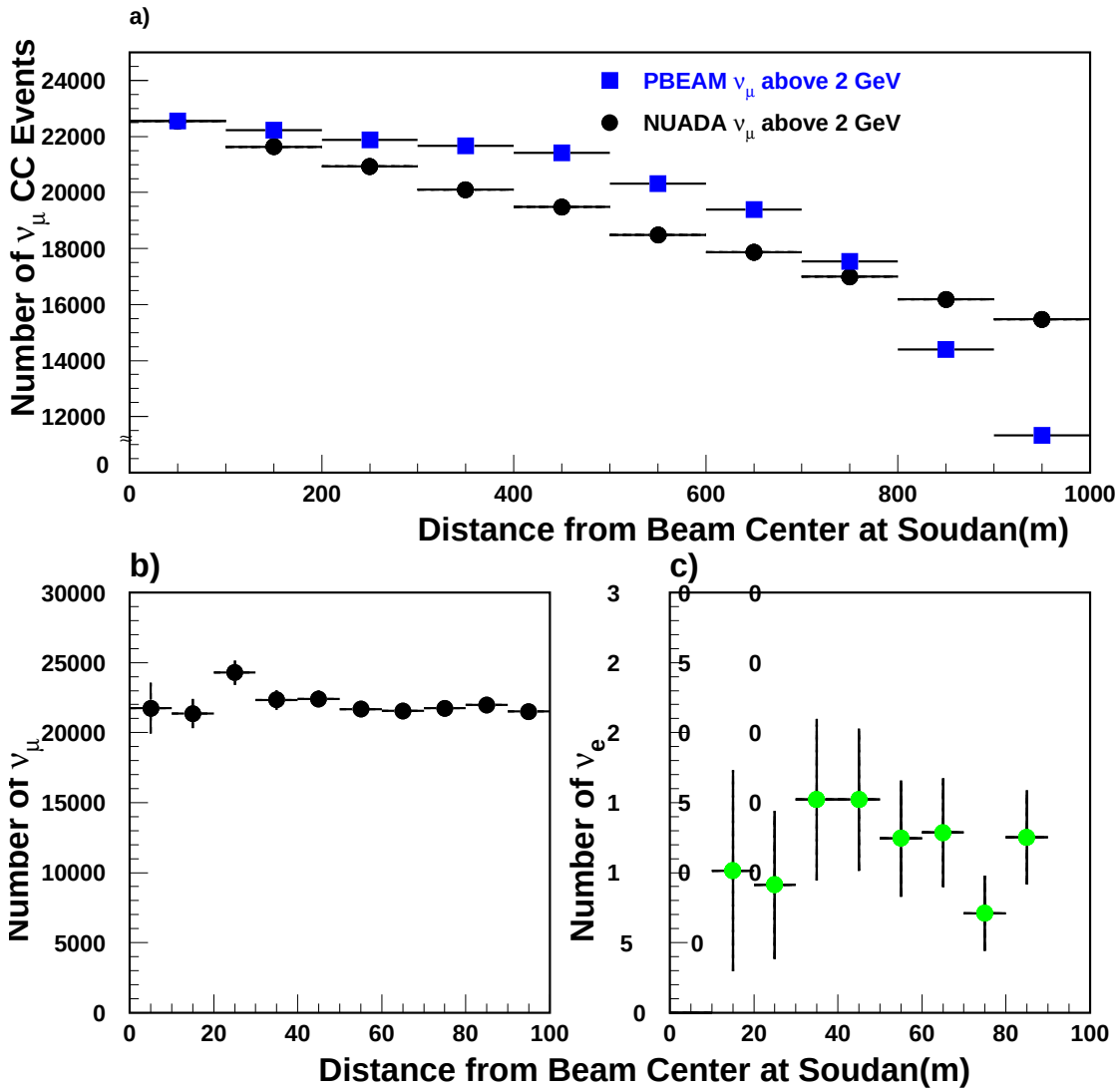

Figure 5.5: a) A comparison of NUADA and PBEAM calculations of the ν_μ beam profile at the far detector (note the suppressed zero on the vertical scale), b) The ν_μ flux normalized by the area of the 10 m bin size annulus, and c) the normalized ν_e flux *vs* distance from beam center at the far detector for a finer distance scale, using the PBEAM program. Only the relative values on the vertical scales are important.

Chapter 6

NuMI Beam Monitoring

6.1 Monitoring of the Wide Band Beam

Beam monitoring is needed to provide stable operating conditions. In order to assure accuracy of neutrino flux determinations the proton targeting and the secondary beam conditions must be consistent throughout the data taking. To assure this, using tried and tested beam monitoring devices, the targeting angle and position of the protons on target plus the profile of the secondary beam somewhat downstream of the horn will be monitored and used to establish and maintain an optimal beam tune. The ratio of secondary flux to protons on target also provides a reproducible quantity that indicates proper beamline operation.

6.1.1 The Proton Beam

The proton beam will be used as the reference trajectory for the WBB. At initial tune-up, the quadrupoles will be set to focus a waist at the center of the target by using two pre-target 0.5 mm SWICs that are separated by 8.7 meters as shown in Figure 6.1. The neutrino energy spectrum at the far detector is constant out to radial distances of about 100 meters. This leads to a beam position resolution of about 250 μm and a pointing accuracy of 0.03 mrad which meets the requirement discussed in Section 5.3.

With the target moved out of the beam the primary protons will be transported to the end of the decay pipe where their profile and position will be measured with another SWIC. For redundancy, a fourth SWIC will be located at the end of the Target Enclosure for similar purposes. However, because it has the longest lever arm, the WBB trajectory will be determined by the upstream pre-target SWIC and the final SWIC at the Dump Enclosure. After the target is moved into the beam, the two pre-target SWICs will be used to monitor the primary beam and the Dump SWIC will monitor the secondary beam. To minimize background, the SWIC at the end of the Target Enclosure will have a sufficiently large frame to be outside the acceptance. It should be pointed out that if alignment questions arise anytime after the initial tune-up, the same procedure can be used to establish the trajectory by taking out the target.

A beam current transformer and for redundancy a Beam Position Monitor (BPM) will be used to measure and monitor the intensity of the primary beam. Having two separate

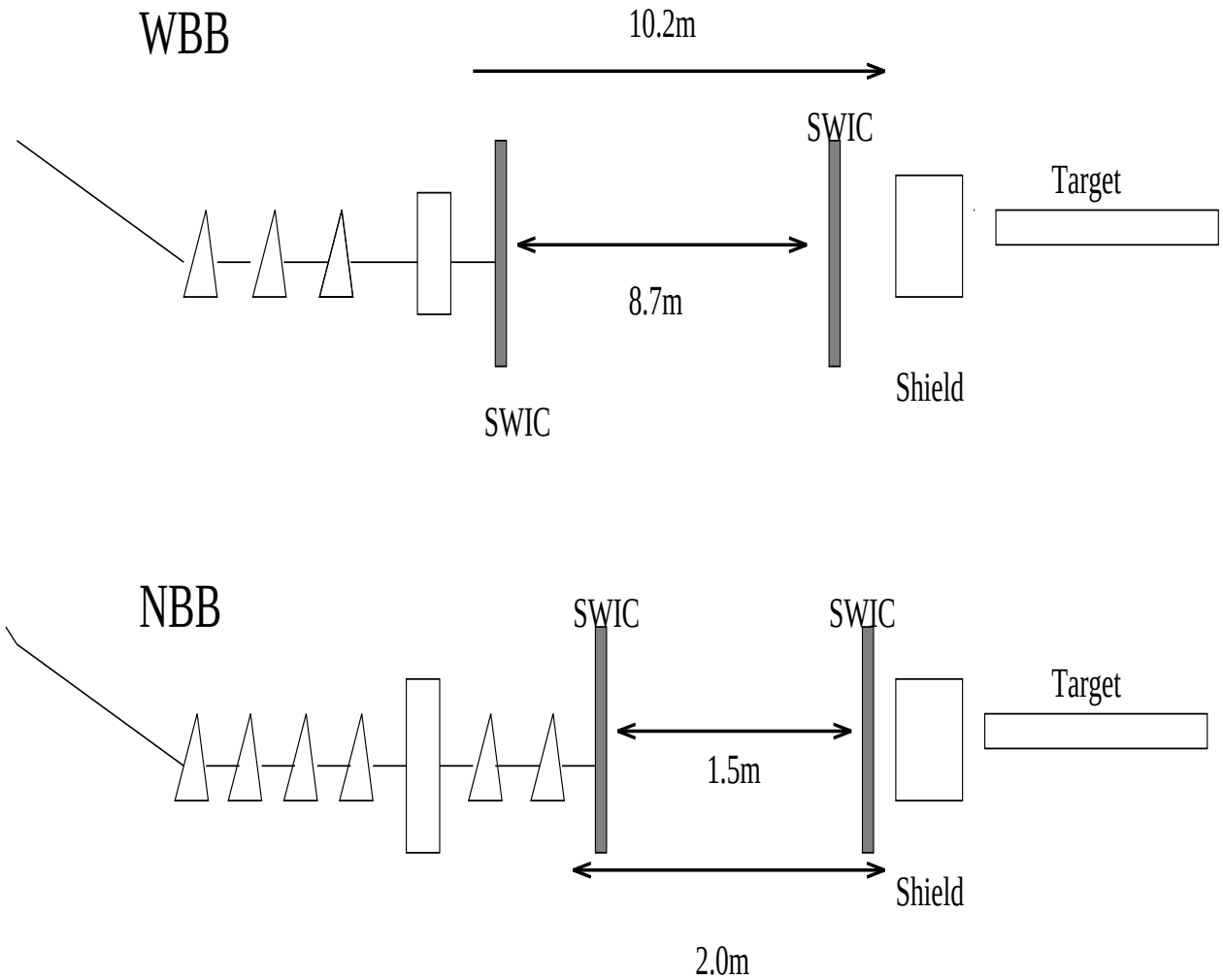

Figure 6.1: Schematic showing the layout of the proton line and SWICs for Narrow Band and Wide Band Beam Configurations.

methods of measurement gives obvious advantages in the event of a failure and also helps to cross calibrate the devices.

6.1.2 The Secondary Hadron Beam and Muon Beam

After establishing the trajectory with the primary beam, a target scan will be done to put the target "on line". Non-interacting protons (about 13% for a two-interaction segmented carbon target) multiple scatter in the target and have a radial size of about 10 cm at the end of the Target Enclosure. So as not to interfere with these protons, a split-plate ion chamber (a disk separated into 4 quadrants) with the inner 20 cm missing, will be used to monitor the secondary hadrons (see Figures 6.2, 6.3 and 6.4). Both horns are on alignment tables, and their position will be finalized by observing and correcting the asymmetries in this split-plate ion chamber.

The profile and position of the entire beam, including the tails of the primary that are outside the target diameter and the non-interacting protons, can be measured by the SWIC

at the downstream end of the Target Enclosure mentioned in the previous Section. Since the split-plate ion chamber will only give up/down and left/right asymmetries, the SWIC will serve as an additional diagnostic. Because of the high rate, a SEM at the downstream end of the Target Enclosure will be used to measure the intensity to obtain a ratio of the flux per incident proton.

Downstream of the proton dump, inside the Dump Enclosure, it will be relatively straightforward to measure the muon flux and its profile with an ion chamber. A schematic of the layout is shown in Figure 6.5 and the radial muon distribution is shown in Figure 6.6. Measuring the muon flux as a function of position will add redundancy to the centering measurements made on the hadrons. In addition it will give a measurement of the number of muons per incident proton in a much less hostile environment because there are no hadrons and the intensity is lower.

6.1.3 Target and Horn Displacement Studies

A Monte Carlo study was made to show the effects on the neutrino beam of small misalignments of the primary-target/horn-focussing system. Three separate simulations, each based on 100 million incident protons, were carried out. One was with the primary target (including the incident proton beam) centered on axis, another with it displaced laterally 2 mm, and another with it displaced 4 mm.

The trajectories of the hadrons emerging from the horns were extrapolated to the region 10 m beyond the end of the 800 m decay tunnel and their locations transverse to the beam axis plotted. Only those secondary hadrons whose decay neutrinos passed through a 2 m-diameter circle at the COSMOS location and which had energies above 2 GeV were considered. It was further required that the hadron energy be above 16 GeV. These limitations are taken to approximate the muon flux above 10 GeV behind the dump, assuming it to be 10 m long. The resulting events are then separated into four quadrants, divided parallel and perpendicular to the direction of the imposed target displacement, and are plotted against radius. The decrease of flux with radius is approximately compensated by the increase in area per unit radial interval.

It can be seen from Figures 6.7 and 6.8 that the on-axis target distributions are both up-down and left-right symmetric, while those for the 2 mm- and 4 mm- eccentric targets are clearly asymmetric with a sense opposite to that of the target displacement. Other analyses, based upon the same Monte Carlo simulations, suggest that the target-horn optical system behaves like a simple lens of a positive magnification 100X in that a lateral target displacement of 4 mm produces an opposite shift of the peak neutrino energy flux (at a distance of 1 km) by about 40 cm.

Of course, displacement of the primary target (and the proton beam) is not the only possible misalignment. A rigid displacement of the entire 2-horn system by the same amount in the opposite direction would give similar effects; but horn displacements are not likely to be so rigid or so simple. Sensitivity to more complex optical asymmetries will be obtained by segmenting each of the muon detector quadrants radially to permit higher moments to be calculated and monitored, on-line.

6.2 Monitoring of the Narrow Band Beam

For the Narrow Band Beam(NBB), the set up is different as shown in Figure 6.1. The distance between the two pre-target SWICs is only 1.5 meters. By itself this leads to a pointing accuracy of only 250 μm/1.5 m = 0.17 mrad. This line combined with the line formed by the two dipoles in the NBB and monitored at the Dump Enclosure SWIC will make the NBB pointing accuracy comparable to that of the WBB. Since all non-interacting protons are stopped in a dump inside the Target Enclosure, only the secondary hadrons will be seen in the SWICs defining the outgoing line. This makes a direct measurement of the beam profile and intensity relatively straightforward with a SWIC and a SEM at the downstream end of the Target Enclosure. In addition, use can be made of Cerenkov counters when the beam energy is well defined, to measure the π and K fractions[37]; as in the past, this effort would be the responsibility of the experimental collaborations. The muon counters downstream of the dump can be used in the same way as in the WBB.

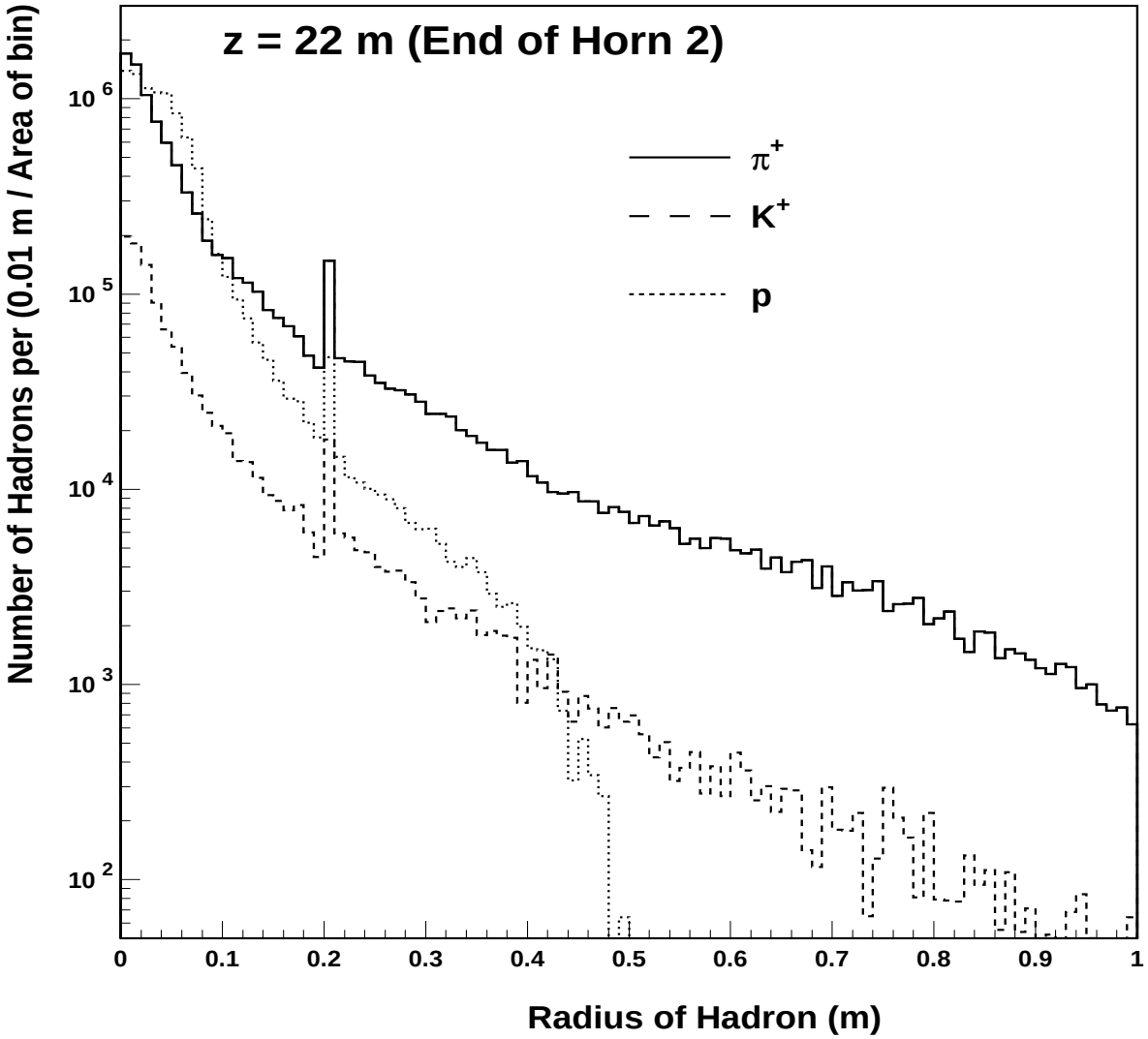

Figure 6.2: The radial distributions of the π^+s, K^+s and protons at the end of the second horn.

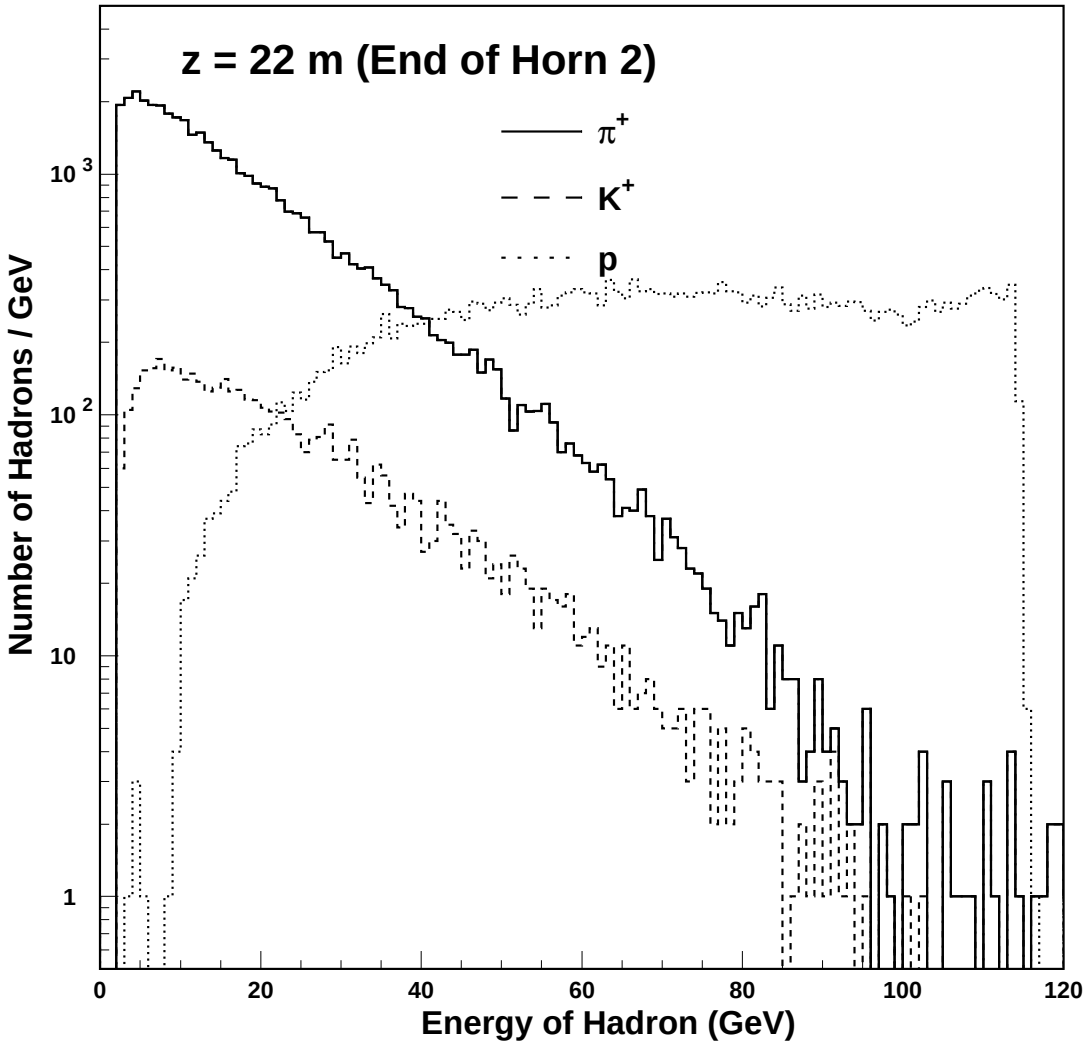

Figure 6.3: The energy distributions of the π^+s, K^+s and protons at the end of the second horn.

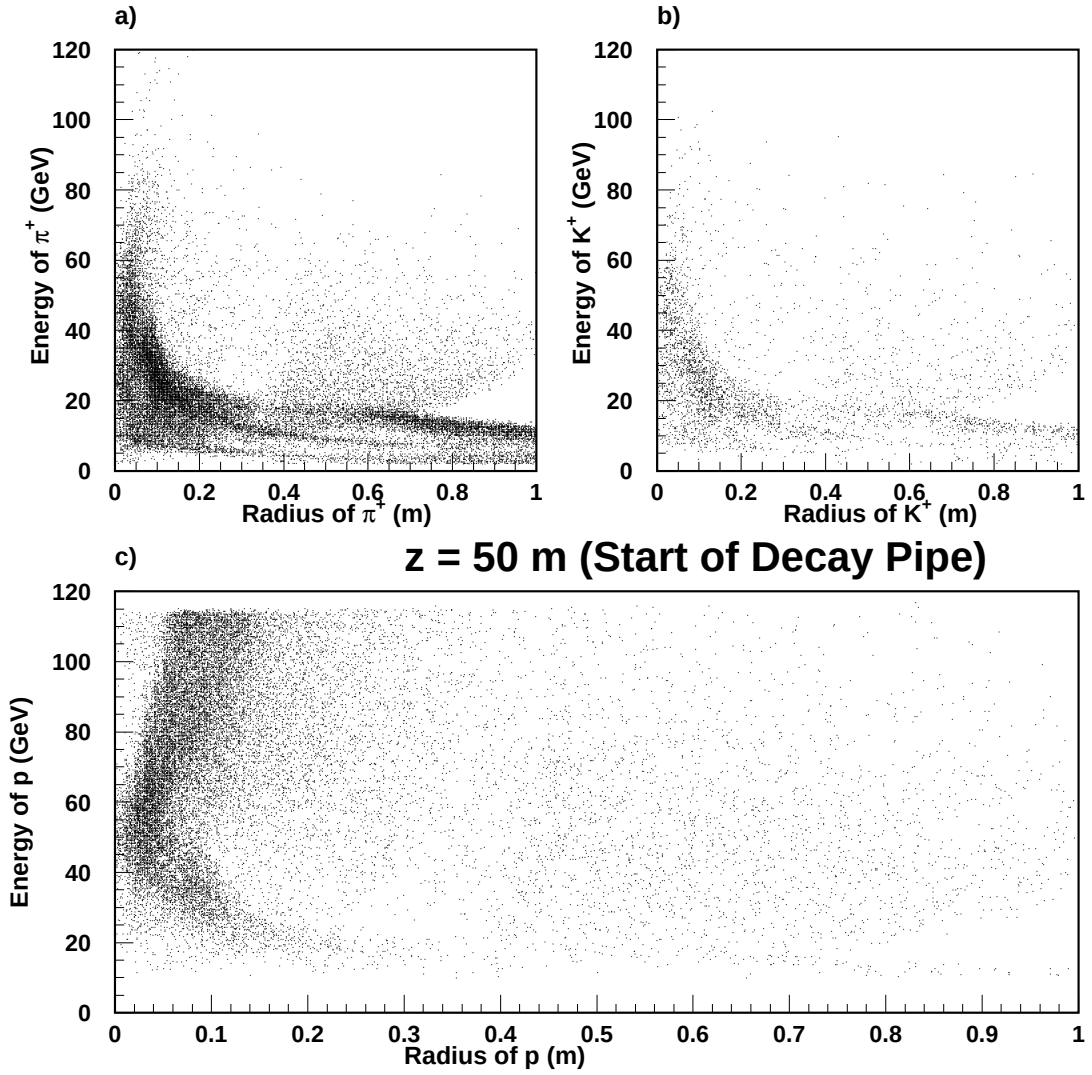

Figure 6.4: a) Energy of the π^+s vs radius at the beginning of the decay pipe, b) energy of the K^+s vs radius in the same location and c) energy vs radius of the protons in the same location.

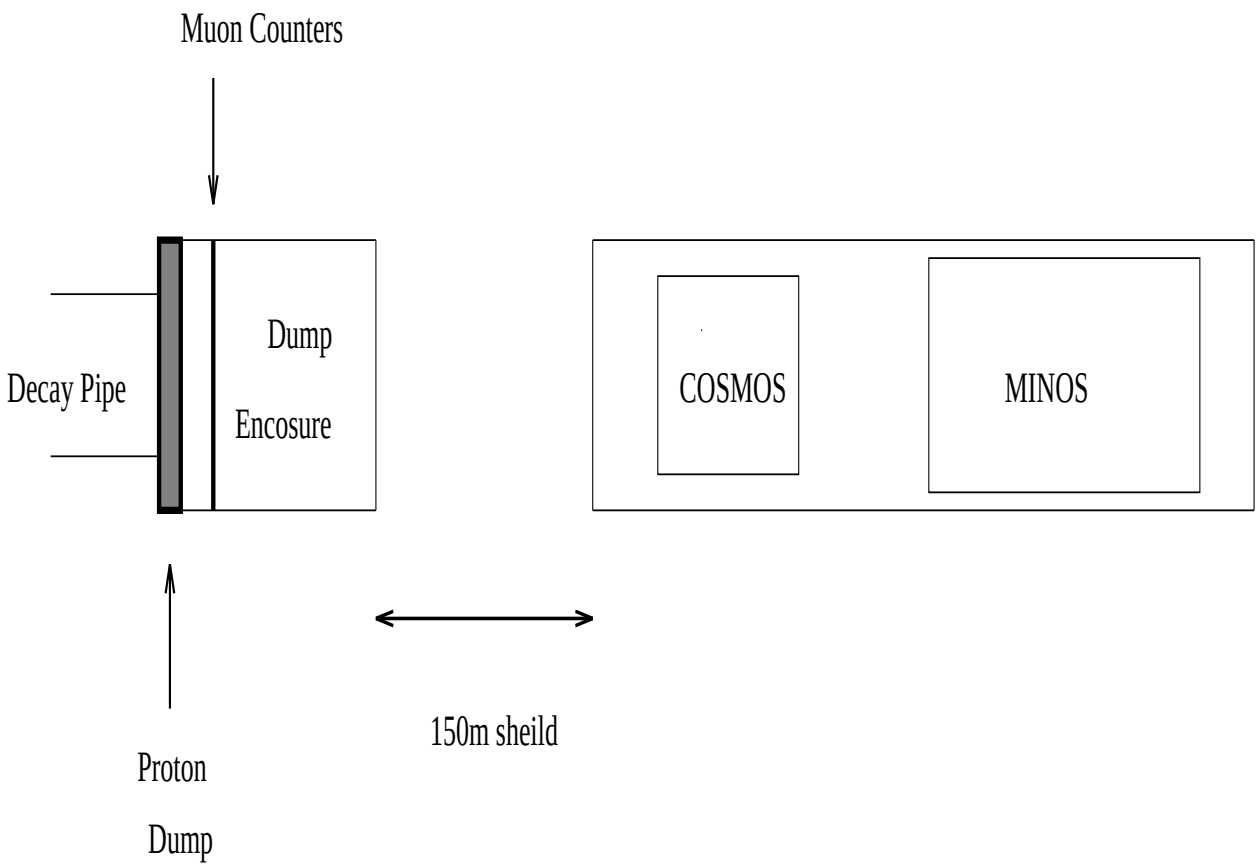

Figure 6.5: Schematic showing the layout of the dump and muon monitoring device.

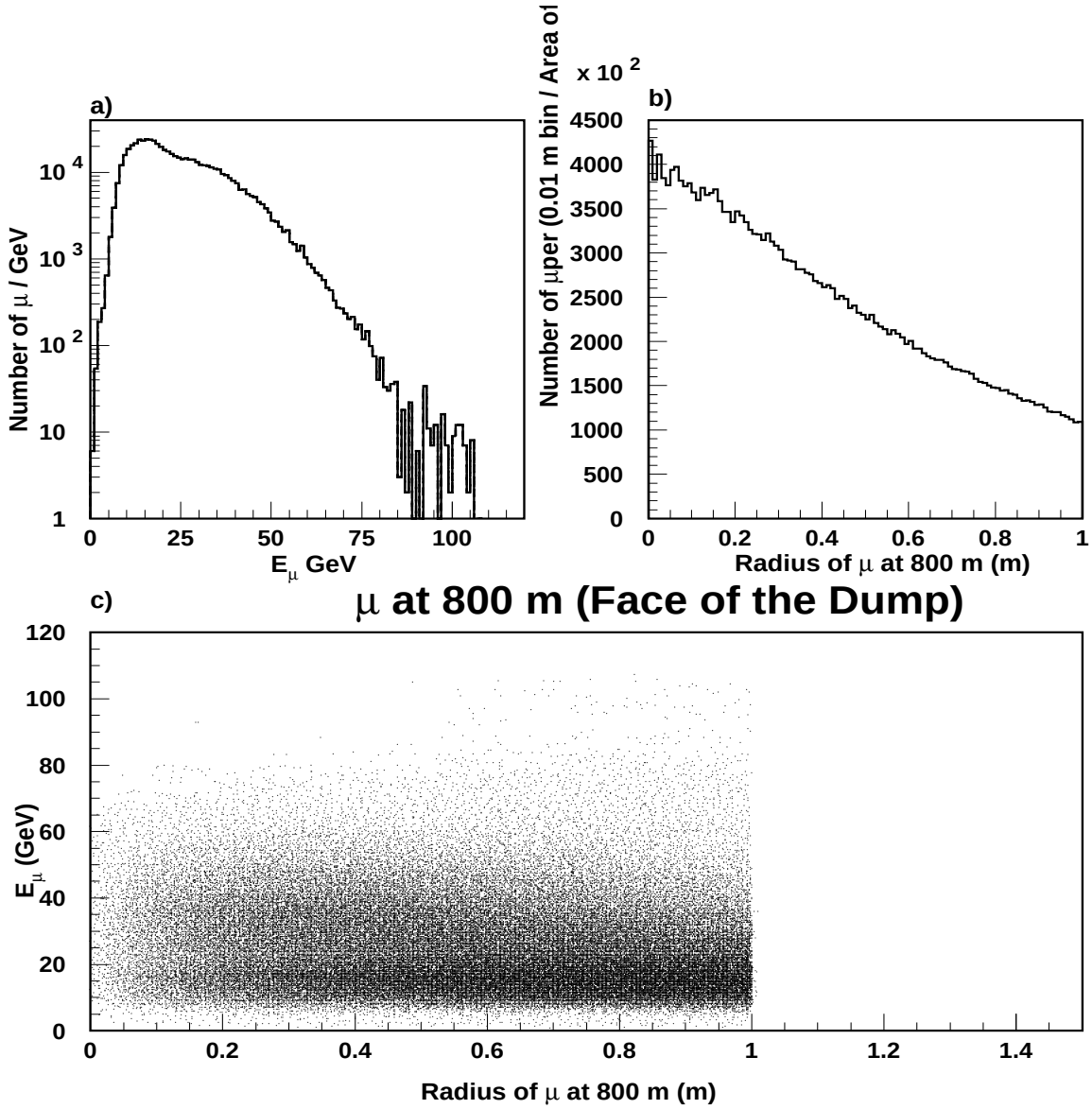

Figure 6.6: a)The energy distributions of the μs at the end of the decay pipe, b) the radial distribution of the μs and c) the energy *vs* radial position.

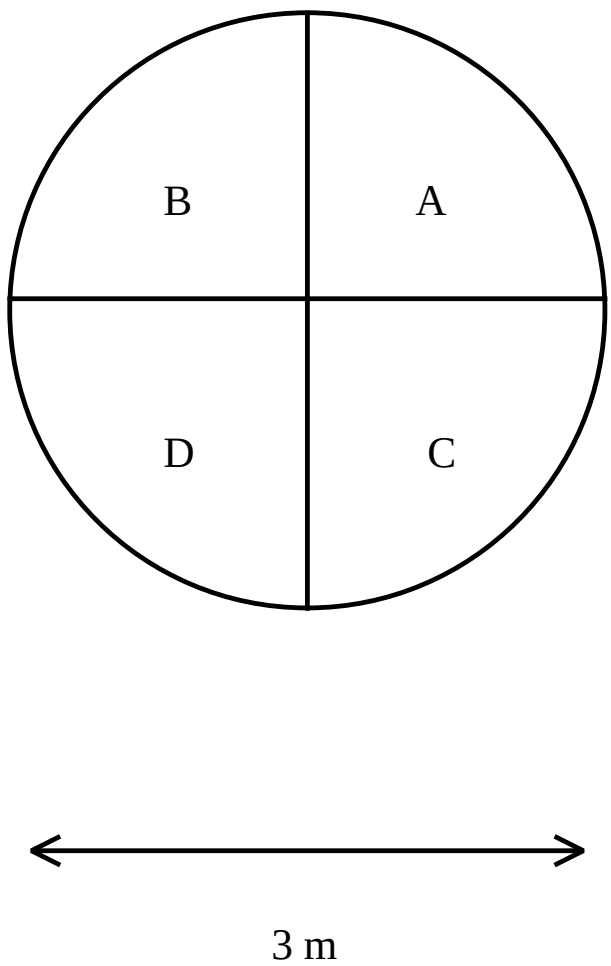

Figure 6.7: Schematic showing definitions of quadrants

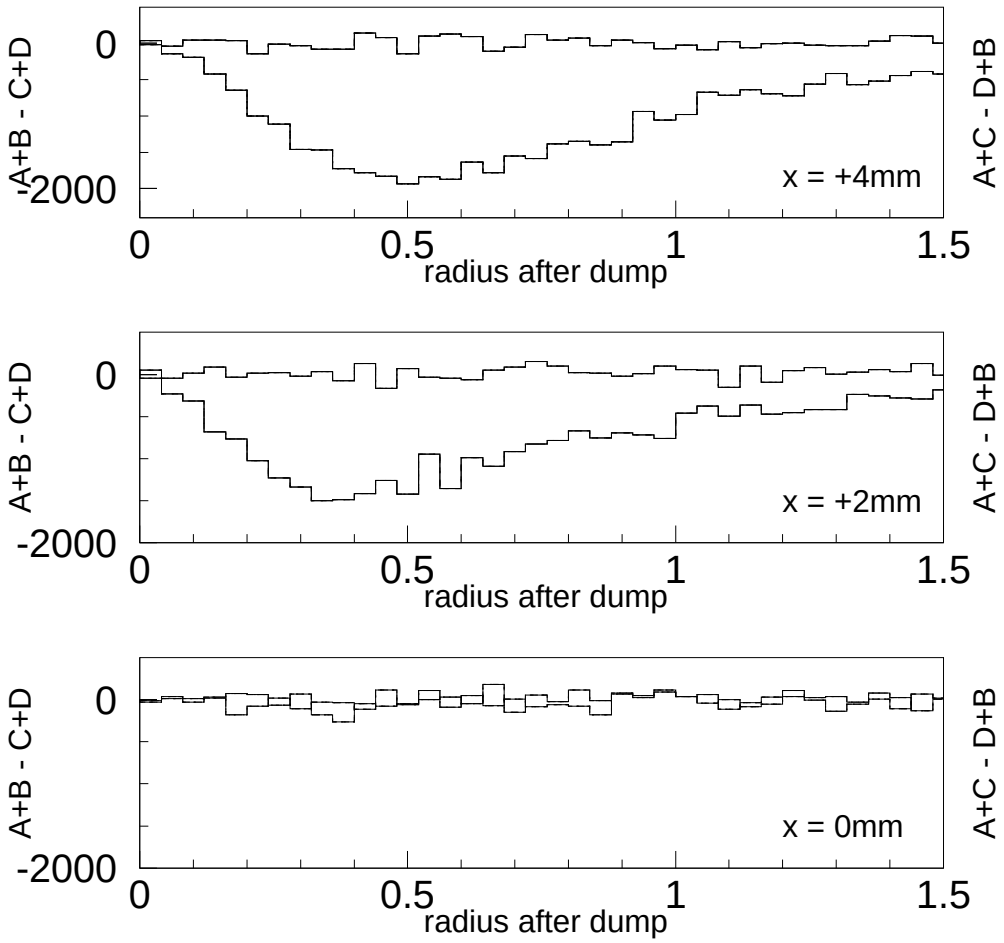

Figure 6.8: Up-down and left-right asymmetry plotted as a function of radius after the dump as a simulation of the muon flux from decayed hadrons in the decay pipe for three different horn system offsets (x) for muons from 10^8 protons on target. (A+B)-(C+D) shows the up down asymmetry (which is essentially zero) and (A+C)-(D+B) is the left-right asymmetry resulting from the shift in position in x.

Chapter 7

Radiation Safety

7.1 Introduction

Radiation safety concerns associated with the NUMI project can be divided into four categories. These are:

- shielding of prompt radiation (both neutrons and muons)
- activation of target and beam line components
- activation of the air within the enclosure
- concentrations of radioactivity produced in ground water and in surface water discharges.

Estimates of residual activity, dose rates, and necessary shielding may be obtained from the results of Monte Carlo calculations using the computer code CASIM[38] and by recognizing that simple scaling arguments apply. CASIM allows one to model arbitrary shielding geometries composed of several different materials and/or regions. The results of a CASIM calculation are the distribution of inelastic interactions (referred to as the star density) produced per incident particle within the specified geometrical limits as well as the total number of stars produced within each material or region. The CASIM results may be converted into dose rates at the surface of bulk shielding or into levels of activation using well-established conversion factors. When coupled to models describing the transport of radioactivity, the results may be used to estimate radionuclide concentrations generated in ground water or surface water discharges.

7.2 CASIM Model Geometry

A cylindrically symmetric model of the NUMI target hall and decay pipe (see Figure 7.1) was coded for use with CASIM. The target hall was modeled as a 50 meter long cylinder 5 meters in diameter and surrounded by concrete. The decay pipe region was modeled as an empty cylinder 745 meters long and 2 meters in diameter surrounded by dolomite ($CaMg(C0_3)_2$). The decay pipe ends in a 5 meter long block of steel (beam absorber), 4 meters in diameter.

A segmented carbon target was followed by the double-horn design. The inner and outer aluminum conductors as well as end flanges of the horns were explicitly included in the model. Magnetic fields for the horns were included, with the field assumed to vary outside the inner conductor of each horn as 34 kG-cm/r (cm) out to a cut-off radius of 15 cm (20 cm) for the first (second) horn. The field was assumed to be zero inside the inner conductors of each horn.

The target and each horn were surrounded by steel shielding out to a radial distance from the beam centerline of 170 cm. The target and first horn were contained within the steel shielding in a cavity 40 cm in diameter, with the upstream end of the target recessed 1 meter into the cavity. The downstream end of the steel shield was 6.5 meters past the downstream end of the horn.

The second horn was contained in a cavity 50 cm in diameter with its upstream end recessed 1 meter into its cavity. The downstream end of the steel was also 6.5 meters past the downstream end of the second horn. The inner diameter of the steel shielding downstream of the second horn was 600 cm. The region between the steel shielding surrounding the two horns contained a 1 meter thickness of concrete shielding.

In order to reduce the star density in the dolomite surrounding the decay pipe region, the effects of various configurations of steel "collimators" were studied, and the results are discussed in Section 7.3.3. Additional calculations also were done to study in more detail the total stars and the star density distribution in the target hall region ($Z < 50$ meters) to determine the residual activation of target hall shielding, the surrounding concrete and air.

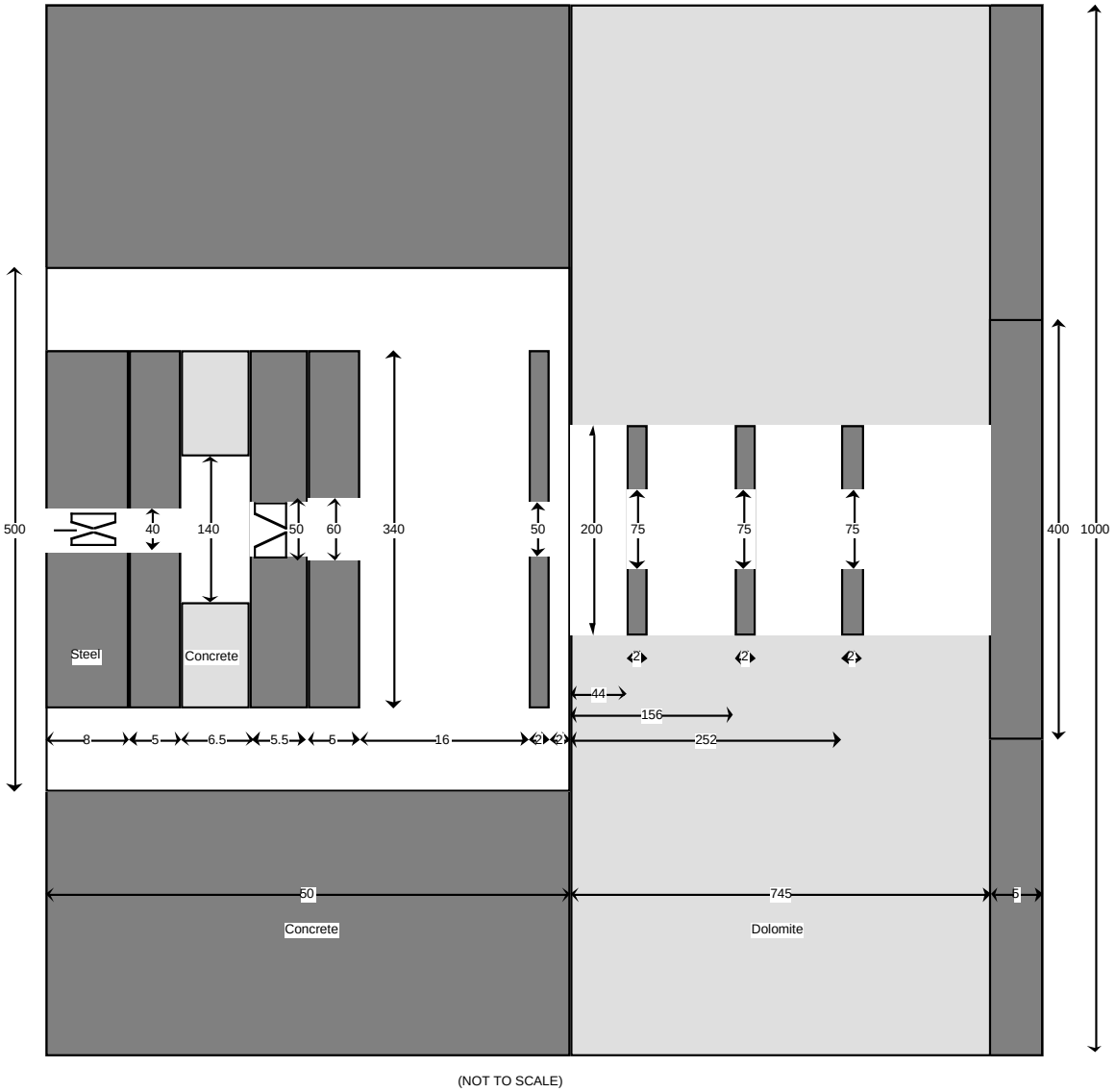

Figure 7.1: NUMI target hall and decay tunnel geometry used for CASIM calculations. Note that the radial and longitudinal scales are different. Horizontal dimensions in meters and vertical dimensions in cm.

7.3 Shielding of Prompt (Beam-on) Radiation

The NUMI primary beam transport line, target hall, decay pipe and beam absorber will be located well below the surface (greater than 7.6 meters). Therefore, beam-on neutron dose rates at the surface will be negligible, allowing unlimited occupancy of the surface above the beamline. In addition, because of the downward angle of the primary beam, muon dose rates also will be negligible and are not discussed further here. For completeness, however, the minimum amount of transverse shielding needed to satisfy the Fermilab Radiological Control Manual criteria is discussed briefly below to justify the statement that dose rates at the surface will be negligible.

7.3.1 Pre-target Enclosure

The standard beam-loss accident scenario was assumed, i.e. a one hour loss of the full machine intensity of 4×10^{13} 120 GeV protons per spill and 1800 spills per hour on a beam line magnet 1 meter from the enclosure wall. The following assumptions were made:

- the energy dependence of the star density at fixed radius varies as (Beam Energy)$^{0.8}$
- the star density decreases by a factor of 10 for each additional 83 cm of earth-equivalent shielding transverse to the beam direction
- the star-density-to-dose conversion factor is 10^{-2} mrem per star per cm^{-3}

Scaling to 120 GeV from the CASIM results of reference [39] for the same geometry but at a beam energy of 1000 GeV, gives a minimum requirement of 7.56 meters (24.8 feet) of earth-equivalent shielding to reduce the accident dose rate to 1 mrem per hour outside the shielding. This accident rate permits unlimited occupancy of the area outside the shielding.

7.3.2 Target Hall

The detailed CASIM results for the region surrounding the target hall ($Z < 50$ meters) with the internal shielding arrangement as described above, show that the maximum star density at a radius of 5 meters from the beam centerline occurs in the region between the two horns and is about 2×10^{-12} stars cm^{-3}-proton^{-1}. This corresponds to a dose rate of 1440 mrem per hour during normal running at 4×10^{13} protons per spill and 1800 spills per hour. To reduce this dose rate to the 0.25 mrem per hour dose rate for normal operating conditions that is required by the Radiological Control Manual for unlimited occupancy requires an additional attenuation of 1.74×10^{-4}. This can be provided by an additional 3.1 meters of earth-equivalent shielding. The total amount of shielding that would be required in this region is then 660 cm (21.6 feet) including the 1 meter of concrete shielding present inside the enclosure between the two horns. This requirement is easily met since the target hall will be located about 26 meters (86 feet) below the surface.

7.3.3 Decay Pipe

The maximum star density in the decay pipe region at a radius of 5 meters from the beam centerline occurs near the upstream end of the decay region and is about 2×10^{-14} stars-cm^{-3}-proton^{-1} for the case where there are no downstream collimators. This corresponds to a beam-on dose rate of 14.4 mrem per hour during normal running at 4×10^{13} protons per spill and 1800 spills per hour. To reduce this dose rate to the 0.25 mrem per hour that is required by the Radiological Control Manual for unlimited occupancy requires an additional attenuation of 1.7×10^{-2}. This can be provided by an additional 1.5 meters of earth-equivalent shielding. The total amount of required earth-equivalent shielding surrounding the decay pipe region is therefore about 5.5 meters (18 feet), assuming a 1 meter radius decay pipe.

7.3.4 Summary

The amount of hadron shielding needed to reduce the dose rate to the levels necessary for unlimited occupancy is no more than 7.6 meters (25 feet) for any region associated with the NUMI facility. Since the depths of the primary beam line, target hall, and decay pipe will all exceed this number, there will be sufficient transverse shielding.

7.4 Activation of Shielding and Components

The dose rates due to residual activation of shielding and other beam line components also can be estimated from CASIM results. The rates depend on assumptions about typical irradiation and cool-off times as well as the type of activated material. The most conservative assumption is that of infinite irradiation and zero cool-off times, which results in the highest estimated levels of activation. The method of dose rate estimation is summarized in the Fermilab Radiological Control Manual[40] and is based on the work of Barbier[41]. For infinite irradiation and zero cool-off time the dose rate, D, is given by

$$D = \frac{\Omega}{4\pi}\omega(\infty,0)\cdot S\cdot I \tag{7.1}$$

where

$\Omega/4\pi$ is the fractional solid angle subtended by the source at the measurement location

$\omega(\infty,0)$ is the material-dependent conversion factor, for infinite irradiation and zero cool-off, that converts star density at the surface of the material to dose rate (9×10^{-3} mrads/hour per star/cm^3/sec for steel)

S is the calculated star density at the surface of the material of interest

I is the beam intensity in protons per second

Typically steel target pile shielding at Fermilab has been designed so that the residual dose rate at the outer surface of the shield is no more that 100 mrads per hour. This insures that beam-off doses to workers within the enclosure are not excessive. This 100 mrads per

hour design goal requires a star density at the surface of steel shielding of less than 1.1×10^{-9} stars cm^{-3} for the NUMI beam intensity and repetition rate. This is achieved by having steel shielding around the target and horns out to a distance of 170 cm from the beam centerline. This corresponds to an actual steel shield thickness of 150 cm around the target and upstream horn region and 145 cm around the downstream horn region, due to the inner diameters of the shielding cavities that contain the target and horns.

Figure 7.2 shows the star density calculated with CASIM for the radial bin between 160 cm and 170 cm as a function of the distance along the beam line. This radial bin corresponds to the outer surface of the steel and concrete shielding in the target hall. Note that it is below the 100 mrads per hour limit except in the region between the horns where no steel and only one meter of concrete shielding was in place. However, the conversion factor, $\omega(\infty,0)$, for concrete is smaller than that for steel by about a factor of two to three, and so the maximum dose rate in this region at the surface of the concrete also should be about 100 mrads per hour. Other options such as using $CaCO_3$ (marble) which has some advantageous activation properties have been discussed in Chapter 3.

Based on the calculated star densities, worst-case dose rates from activation inside the steel shielding along the inner surfaces of the cavity containing the target and first horn could be as much as 5000 rads per hour shortly after the beam is turned off following a long run and would be expected to decrease by roughly a factor of three after a 10 day cool-off period. Dose rates on the upstream and downstream faces of the steel shielding close to the beam axis also will be high immediately after beam shut-off, ranging from 100 to 1500 rads per hour, depending on location.

It is useful to compare these CASIM estimated rates with measured residual dose rates from the anti-proton target station, which operates at about 3.0×10^{12} ppp with a beam energy of 120 GeV and a repetition rate of 2 seconds per spill. Dose rates for the lithium lens as high as 80 R per hour on contact and 10 R per hour at one foot have been measured. Dose rates on the anti-proton production target have been measured as high as 550 R per hour on contact and about 45 R per hour about one foot beneath the target. Dose rates of about 3 R per hour have been measured one foot to the side of the bottom edge of some steel shielding modules. The decay time following beam shutoff varied for these measurements, but it was typically from one to a few days, implying dose rate reductions of two to three due to decay [42].

The NUMI beam intensity will be about 13.3 times the current Main Ring intensity used for anti-proton production. Scaling the lowest reading for the antiproton target of about 3 R per hour measured one foot from the bottom of the steel shielding to the higher Main Injector intensity, correcting for decay (a factor of about 2) and for measurements made at one foot versus measurements made on contact (a factor of about 10 typically), suggests that rates on contact with the inner surface of the NuMI steel shielding immediately after beam shut off could be about 800 R per hour. Target and lithium lens dose rate measurements scaled to the Main Injector era indicate even higher rates. While target station geometry and some materials are different for the anti-proton and NUMI target stations, it is clear that contact dose rates of the order 1000 R per hour or more inside the target station shielding should be expected immediately after shutdown. Clearly, dose rates of this magnitude will require that the target and other beam line components be carefully designed to minimize personnel exposure during maintenance and replacement activities.

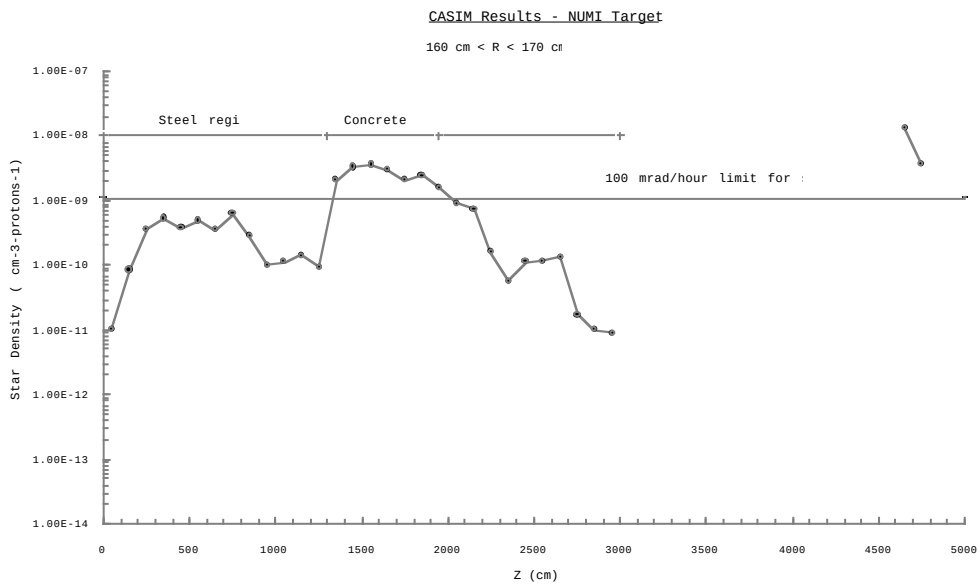

Figure 7.2: The star density for the radial bin 160 cm $< R <$ 170 cm in the target hall region ($Z <$ 50 meters). This radial bin corresponds to the outer surface of the steel and concrete shielding installed within the target hall. The horizontal line corresponds to the star density limit that results in 100 mrads per hour residual dose rate at the surface of the steel for infinite irradiation and zero cooloff times with a primary beam intensity of 4×10^{13} protons every 2 seconds.

7.5 Air Activation

To set the scale for the levels of air activation in the target hall, ^{11}C production was estimated by replacing the void spaces in the target hall CASIM geometry of Figure 7.1 with air (assumed to be 20 % O_2 and 80% N_2). The beam path length through the air was 50 meters. The production rate of ^{11}C was determined from the total number of stars produced in air per incident proton using an assumed ^{11}C production cross section of 30 mbarns. This cross section is 11% of the weighted average of the O_2 and N_2 total proton inelastic cross sections for these elements. It was also assumed that there was no ventilation of the target hall and that the beam was on for a time long compared to the ^{11}C half-life of 20 minutes so that the production rate equaled the decay rate.

The CASIM results indicate 0.137 stars per incident proton are produced in the air. If 11% of these result in the production of a ^{11}C atom then the total production rate for an incident beam of 4×10^{13} protons every 2 seconds is 3×10^{11} per second. At equilibrium, this represents an activity of 8 Curies. If this 8 Curies of activity is uniformly mixed with the entire air volume present in the modeled target hall geometry (6.26×10^{5} liters) the initial concentration would be 1.3×10^{-2} micro Curies per ml which is 43 times the value of the Derived Air Concentration (DAC) limit for inhalation of ^{11}C in the form of CO_2 (3.0×10^{-4} microCuries per ml) and 3250 times the value of the DAC limit for immersion in a semi-infinite airborne cloud containing ^{11}C (4.0×10^{-6} microCuries per ml) [43]. Waiting a total of two hours following beam shutoff would reduce the concentration to less than the inhalation DAC limit and waiting a total of about four hours after beam shutoff would reduce the ^{11}C activity to less than the immersion DAC limit, even in the absence of ventilation.

Levels of airborne radionuclide emissions from the NUMI target station can be limited by minimizing the ventilation of the area during operations and then allowing sufficient time for decay of airborne radioactivity after a beam-shutdown and prior to any personnel access. In the example indicated above, a one hour decay period followed by rapid ventilation of the target hall enclosure would result in about 1 Curie of ^{11}C released to the environment. A two hour wait prior to ventilating the area would result in the release of about 0.125 Curies.

Comparable levels of ^{15}O and ^{13}N would also be produced, but they have shorter half-lives than ^{11}C and so are ignored here. Other isotopes with somewhat longer half-lives than ^{11}C, such as ^{38}Cl and ^{39}Cl produced by spallation on atmospheric ^{40}Ar, and ^{41}Ar, produced by thermal neutron capture on ^{40}Ar, will also be present and contribute to the airborne activity. All of these isotopes have been identified in previous emissions from other target station stacks at Fermilab.

It is planned to have a substantial fraction of the air-filled target hall volume along the beam direction (30 m) filled with helium gas thereby substantially reducing the production of ^{11}C and the other isotopes. The only radionuclide that would be produced through interactions in the helium gas is tritium, which is not easily detected by the standard survey meters or stack monitors currently in use at Fermilab. However, it is possible to estimate tritium production rates in helium gas using the same approach discussed here for ^{11}C. If the helium gas is contained in a closed system, the level of tritium would increase in approximate proportion to the total number of incident protons due to tritium's long half-life ($\sim$ 12.3 years). This is different than the ^{11}C case where an equilibrium level of activity is quickly reached. CASIM calculations of tritium production in helium gas are currently

underway.

7.6 Ground Water and Surface Water Activation

The presence of induced radioactivity in the soil and/or rock surrounding the NUMI target hall and decay pipe regions potentially can lead to the presence of radioactivity in underlying ground water or in water discharged from beam line enclosures to the surface through a process known as leaching. Leaching can occur when water passes through rock or soil containing radioactivity. Several studies and measurements of the leachable radioactivity produced in the soil adjacent to Fermilab target stations show that the two principal isotopes of concern are ^{3}H and ^{22}Na [44]. There are regulatory limits on the allowable concentrations of ^{3}H and ^{22}Na in community drinking water supplies (ground water) and in surface water discharges. These limits must not be exceeded.

CASIM results of the maximum star density per incident proton produced in unprotected soil or rock can be combined with a specific model of the leachability and transport of ^{3}H and ^{22}Na to arrive at an annual limit on the number of protons that can be targeted for a specific target station shielding design. This model of leachability and transport is referred to as the "Concentration Model" and is discussed more fully in references [45] and [46]. The model is summarized below.

In the Concentration Model the initial concentration C_i, for radionuclide i, in a region of soil or rock is given by

$$C_i = \frac{N_p \cdot S_{max} \cdot 0.019 \cdot K_i \cdot L_i}{1.17 \times 10^6 \cdot \rho \cdot w_i} \tag{7.2}$$

where

N_p is the number of incident protons per year

S_{max} is the maximum star density per incident proton in the unprotected soil or rock obtained from a CASIM calculation.

K_i is the radionuclide production probability per star (0.075 atoms/star for ^{3}H, 0.02 atoms /star for ^{22}Na in soil; 0.03 atoms / star for ^{3}H, 0.02 atoms / star for ^{22}Na in dolomite)

L_i is the leachability factor for the radionuclide (0.9 for ^{3}H and 0.135 for ^{22}Na in soil; 0.9 for ^{3}H and 0.009 for ^{22}Na in dolomite))

ρ is the material density (2.25 gm/cm^3 for moist soil, 2.8 gm/cm^3 for dolomite)

w_i is the weight of water divided by the weight of soil that corresponds to 90% leaching (0.27 for ^{3}H and 0.52 for ^{22}Na) in soil.

The final concentration in ground water, C_f, is related to the initial concentration by

$$C_f = C_i \cdot R_{till} \cdot R_{mix} \cdot R_{dolomite} \tag{7.3}$$

where R_{till} is a reduction factor in the model that takes account of the migration of radionuclides downward through the soil (glacial till) to the aquifer and allows for radioactive decay *en route*. The reduction factors are given by

$$R_{till}(^3H) = 1.0e^{[-0.3d(meters)]} \tag{7.4}$$

$$R_{till}(^{22}Na) = 1.0e^{[-0.92d(meters)]} \tag{7.5}$$

where d is the distance between the aquifer and a point 1.84 meters below the point of maximum star density. The other reduction factors, R_{mix} and $R_{dolomite}$ usually are assumed equal to one.

The regulatory limit on the final concentrations that must be met can be expressed as

$$\frac{C_f(^3H)}{C_{reg}(^3H)} + \frac{C_f(^{22}Na)}{C_{reg}(^{22}Na)} \leq 1 \tag{7.6}$$

where $C_{reg}(^AZ)$ is the regulatory limit on the concentration for isotope ^AZ.

The model as described above applies to the case of a standard near-surface Fermilab target station located in the glacial till several meters above the ground water aquifer. The NUMI design locates the target station and decay region in dolomite bedrock below the elevation of the shallowest aquifer. Thus R_{till} is not present and there is assumed to be no reduction due to migration so that C_f will equal C_i . The C_i values are calculated using the dolomite values for K_i, L_i and ρ [47]

The pressure gradients that drive the flow of water through the dolomite are assumed to be such that water will generally flow into rather than away from the NUMI target station and decay pipe regions. It is assumed that this water will be collected in sump pits and subsequently discharged to the surface. Thus, it is the regulatory limits for the concentrations in surface water discharges rather than the ground water limits that drive the NUMI target station and decay region shield design. This is an advantage since the surface water discharge limits on the concentrations are 100 times greater than the ground water limits for ^{3}H (20 vs. 2000 pCi per ml) and 50 times greater for ^{22}Na (0.2 vs. 10 pCi per ml).

The modeled geometry shown in Figure 7.1 was used in CASIM to determine the maximum star density produced in the innermost layer of rock (100 cm $< R <$ 110 cm) surrounding the decay pipe region. The results are shown in Figure 7.3 as a function of the distance along the beam line. The solid circles correspond to a design where there is no additional shielding of the rock surrounding the decay pipe. Note that the calculated star density is slowly varying with Z and is roughly a factor of ten higher than the limiting star density of 5×10^{-9} stars per cm^3 per incident proton. This limiting value, shown as the horizontal line in Figure 7.3 was calculated using Equations 7.2, 7.3 and 7.6 assuming that water containing leached radioactivity flows into the decay pipe tunnel, is collected and discharged to the surface and that the number of protons on target per year is 3.7×10^{20}.

It is necessary to reduce the star density in the rock to the limiting value shown in the figure to ensure that surface discharge limits are not exceeded. One approach being studied is to provide additional shielding in the form of steel "collimators" at selected locations within the decay pipe. These function as absorbers to reduce star production in the surrounding rock. The solid squares in Figure 7.3 illustrate the combined effect of collimators located at

Z= 48 meters, 96 meters, 208 meters and 304 meters. The collimator at Z=48 meters (near the end of the target hall) had a 50 cm diameter aperture. The others had 75 cm apertures. Note that a 2 meter long collimator with a 75 cm aperture at Z= 304 meters reduces the maximum star density along the remainder of the decay pipe to less than the required limit. The more upstream collimators also can reduce the star density but over more limited ranges of Z. Studies are underway to optimize the number, locations, length and aperture sizes of such collimators to reduce the star density below the allowed value over the entire decay pipe length while maintaining an adequate neutrino flux.

Figure 7.4 shows a comparison between the surface water discharge limit (horizontal line) and the star density in the target hall region only ($Z < 50$ meters) for the innermost radial bin surrounding the target hall (250 cm $< R <$ 260 cm). Star densities for this radial bin also meet the surface water discharge limit.

7.7 Summary

Radiological concerns associated with the NUMI project are no different in kind than those that have been handled successfully at Fermilab in the past. Prompt radiation dose rates will be mitigated by the depth of the beam below ground. The levels of residual activation of some target station components and shielding will be high and will require that careful attention be paid to their detailed design to keep personnel exposures as low as reasonably achievable. Remote handling capability and use of shielding materials in selected locations that have reduced activation potential and more rapid decay properties (such as marble), the use of temporary shielding and lead coffins for storage and transport of components are all methods that could be used to mitigate personnel exposures. Environmental radiation concerns to the air and ground water can also be adequately mitigated through proper shielding design and operational procedures.

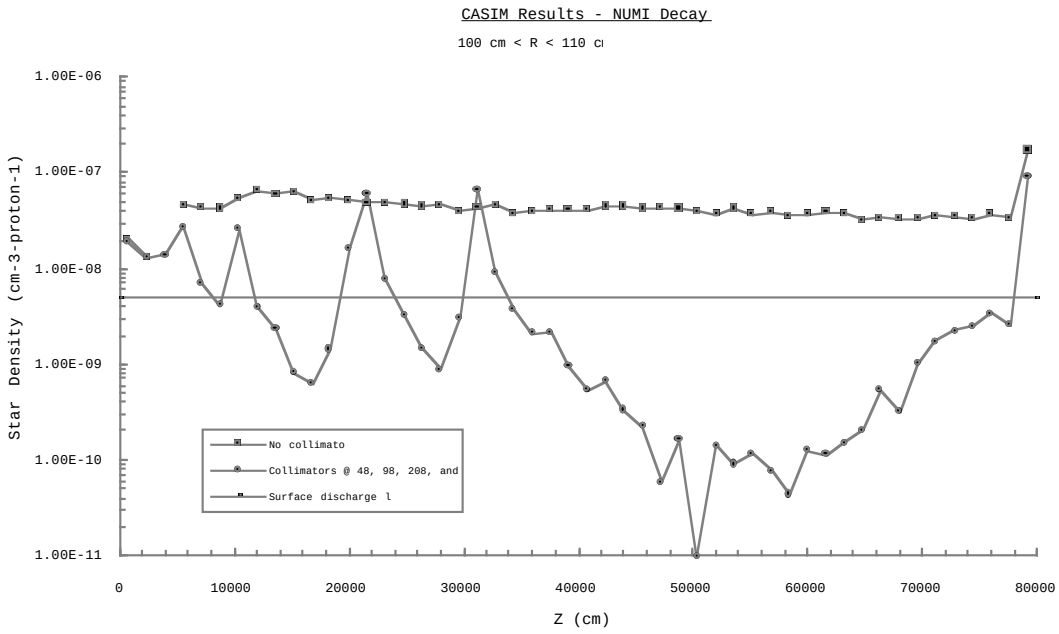

Figure 7.3: The star density for the radial bin 100 cm< R <110 cm as a function of the distance along the beam line. The solid circles are the CASIM results with no forward "collimator" shielding installed. The solid squares are the CASIM results with 2 meter long steel collimators located at 48, 96, 208 and 304 meters. The horizontal line indicates the limiting star density for surface water discharge assuming 3.7×10^{20} targeted protons per year. Other lines are drawn to guide the eye.

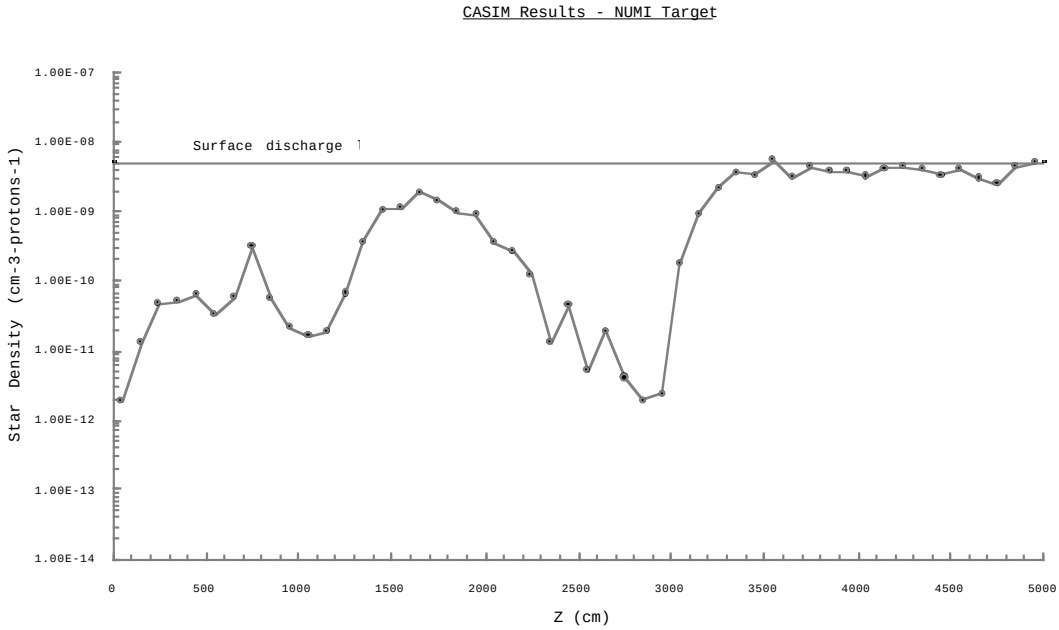

Figure 7.4: The star density for the radial bin 250 cm $< R <$ 260 cm as a function of the distance along the beam line in the target hall region ($Z <$ 50 meters). The solid squares are the CASIM results. The horizontal line indicates the limiting star density for surface water discharge assuming 3.7×10^{20} targeted protons per year. The other lines are drawn to guide the eye

Chapter 8

Optimization of the Beam Lines

In the preceding chapters we have presented a detailed description of the design for a neutrino beam facility that will provide both the wide-band and narrow-band neutrino beams necessary to successfully complete the physics programs of the COSMOS and MINOS experiments. This design is based on technology and systems that either exist now at Fermilab or have been built in the past. It is, therefore, a fairly conservative design that has been frozen for the June, 1995 HEPAP sub-panel presentation and which must undergo further refinement and enhancement. In this chapter we will describe how we currently envision this optimization program.

There are two specific types of "optimization" that should be considered. The first type involves providing the described neutrino beam facility with equal physics potential for reduced cost in either initial dollars and/or projected down-time. The second involves improving the physics potential of the beam facility for equal or slightly increased cost, ie more physics yield per dollar or hour of potential down-time. The ultimate optimization is, of course, to combine the two cases and provide increased physics potential for reduced costs.

The various elements of the neutrino beam are, naturally, interrelated. We address each section in turn and discuss how the optimization of one can affect the others:

8.1 Pre-target proton transport and the target

The optics of this section were designed to bring the protons on target at the correct angle and with the optimum size and divergence. The impinging angle simply reflects the bends within the secondary beamline after the target (none in the case of the wide-band beam) and is easily adjustable. The size, on the other hand, is directly tied to the thermal properties of the target. In the original design the beam, and therefore the target, had been enlarged (r = 3 mm target) so as to be able to accept the high rate of 120 GeV protons necessary for the experiment. This resulted in a loss of neutrino intensity due to reabsorption of secondaries in the target. Recent advances in cooling techniques and available materials have allowed us to reduce the size of the target to r = 2 mm with a consequent increase in flux. We are currently studying various combinations of target material, geometry and cooling techniques which might allow us to reduce the size of the target and beam even further. This study will

also include an analysis of system effects, such as proton beam divergence, on intensity and efficiency.

8.2 Secondary Collection and Focusing

The horns of the wide-band beam have undergone a certain degree of optimization in that many shapes, lengths and spacing have been tried, as described in chapter 3, and none have been found superior to the nominal horn described in this Status Report. Designs for shorter horns are still being investigated since they have the advantage of making the handling easier and also enable the actual size of the shielding pile to be reduced. Furthermore, all designs maintained a certain minimum horn radius which was based on the strength of the materials used. We are currently investigating whether new materials can be developed which allow smaller radii and thus deeper penetration into the secondary beam profile and more efficient focusing.

The optics of the narrow-band beam have been based on a 1-cm radius Li-lens since this has been employed successfully by the anti-proton source group at Fermilab for many years. To further optimize the NBB, one could design special dipole and quadrupole magnets with increased apertures which are a real restriction on collected phase space. One can also work toward lowering the stress on the titanium cooling jacket which is done by lowering the preload on the lithium at fill time as described in section 3.4.2. If this is done, the lens can handle the larger thermal stresses which come from running at higher currents. The lens can then be moved closer to the target and collect more secondaries.

Finally, although plasma lenses have not yet met with much success, a plasma lens would offer the immediate advantage of negligible absorption compared to the loss of around 10 per-cent with the Li-lens.

One avenue of potential improvement that would affect both the wide-band and narrow-band beam options is the development of an optical system which combines a Li-lens with a horn. This system might well provide equal or better intensity compared to the double Horn system. Currently, the main problem with this idea is the physical placement of the two components so as to minimize absorption of the secondaries. Were this possible, the time required to switch from one beamline configuration to the other would be greatly reduced.

8.3 Replacement of Damaged Components

This is an area where an initial investment during the design stage can save many frustrating hours of down- time. In the present design we have incorporated a straight-forward replacement of a failed horn with as much remote handling as possible. This replacement scheme still involves an amount of lost beam-time which we would like to reduce. We are currently investigating the possibility of having a sliding table, with a spare horn ready for installation, within the target pile, without an unacceptable increase in the size of the shielding.

8.4 Decay Region

The present length of the decay space (800 m) was chosen as a compromise between the needs of E803, E875, the position of the experimental hall and the overall cost of the beam line. However, for the short baseline experiment, it has been shown [48] that by varying the decay space, it would be possible to determine Δm^2 and $\sin^2(2\theta)$ separately, rather than just a 2-dimensional contour if a signal were observed. For control of groundwater contamination we are presently considering the necessity of installing a series of 75 cm gap collimators at selected sites within the 2 m diameter beam pipe. If we make these variable gap collimators that can be adjusted to also stop most of the parent mesons we would have a method for varying the L parameter in the oscillation probability expression.

8.5 Monitoring

The procedures of monitoring the neutrino beam presented in this document are methods that have been used by other wide-band and narrow-band neutrino beams in the past. They have known limitations in trying to fit the parent meson momentum distribution which is what is needed to uniquely predict the neutrino spectrum in a given detector. The best way to obtain this knowledge would be to actually measure the four-vectors of mesons leaving the target and coming out of the optics (second horn of the WBB). However, this is a major experiment in itself with many complications. If the spatial and momenta spectra of the secondaries would allow it, a good approximation of this spectra should be obtainable using Cerenkov techniques such as were employed in earlier narrow-band beam runs at both Fermilab and CERN.

Appendix A

Neutrino Oscillations Facility: Design Basis for Civil Construction - G. Koizumi, Fermilab and T. Toohig, Boston College

A.1 Scope

The major defining elements of the neutrino oscillations (NuMI) facility are the 120 GeV proton beam from the Main Injector (MI) to the neutrino production target, the neutrino beam forming system including the 800-meter decay region, and the on-site detectors. The civil construction for the facility includes the housing and support elements for transporting the primary proton beam, for the targeting and beam forming systems, for the decay pipe, for the beam dump(s) and for the on-site detectors. It also includes the monumentation and survey referencing with the required accuracy the on-site facility to the major detector at Soudan.

The detector hall will house the detector for the short baseline experiment, COSMOS, and the near detector for the long baseline proposal, MINOS. After the two major detectors are assembled, the laydown space on the beam axis for assembling these detectors will be used for exposing modules from the Soudan 2 detector. The pre-target and target regions, which include the active elements of the primary proton beam and the neutrino beam system, will house the wide band beam forming system (WBB), the horn system, which is included in the project. After exposure to the wide band system the targeting may be converted to a narrow band system (NBB), which can be accommodated in the space.

A.2 Design Considerations

The design must take cognizance of the requirements for installation, operation and maintenance of all of the technical systems, while minimizing the facility costs and conforming to applicable safety, environmental and radiation guidelines. Very few design solutions are unique, so the conceptual design adopted here reflects a number of decisions relative to sit-

ing, operations, handling of radioactive elements, and environmental protection. The major decisions impacting the design are described below:

The experimental area must lie south of Pine Street, which is the primary access to the Laboratory, in order to avoid complications and expense associated with road access, utilities, and environmental and aesthetic requirements. This constraint, coupled with the specified 800-meter decay length, places the target south of the new 8 GeV line, adjacent to the Anti-proton source building.

The production target must be a minimum of 20 feet below the top of rock stratum to avoid interference with the overlying aquifer at the base of the glacial till. This constraint added to the constraint above results in a dip angle of approximately -104 mr for the proton beam leaving the Main Injector extraction stub enclosure.

Access to the underground is excluded when the primary proton beam is enabled. This provision simplifies the configuration of the underground enclosure, reduces the volume of excavation and eliminates the need for massive shielding doors. It also simplifies the security system and personnel safety procedures.

Radiation shielding in the target region will utilize local, close-packed shielding around radiation sources, including the target, beam forming elements and any beam dumps. This local containment of the radiation reduces the levels at the walls of the enclosures below the limits specified for protection of the ground water regime. Putting the radiation burden on the internal shielding, rather than the surrounding bedrock simplifies the civil construction initially and minimizes concerns for decommissioning later. A remotely-operated bridge crane will be required to extract radioactive elements from the shielding piles.

Calculations using the approved Fermilab ground water model indicate that, with appropriate shielding, any impact on the groundwater of radiation along the neutrino decay pipe will be below regulatory limits. In addition, the decay tunnel is designed to provide positive control of the ground water along the approximately 750 meters of the decay tunnel by introducing a negative, inward gradient in the hydrogeologic pressure in the surrounding host rock.

Primary access to all enclosures will be by elevator with emergency backup power. Exit shafts will be equipped with OSHA-compliant ladderways and space and provision for emergency evacuation hoists. The depth of the enclosures, ranging from 100 to 285 feet, is unprecedented at Fermilab. In view of the depths, equivalently 10 to 28 stories, stairways are not themselves a practicable means of evacuation, and interfere with space for an evacuation hoist.

Access to the underground enclosures will be from the west side. This choice is driven by the proximity of the antiproton service road.

A.3 The Pre-Target System

The pre-target system consists of a drift space of approximately 300 feet from the Main Injector and a length of approximately 180 feet containing the proton beam steering and focusing magnets extending from the end of the drift space to the target. The proton beam leaves the Main Injector enclosure with a bearing of 152.190 degrees with respect to Fermilab site East, and a dip angle of approximately -104 mrad for the wide band beam system, or

-102 mrad for the narrow band beam system. The vertical separation of the two beam trajectories at the end of the drift space is approximately 8 inches. Both trajectories can be contained in a single 12-18 inch beam pipe. A 24-inch diameter micro-tunneled carrier pipe is provided in the conceptual design to accommodate this beam pipe. In the pre-target enclosure this dip angle is reduced to approximately -58 mr, the angle to the detector at Soudan. The enclosure has a nominal cross-section of 8-ft. x 8-ft with the beam 30 inches from the east wall; the slope of the floor follows the dip angle of the beam with the beam entering 3-ft. below the roof of the enclosure and leaving 3-ft. above the floor for the wide band trajectory. An emergency exit shaft is located within 50 feet from the south end of the enclosure and is connected to the enclosure by a shielding labyrinth.

A.4 The Target Hall

The target hall extends approximately 170 feet from the pre-target enclosure to the entrance to the 6-ft. diameter decay pipe. The length of the hall accommodates the range of designs for projected wide-band and narrow-band systems. The floor of the enclosure is sloped to parallel the beam centerline. The width of the hall, 17'-6", is determined by the width of the close-packed shielding around the target and horns plus the width of the aisle for operations and maintenance. The height of the hall, 19'-6" to the top of the crane bridge, is fixed by the height of the shielding pile around the target and horns, plus clearance for materials handling in maintenance operations. An equipment drop, 15' x 30' alongside the target hall is connected to the hall within 50 ft. of the north end of the enclosure by a 7-ft. wide corridor. The drop and corridor are level, in contrast to the hall itself. The length of the corridor and the separation of the drop from the hall are determined by radiation shielding and constructibility considerations. Normal access to the hall is by elevator accessing both the hall and equipment drop.

A.5 The Decay Tunnel and Pipe

The decay pipe is a nominal 2-meter diameter evacuated steel pipe, approximately 2500 ft. (750 m) in length with a wall thickness of approximately 3/4", sufficient to sustain the vacuum pressure. The centerline of the pipe is along the centerline of the beam. The pipe is flanged at either end and closed with a vacuum window having a smaller flanged thin window to accommodate the beam and a vacuum pumpout port. The tunnel housing the decay pipe is a nominal 8-ft. diameter tunnel centered on the beam axis with clearance between the wall of the tunnel and the pipe for insertion of monitoring equipment. The tunnel is unlined to present a negative gradient for any movement of water and grouted to maximize the water inflow which can then be collected in the dump enclosure.

A.6 The Dump Enclosure

The dump enclosure, which terminates the decay region, contains a massive steel beam dump with a water-cooled aluminum core. A beam monitor, requiring occasional access, is

positioned between the vacuum window of the decay pipe and the dump. The floor of the dump is level to allow extraction and insertion of the dump for servicing of the monitor. The dump is mounted on recessed tank rollers which roll on track plates embedded in the floor. The sides and top of the dump are stepped to contain radiation by eliminating cracks. The 245 foot deep shaft is offset from the enclosure to attenuate radiation penetrating the dump. Normal access is by a rack-and-pinion, construction-type elevator. Provision is made for an emergency hoist with an emergency ladder as backup. Entrance into the enclosure will be rare, since the dump is basically an inert device. Space is provided for a sump to contain the water from the decay region, for a heat exchanger for the dump cooling, if required, and for a holding pump for the decay pipe vacuum.

A.7 The Detector Hall

Two versions of the detector hall are included in the conceptual design; the first, 40-ft. x 100-ft., makes multiple use of space by scheduling the detector construction as a unit, the second, 60-ft. x 140 ft., provides space for independent and simultaneous construction of all three detectors to be operated in the hall. The distances involved in the second case require a fire-corridor from the exits to within 50 feet of the ends of the hall, effectively reducing the useful width of the hall by some amount. For both designs a single large, 15-ft x 30-ft., equipment shaft is offset from the hall, in addition to personnel and exit shafts. A 30-ton crane is provided in both designs for constructing and servicing the experiments.

Appendix B

NuMI Technical Costs (preliminary)

The following Table lists the technical costs for the entire beamline from the extraction at MI-60 through the Dump Enclosure. Many of the estimates have relied on recent experience, modified for NuMI requirements. We have drawn most heavily from the work of E-815, KTeV, and the Main Injector. The assumptions in the cost estimate are the following:

1. All standard dipoles and quadrupoles will be available from existing Fermilab beamlines, but Lambersons, C-Magnets and verniers will not.

2. All standard power supplies will be available from existing Fermilab beamlines.

3. Water pumps, some piping, and a RAW system from a decommissioned beamline in the Proton Area, service building PS-4 will be available.

4. Removal of the magnets, power supplies and the PS-4 water system from their existing locations and refurbishing costs are included in item "1.1.3.7 Reclamation of Existing Equipment".

5. All standard SWICs and Loss Monitors will be available from existing Fermilab beamlines.

6. T & M costs are listed individually in the costs. However, no cost has been included for Fermilab organizational units providing technician manpower, nor for physicist/manager salaries. Not included are magnet installation in the Main Injector enclosure only, power supply checkout, installation of vacuum hardware, commissioning of the water system, software for controls, instrumentation & interlock installation and checkout, horn/lithium lens tests, and alignment (survey).

7. Included in the monitoring equipment are split plate ion chambers and three large area SWICs along with their electronics. Additional SWICs or Cerenkov counters may be needed pending further studies.

8. Contingency and EDIA are not included. The largest contingency item at this time is the horn power supply system (100%). Both a transformer solution and a non-transformer solution are being pursued. Including the horn power supply, we have estimated the overall contingency of the technical costs to be 28%.

WBS 1.1 Technical Cost Estimate	Number	Unit	Unit Cost(K$)	Cost(K$)	Sub-Total(K$)	Total(K$)
1.1.1 Beam Transfer From MI-60						1565.7
1.1.1.1 Magnets					450	
1.1.1.1.1 Dipoles	11	Each	0	0		
1.1.1.1.2 Quads	7	Each	0	0		
1.1.1.1.3 Lambertsons	3	Each	113	339		
1.1.1.1.4 C-Magnet	1	Each	51	51		
1.1.1.1.5 Trims	4	Each	2	8		
1.1.1.1.6 Stands	26	Each	2	52		
1.1.1.2 Extraction					289	
1.1.1.2.1 Septa	3	Each	80	240		
1.1.1.2.2 Septa Power Supply	1	Each	20	20		
1.1.1.2.3 Cables	2	Each	10	20		
1.1.1.2.4 Stands	3	Each	2	6		
1.1.1.2.5 Cable Installation	2000	Feet	0.0015	3		
1.1.1.3 Power Supples					568	
1.1.1.3.1 Dipoles	3	Each	0	0		
1.1.1.3.2 Quads	5	Each	0	0		
1.1.1.3.3 Lambertsons	1	Each	150	150		
1.1.1.3.4 C-Magnet	1	Each	150	150		
1.1.1.3.5 Trims	4	Each	3	12		
1.1.1.3.6 Circuit Breakers/Panels	14	Each	2	28		
1.1.1.3.7 Cable Trays	800	Feet	0.03	24		
1.1.1.3.8 Cable Tray Installation	800	Feet	0.05	40		
1.1.1.3.9 Cables	30000	Feet	0.003	90		
1.1.1.3.10 Cable Installation	30000	Feet	0.0015	45		
1.1.1.3.11 Cable End Terminations	100	Each	0.05	5		
1.1.1.3.12 PS Installation(10)	40	Crew Hr	0.6	24		
1.1.1.4 Water System					123.5	
1.1.1.4.1 Heat Exchanger	1	Each	19	19		
1.1.1.4.2 LCW Pipes	1700	Feet	0.015	25.5		
1.1.1.4.3 Pipe Installation	85	Crew Hr	0.6	51		
1.1.1.4.4 LCW Pumps	1	Each	28	28		
1.1.1.5 Vacuum System					52.2	
1.1.1.5.1 Beampipe & Bellows	100	Feet	0.2	20		
1.1.1.5.2 Pumps	7	Each	3	21		
1.1.1.5.3 Valves	2	Each	5	10		
1.1.1.5.4 Gauges/Cables	6	Each	0.2	1.2		
1.1.1.6 Controls					41	
1.1.1.6.1 Racks	2	Each	1	2		
1.1.1.6.2 Crates	2	Each	4	8		
1.1.1.6.3 Computer Link	1	Each	1	1		
1.1.1.6.4 FIRUS & CATV	1	Each	10	10		
1.1.1.6.5 CAMAC Cards	20		1	20		
1.1.1.7 Instrumentation					42	
1.1.1.7.1 Beam Position Monitors	4	Each	1.5	6		
1.1.1.7.2 Loss Monitors	6	Each	0	0		
1.1.1.7.3 SWICs	2	Each	0	0		
1.1.1.7.4 Electronics	12	Each	1	12		
1.1.1.7.5 Cables	12000	Feet	0.002	24		

	Number	Unit	Unit Cost(K$)	Cost(K$)	Sub-Total(K$)	Total(K$)
1.1.2 Beampipe to Target Enclosure						64
1.1.2.3 Roughing Pump	1	Each	35		35	
1.1.2.4 Diffusion Pump	1	Each	25		25	
1.1.2.5 End Flanges & Windows	2	Each	2		4	
1.1.3 Primary Beam						742.4
1.1.3.1 Magnets					121.2	
1.1.3.1.1 Dipoles	8	Each	0	0		
1.1.3.1.2 Quads	3	Each	0	0		
1.1.3.1.3 Trims	2	Each	2	4		
1.1.3.1.4 Stands	13	Each	2	26		
1.1.3.1.5 Installation	52	Crew Hr	0.6	31.2		
1.1.3.1.6 Alignment Sight Pipes	2	Each	30	60		
1.1.3.2 Power Supples					133.4	
1.1.3.2.1 Dipoles	2	Each	0	0		
1.1.3.2.2 Quads	3	Each	0	0		
1.1.3.2.3 Trims	2	Each	3	6		
1.1.3.2.4 Circuit Breakers/Panels	7	Each	2	14		
1.1.3.2.5 Cable Trays	1200	Feet	0.007	8.4		
1.1.3.2.6 Cable Tray Installation	1200	Feet	0.05	60		
1.1.3.2.7 Cables	7000	Feet	0.003	21		
1.1.3.2.8 Cable Installation	7000	Feet	0.0015	10.5		
1.1.3.2.9 Cable End Terminations	30	Each	0.05	1.5		
1.1.3.2.10 PS Controllers	7	Each	0	0		
1.1.3.2.11 PS Installation(5)	20	Crew Hr	0.6	12		
1.1.3.3 Water System					108.6	
1.1.3.3.1 Heat Exchanger	1	Each	19	19		
1.1.3.3.2 LCW Pipes	1200	Feet	0.015	18		
1.1.3.3.3 Fittings	1	Lot	6	6		
1.1.3.3.4 Valves(from PS4)	40	Each	0	0		
1.1.3.3.5 Pipe Installation	60	Crew Hr	0.6	36		
1.1.3.3.6 RAW System	1	Each	16	16		
1.1.3.3.7 RAW Installation	16	Crew Hr	0.6	9.6		
1.1.3.3.8 ICW parts	1	Lot	4	4		
1.1.3.3.9 LCW Pumps(PS4)	3	Each	0	0		
1.1.3.4 Vacuum System					91.2	
1.1.3.4.1 Beampipe & Bellows	100	Feet	0.2	20		
1.1.3.4.2 Roughing Pump	1	Each	35	35		
1.1.3.4.3 Diffusion Pump	1	Each	25	25		
1.1.3.4.4 Valves	2	Each	5	10		
1.1.3.4.5 Gauges/Cables	6	Each	0.2	1.2		
1.1.3.5 Controls					106	
1.1.3.5.1 Racks	2	Each	1	2		
1.1.3.5.2 Crates	2	Each	4	8		
1.1.3.5.3 Computer Link	1	Each	1	1		
1.1.3.5.4 FIRUS & CATV	1	Each	10	10		
1.1.3.5.5 Safety Interlocks						
16 conductor cable	3000	Feet	0.0015	4.5		
15 pair conductor cable	1500	Feet	0.0015	2.25		
12 pair conductor cable	1500	Feet	0.0015	2.25		
1.1.3.5.6 Interlock Electronics	1	Lot	9	9		
1.1.3.5.7 Electricians	20	Crew Hr	0.6	12		
1.1.3.5.8 Local Control System						
Computing Platform	1	Each	10	10		
Hardware	1	Each	27	27		
Fiber Cable	1500	Feet	0.004	6		
Fiber Cable Installation	20	Crew Hr	0.6	12		

	Number	Unit	Unit Cost(K$)	Cost(K$)	Sub-Total(K$)	Total(K$)
1.1.3.6 Instrumentation					35.6	
1.1.3.6.1 Beam Position Monitors	4	Each	1.5	6		
1.1.3.6.2 Loss Monitors	4	Each	0	0		
1.1.3.6.3 SWICs	2	Each	0	0		
1.1.3.6.4 Large Area SWIC	1	Each	5	5		
1.1.3.6.5 Split Plate Ion Chamber	1	Each	3	3		
1.1.3.6.6 Electronics	12	Each	1	12		
1.1.3.6.7 Cables	4800	Feet	0.002	9.6		
1.1.3.7 Reclamation of Existing Equipment					146.4	
1.1.3.7.1 Magnets(36)	144	Crew Hr	0.6	86.4		
1.1.3.7.2 Power Supplies(15)	60	Crew Hr	0.6	36		
1.1.3.7.3 PS-4 Water System	40	Crew Hr	0.6	24		
1.1.4 Horn Beam						1491
1.1.4.1 Target	1	Each	10		10	
1.1.4.2 Steel Shielding	100	Ton	0.7		70	
1.1.4.3 Limestone Shielding	18	Blocks	2		36	
1.1.4.4 Horn 1	1	Each	200		200	
1.1.4.5 Steel Sheielding	300	Ton	0.7		210	
1.1.4.6 Limestone Shielding	54	Blocks	2		108	
1.1.4.7 Horn 2	1	Each	200		200	
1.1.4.8 Steel Sheielding	200	Ton	0.7		140	
1.1.4.9 Limestone Shielding	36	Blocks	2		72	
1.1.4.10 Installation	120	Crew Hr	0.6		72	
1.1.4.11 Horn Power Supply System					285	
1.1.4.11.1 Power Supply	2	Each		0		
1.1.4.11.2 Capacitor Bank	1	Each	120	120		
1.1.4.11.3 Cap Bank(Structural)	1	Each	40	40		
1.1.4.11.4 SCR Switches & Trnsdtrs	8	Each	5	40		
1.1.4.11.5 Firing Circuits & Controls	1	Each	10	10		
1.1.4.11.6 Dischg Restr & Safety	1	Each	15	15		
1.1.4.11.7 Installation	100	Crew Hr	0.6	60		
1.1.4.12 PC Data Logger/Controller	1	Each	10	10	10	
1.1.4.13 Helium System	150	Feet	0.2	30	30	
1.1.4.14 Limestone Shielding(between Horns)	24	Blocks	2	48	48	
1.1.5 Dichromatic Beam						1144
1.1.5.1 Target	1	Each	10		10	
1.1.5.2 Lithium Lens	1	Each	42		42	
1.1.5.3 Transformer	1	Each	57		57	
1.1.5.4 Lithium Lens Power Supply	1	Each	270		270	
1.1.4.5 Dipoles	2	Each	70		140	
1.1.4.6 Quadrupoles	5	Each	44		220	
1.1.4.7 Magnet Power Supplies	7	Each	40		280	
1.1.4.8 Primary Proton Dump	1	Each	125		125	
1.1.7 Dump Enclosure						455.5
1.1.7.1 Primary Proton Dump					165	
1.1.7.1.1 Steel	100	Ton	0.7	70		
1.1.7.1.2 Copper	0.8	Ton	10	8		
1.1.7.1.3 Machining	100	Hr	0.04	4		
1.1.7.1.4 Underground Assembly	40	Crew Hr	0.6	24		
1.1.7.1.5 Installation	24	Crew Hr	0.6	14.4		
1.1.7.2 Water System						
1.1.7.2.1 Heat Exchanger	1	Each	19	19		
1.1.7.2.2 RAW Water System	1	Each	16	16		
1.1.7.2.3 Install RAW	16	Crew Hr	0.6	9.6		

	Number	Unit	Unit Cost(K$)	Cost(K$)	Sub-Total(K$)	Total(K$)
1.1.7.3 Vacuum(At Target & Dump Enclosure)					156.8	
1.1.7.3.1 Roughing Pump	2	Each	35	70		
1.1.7.3.2 Diffusion Pump	2	Each	25	50		
1.1.7.3.3 Valves Between Pumps(35")	2	Each	12	24		
1.1.7.3.4 End Flanges & Windows	2	Each	3	6		
1.1.7.3.5 Safety Doors	2	Each	3	6		
1.1.7.3 6 Guages/Cables	4	Each	0.2	0.8		
1.1.7.4 Controls					96.1	
1.1.7.4.1 Racks	1	Each	1	1		
1.1.7.4.2 Crates	1	Each	4	4		
1.1.7.4.3 Computer Link	1	Each	1	1		
1.1.7.4.4 FIRUS & CATV	1	Each	10	10		
1.1.7.4.5 Safety Interlocks						
16 conductor cable	3000	Feet	0.0015	4.5		
15 pair conductor cable	3000	Feet	0.0015	4.5		
12 pair conductor cable	1000	Feet	0.0015	1.5		
1.1.7.4.6 Interlock Electronics	1	Lot	9	9		
1.1.7.4.7 Electricians	16	Crew Hr	0.6	9.6		
1.1.7.4.8 Local Control System						
Hardware	1	Each	27	27		
Fiber Cable	3000	Feet	0.004	12		
Fiber Cable Installation	20	Crew Hr	0.6	12		
1.1.7.5 Instrumentation					37.6	
1.1.7.5.1 Beam Position Monitors	0	Each	1.5	0		
1.1.7.5.2 Loss Monitors	0	Each	0	0		
1.1.7.5.3 SWICs	0	Each	0	0		
1.1.7.5.4 Large Area SWIC	2	Each	5	10		
1.1.7.5.5 Split Plate Ion Chamber	2	Each	3	6		
1.1.7.5.6 Electronics	12	Each	1	12		
1.1.7.5.7 Cables	4800	Feet	0.002	9.6		
					GRAND TOTAL	5462.6

Appendix C

Reply to HEPAP Subpanel Questions

In this appendix we include answers to the questions posed by the HEPAP subpanel which involve characteristics and/or performance of the NuMI beams.

C.1 Question #1 (a): Near Hall Location

What would be the improvement in systematics by moving the near detector hall back or reducing the decay pipe length by of order 100 meters? What would be the cost implications? How will this affect the sensitivity to $\nu_\tau \to \tau$ production for COSMOS?

The currently planned NuMI beam geometry has an 800 m long decay pipe and a shield length d of 170 m between the dump and the MINOS detector (the "800/170" scenario). The near- and far-detector neutrino energy spectra would become more similar if the shield length were increased. Thus we expect that any systematic uncertainty resulting from the difference in these spectra would be reduced by such a change. Figure C.1 shows the location of the NuMI beamline on the Fermilab site, and indicates the constraints imposed by the two branches of Pine Street and the site boundary.

A priori, d could be increased by about 100 m in two ways: (a) shortening the decay pipe by 100 m and leaving the near detector hall at the current location ("700/270"), or (b) moving the near detector hall downstream by 100 m ("800/270"). Implementation of the first geometry is straightforward but the second is more complicated. We elaborate below on these two possibilities.

The first solution would decrease the neutrino flux at the MINOS far detector by about 9%. For COSMOS[2, 49], sensitivity in $\sin^2(2\theta)$ would decrease at large values of Δm^2 by about 10%. There would be a small (about 5%) compensatory increase in sensitivity at low values of Δm^2 (i.e., $< 20\ eV^2$). The cost saving from this change (quoted, as are all subsequent cost figures, without multiplicative factors for EDIA, contingency and indirect costs) would be about \$0.75 M.

The second solution is more complicated. Moving the near detector downstream by 100 m would put the near-hall experimental building right on the south branch of Pine Street. For environmental reasons, we cannot locate the near hall between the two branches of Pine Street. Thus the nearest possible downstream location is just north of Pine Street, about 350 m from the current location. This solution ("800/520") would cause a substantial loss

of sensitivity for COSMOS. Their calculation of an "800/350" configuration shows a 35-40% loss of sensitivity in $\sin^2(2\theta)$ at large Δm^2 relative to their baseline ("800/160"). There is a small gain in COSMOS sensitivity below 20 eV^2. Figure C.2 [50] shows the 90% CL limit curves for COSMOS for several different decay-pipe lengths and shield lengths.

In light of these constraints, we have also considered a variant of the second ("800/520") solution, which incorporates separate near halls for COSMOS and MINOS. COSMOS would stay at the current location and the MINOS near detector would move 350 m downstream. The total excavated volume of the two halls and the total area of the two experimental buildings would stay roughly the same as in the current configuration. About half of the additional cost would be for the shaft to the MINOS near hall, which would go to a greater depth. Assuming the same cross-sectional area of the shaft as in current near-hall design, we estimate a total additional cost of about \$5.3M (without multipliers). We might realize some cost reduction by decreasing the shaft size to the MINOS near hall, since MINOS requirements for moving large apparatus components underground are less demanding than for COSMOS. Alternatively, if both MINOS and COSMOS were to be located in a single hall north of Pine Street, the estimated cost increment is only \$1.5M. As described above, this would compromise the COSMOS sensitivity at large Δm^2.

As expected, the near-far detector spectrum differences decrease as d increases, as shown in Figures C.3 and C.4. We have calculated the effect of this change on the T = CC/total oscillation test. In Figure C.5 we show the variation of T_{near}/T_{far} as a function of the shield length d for several different values of the parameter E_{cut}. E_{cut} is defined as the minimum number of charged particle gap crossings required for an event to be accepted. A value $E_{cut} = 4$ corresponds to a deposited energy of about 1 GeV. If we take the T_{near}/T_{far} ratio as a measure of the potential systematic error in the T test due to near-far spectrum differences, on average a small improvement is seen as d increases. The T test, however, is rather insensitive to energy spectrum variation because of a fortuitous cancellation in the NC/CC event ratio. As the fraction of low energy neutrinos increases, more CC events are misidentified as NC. However, more NC events are lost because of the minimum energy cut (i.e. number of hits). Thus the ratio NC/CC (which is closely related to T) does not change very rapidly.

In a two year run with a full detector, the statistical error on T will be about 0.002. Based on Figure C.5, we take 0.001 as a rough estimate of systematic error in T and conclude that the T test alone does not argue for increasing the value of d. However, other tests, e.g., disappearance and CC energy shape, are more sensitive to the near-far energy spectrum differences. Thus the question of modifying the shield length deserves more detailed investigation.

If we were to adopt the "800/520" solution, we would consider the possibility of placing an aluminum-plate beam monitor calorimeter, backed by a magnetized iron muon spectrometer, in the COSMOS experimental hall. This would provide an additional measurement of the neutrino flux and would extend our oscillation sensitivity to high values of Δm^2. However, we have not yet studied these possible benefits quantitatively.

Independent of whether we adopt one of the alternative beam geometries described above, the Fermilab site offers the flexibility of adding a second, intermediate distance, near detector in the future. The Laboratory has not yet had the opportunity to investigate this option carefully, but believes that it may be feasible. The distance from the currently planned

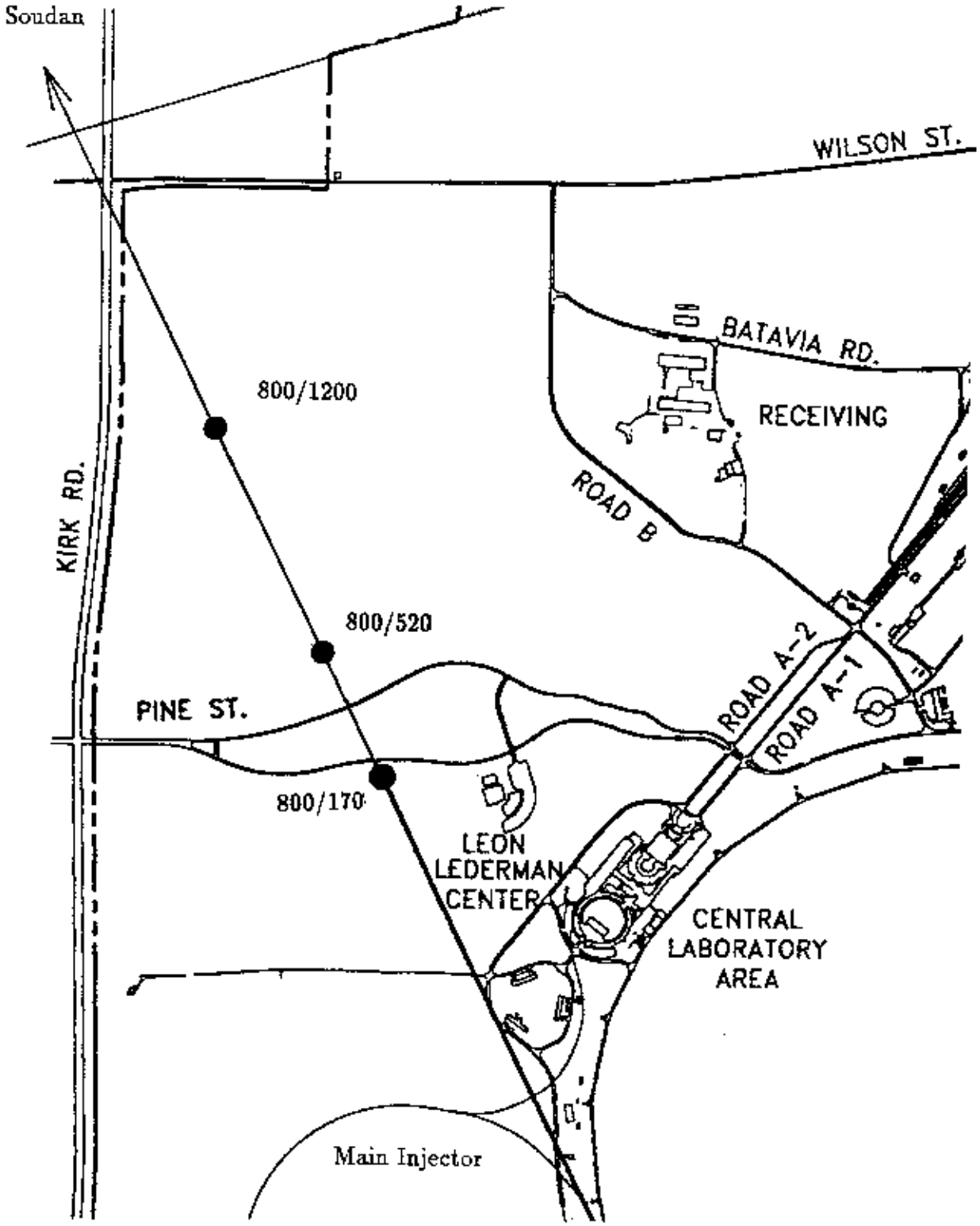

Figure C.1: Map of the Fermilab site, showing the location of the NuMI beamline and the constraints imposed by the two branches of Pine Street and by the site boundary.

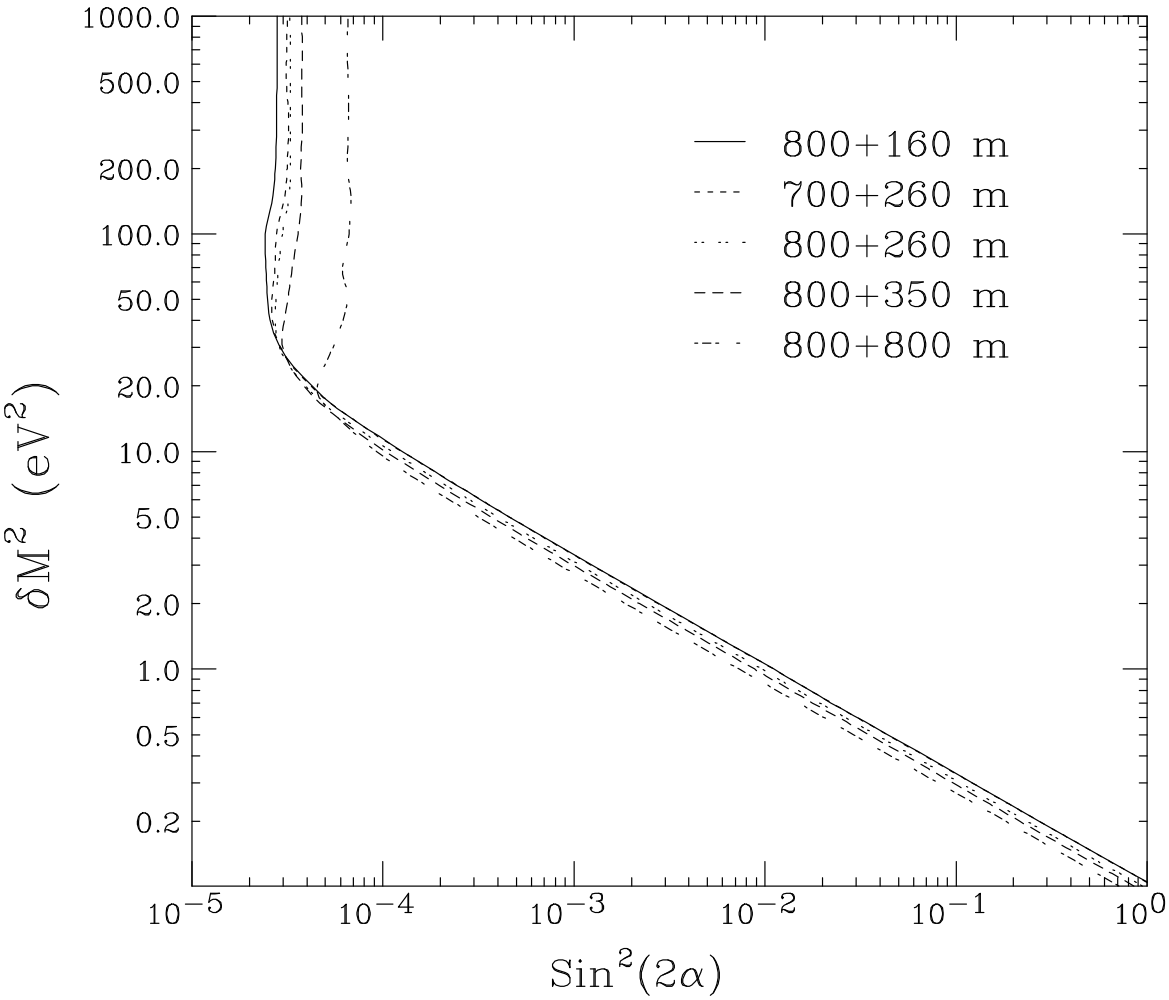

Figure C.2: Expected 90% confidence level limit curves for $\nu_\mu \rightarrow \nu_\tau$ oscillations in the COSMOS experiment for various decay pipe lengths L and shield lengths d (labelled as "$L + d$ m").

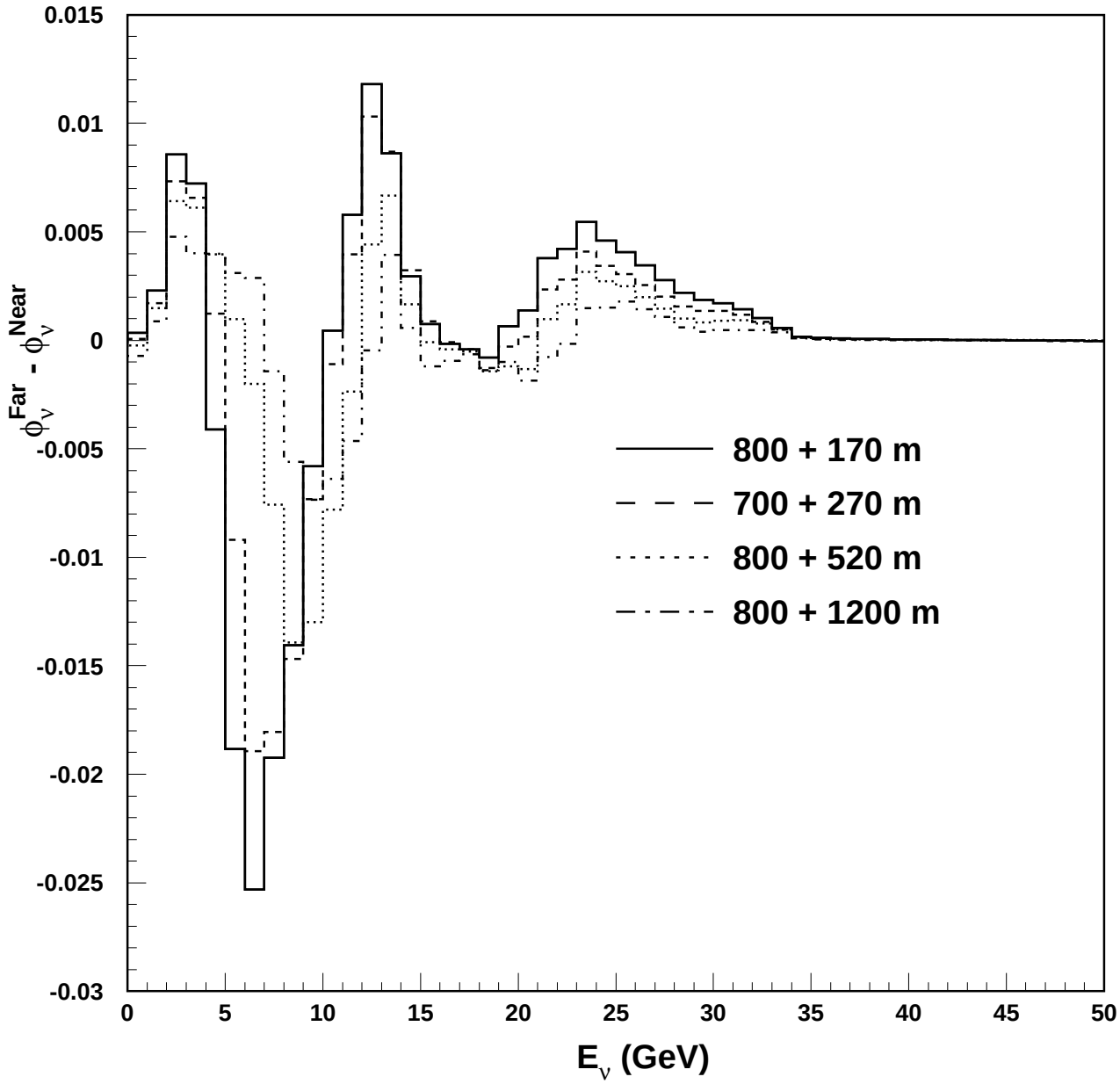

Figure C.3: Normalized far - near differences between the neutrino flux energy spectra for various decay-pipe lengths L and shield lengths d (labelled as "$L + d$ m").

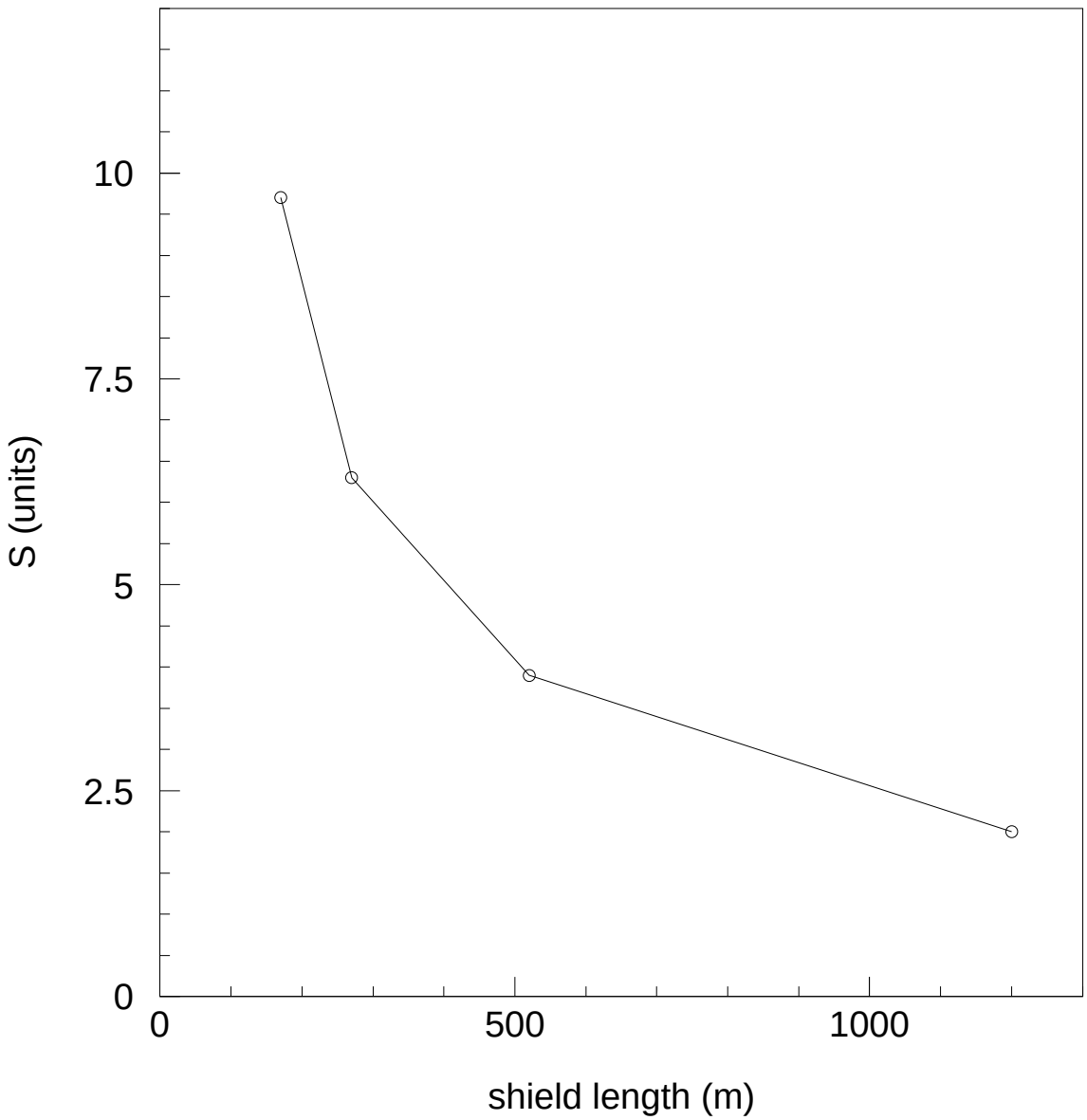

Figure C.4: Dependence of the parameter S on the shield length d. S is a figure of merit which characterizes the beam spectrum difference between the near and far detectors. S is defined on page 10 of the "MINOS Answers" document as the maximum difference between the normalized integral neutrino spectra at the near and far detectors.

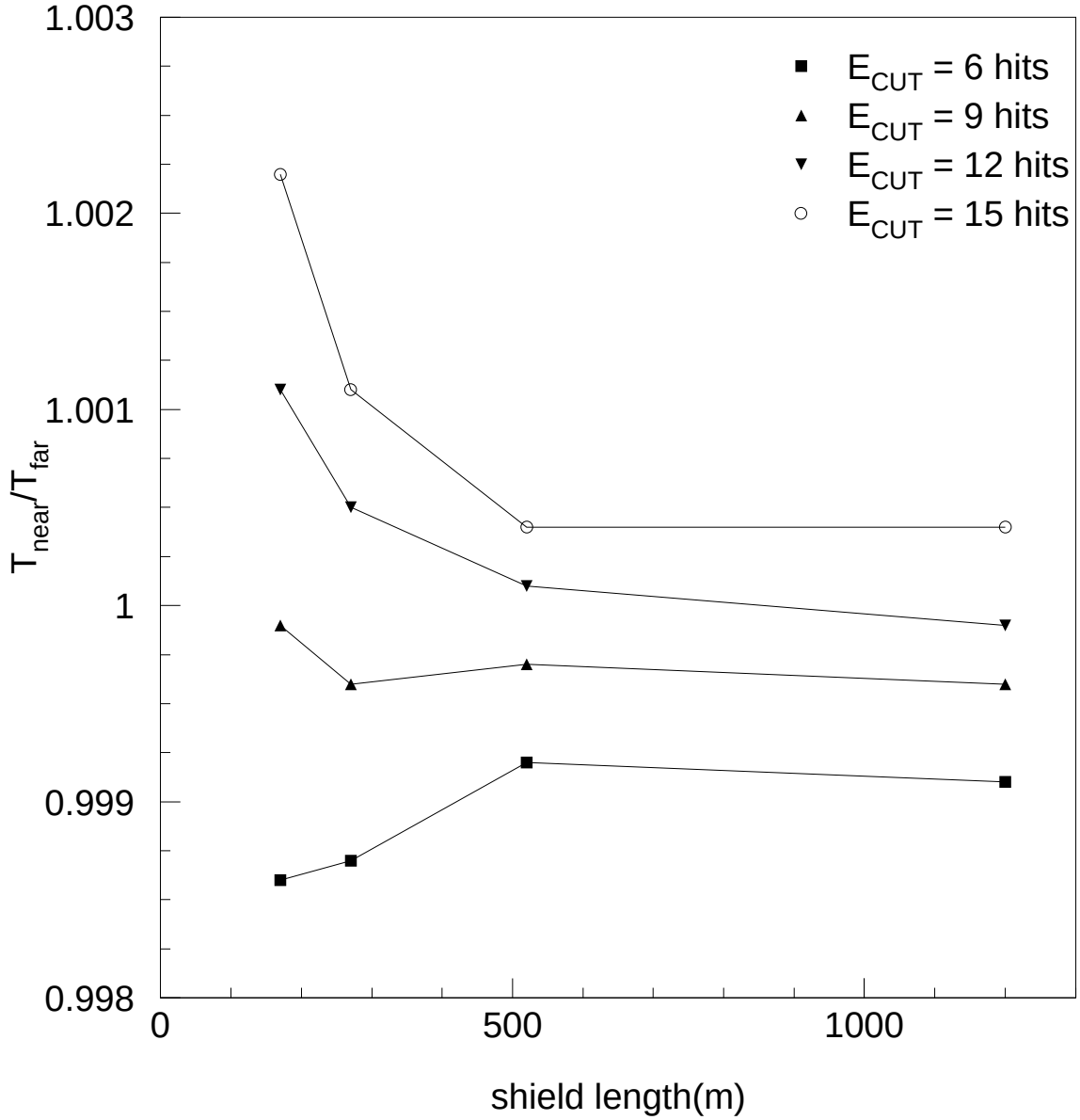

Figure C.5: Dependence of the ratio T_{near}/T_{far} (where T = CC/total event ratio) on shield length d for four different energy cuts.

near-detector location to the site boundary is about 1.7 km. We can envisage physics developments which would motivate such an upgrade in the future. For example, if the LSND results hold up with additional data and further analysis, this general location would be well suited to a measurement of $\nu_\mu \rightarrow \nu_e$ oscillation parameters with the Main Injector neutrino energy spectrum. Such an upgrade would also allow for a potentially much lower systematic uncertainty due to near-far beam differences; thus the higher neutrino fluxes which might be available in the future would provide a justification for this upgrade. A rough cost estimate for such an experimental hall ("800/1200") indicates a cost of about $10M (without multipliers) for the hall, shaft, utilities, etc., exclusive of detector costs.

C.2 Question #1 (c): Lower Neutrino Energies

For the longer term, what are the possibilities, if any, for lowering the neutrino energy and effectively using it to extend the lower end of the Δm^2 range?

C.2.1 Introduction

Different methods are used to enhance the flux of low energy neutrinos in the narrow-band beam (NBB) and the wide-band beam (WBB) configurations. For the NBB, we have adjusted the position of the production target while keeping the lithium lens current fixed at its nominal value. For the WBB, we have investigated the effect of decreasing the horn currents to improve the acceptance at lower energies. The results of these studies are described in the following two Sections.

C.2.2 Narrow-band beam

Table C.1 shows the integrated ν_μ fluxes and event rates (for a 7 kT fiducial mass MINOS far detector operated for two years) obtained for NBB tunes between 10 GeV and 45 GeV. Figure C.6 shows the NBB neutrino energy spectra for 10 GeV, 20 GeV, and 45 GeV tunes. The position of the production target was adjusted for each energy, while keeping the lithium lens gradient at its nominal 100 kG/cm and scaling currents in the remaining beam elements, as described in Section 3.4.5 of this report. No attempt was made to optimize target length. Figure C.7 illustrates the gain in NBB flux at low energy which results from properly positioning the one-interaction-length production target with respect to the lithium lens focal point. Reabsorption of pions in the target and lithium lens has been included in our calculation, but the tertiary production of low energy mesons from secondary hadrons has not.

The NBB geometry used for these calculations is somewhat different from that described in the main body of this report. The design adapted for the following estimates uses smaller bend angles to accept lower production angles. This can lead to increases of the NBB neutrino flux at low energies of as much as 20% compared to the original configuration. However, operation at NBB energies greater than 45 GeV is not possible in this configuration.

C.2.3 Wide-band beam

To design a maximally efficient low-energy wide-band beam would require a complete study of horn shapes as well as their spacing and currents. In addition, appropriate changes in the target design would also enhance the low energy neutrino flux. During the short time available since the June meeting we have attempted to improve the low-energy performance of the WBB solely by decreasing the horn currents from the nominal value of 170 kAmp to 50 kAmp. Figure C.8 shows the relative flux of the beams with these two horn currents while Table C.2 summarizes the neutrino energy spectra obtained for these two horn currents and compares it to that achieved with the NBB tuned for 10 GeV pions. Note that substantial flux increases at low energy have been achieved while the high energy component has been reduced by over an order-of-magnitude. Flux, backgrounds, and detector performance at

low energy, in addition to physics backgrounds, will all be important in determining the preferred mode of operation of the NuMI beam for a given experiment.

C.2.4 Conclusion

Effective increases in the low-energy component of both the wide-band and narrow-band NuMI beams have been obtained even without the benefit of a complete goal-oriented redesign of the beams. The fluxes quoted should be viewed as conservative because complete optimization has not been done as yet. In addition, tertiary production in the target should enhance the low energy part of the spectrum. The eventual mode of low-energy running will be chosen on the basis of event yield, background and detector performance, as well as physics requirements.

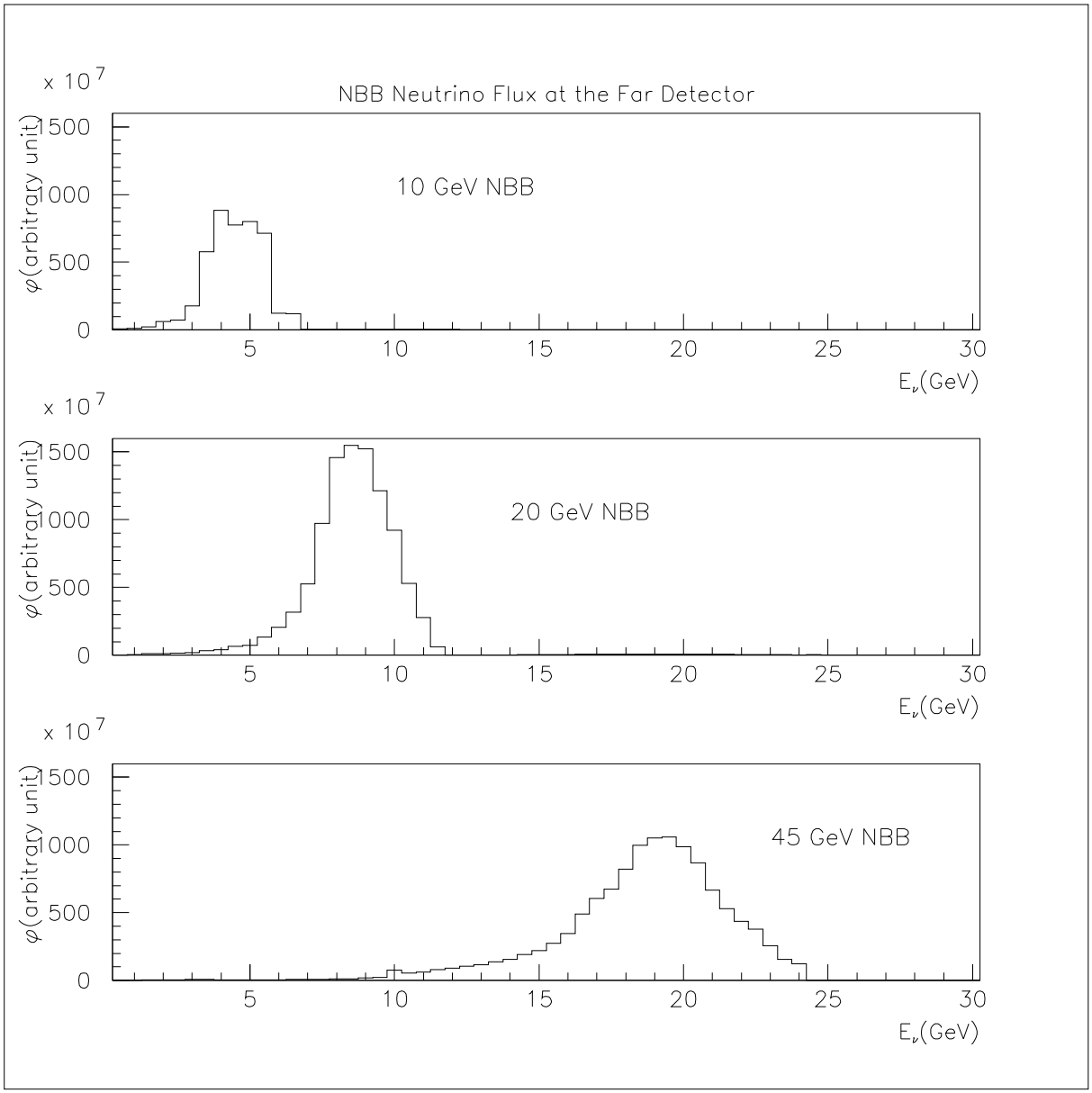

Figure C.6: The ν_μ fluxes at the MINOS far detector for the NBB tuned to 10, 20, and 45 GeV.

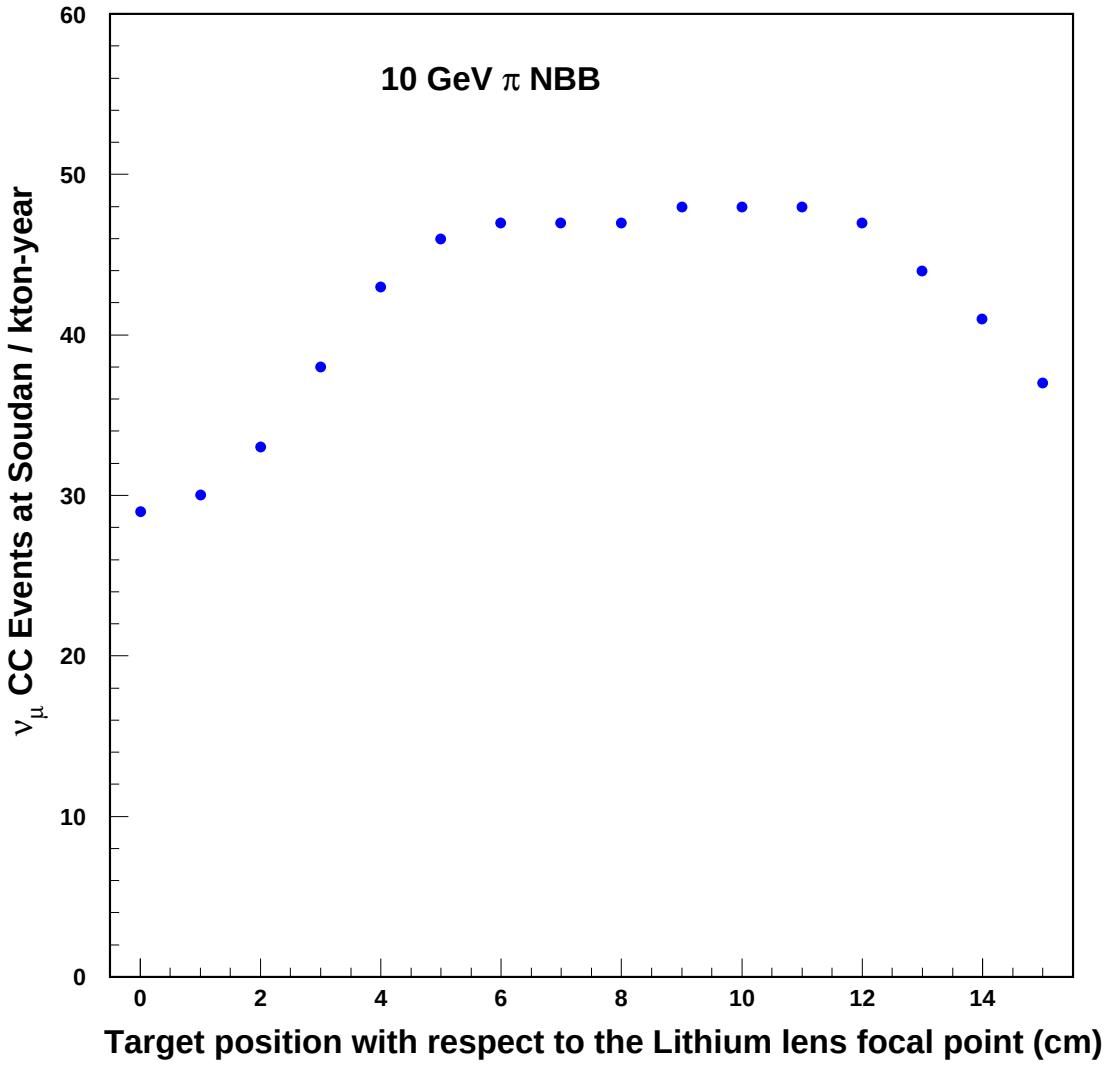

Figure C.7: The ν_μ CC event rate at the far detector as a function of the position of the upstream end of the target (in cm) with respect to the lithium lens focal point (for a one kT-year MINOS exposure). The position plotted is positive as the target is moved upstream.

NBB Energy (GeV)	ν_μ Flux ($\times 10^{10}$)	ν_μ Events	ν_τ CC/ν_μ CC (percent)
10	31	875	7.0
15	50	1910	13.8
20	71	3500	19.4
25	86	5250	24.3
30	94	6750	28.5
35	98	8175	32.0
40	96	9000	35.2
45	87	9000	38.0

Table C.1: Integrated NuMI flux and event rate as a function of energy, for a two year exposure of a 7 kT MINOS far detector. Neutrino flux is given in units of $m^{-2}GeV^{-1}$.

ν_μ Energy (GeV)	ν_μ Flux 170 kAmp ($m^{-2}GeV^{-1}$) ($\times 10^{10}$)	ν_μ Flux 50 kAmp ($m^{-2}GeV^{-1}$) ($\times 10^{10}$)	ν_μ Flux NBB ($m^{-2}GeV^{-1}$) ($\times 10^{10}$)
3.0	12	21	3.1
4.0	17	22	15
5.0	16	21	14
6.0	26	27	2.1
20.0	14	0.78	0
30.0	3.4	0.21	0

Table C.2: WBB energy fluxes for 170 kAmp (nominal) and 50 kAmp horn currents, compared to 10 GeV (E_π) NBB fluxes, at the MINOS far detector for a two-year exposure.

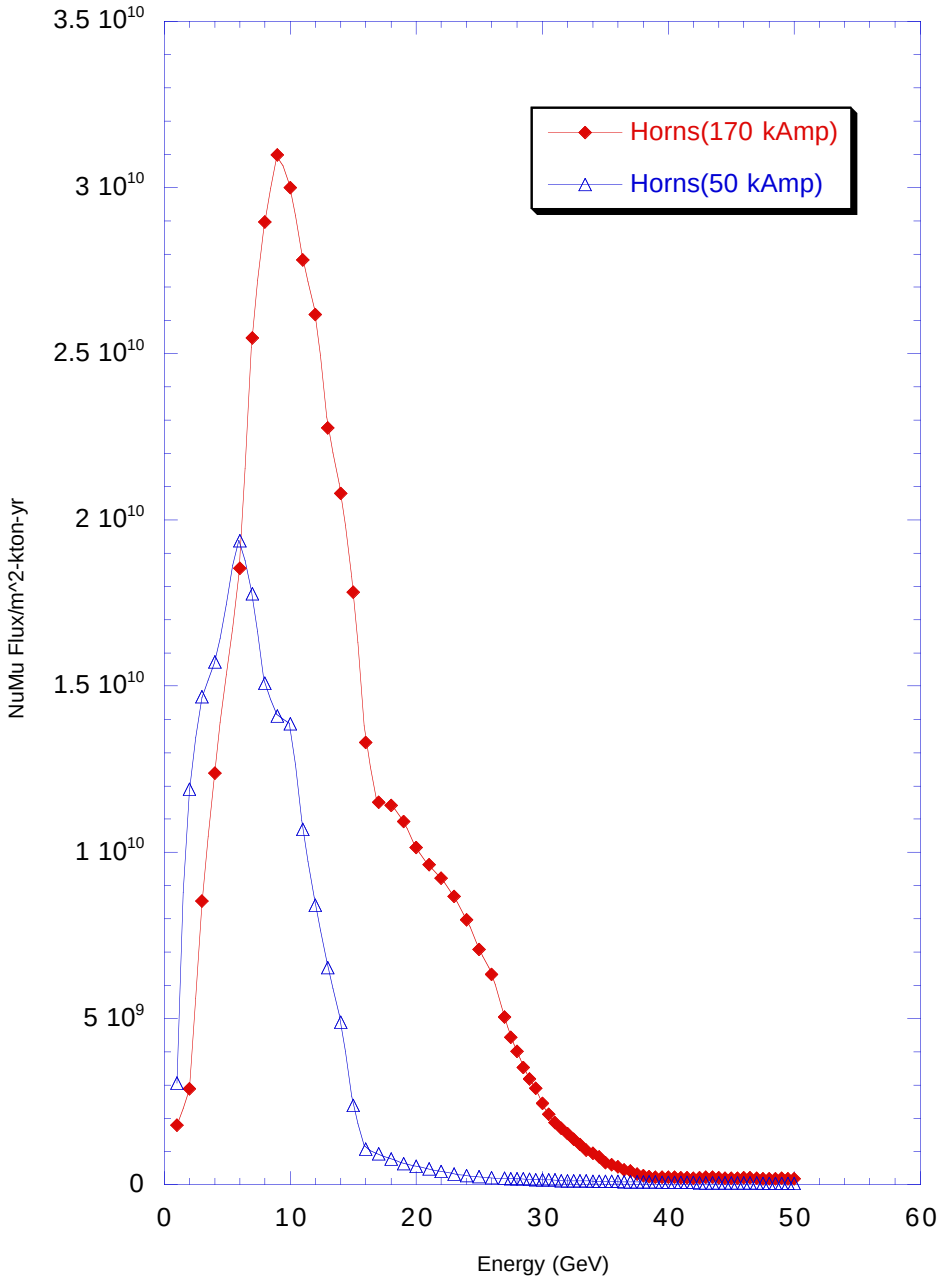

Figure C.8: Relative fluxes obtained from the wide band beam using the nominal (170 kAmp) and low-energy (50 kAmp) horn current settings described in the text.

C.3 Question #1 (d): Higher Energy Protons

What higher energy protons might be brought to the target of the new neutrino area?

C.3.1 Higher energy beam from the Main Injector

In this Section we consider the problem of extracting higher energy ($> 120\ GeV$) Main Injector (MI) beams and transporting them to the NuMI production target. In order to avoid additional civil construction, we constrain the primary proton beam to pass through the Main Injector MI-60 extraction stub.

Main Injector dipoles are designed for a maximum energy of 150 GeV. However, the good field region falls off to ± 25 mm (with sextupole correction) at 150 GeV, and resonant extraction has never been modeled at 150 GeV to determine if apertures and magnets are adequate.

The feeder, transformer and power supply system for the MI have not been designed to provide a 150 GeV cycle with a fast repetition rate for MI fixed target physics. The maximum ramp repetition rate is set by a combination of a 40 MVA average feeder limit for each half of the ring and a rms current limit of $\sim$5000 Amps in the dipole bus by the cooling water system. The current 150 GeV Tevatron fixed target injection ramp cycle time is 2.4 sec with a 0.25 sec flattop and requires an rms dipole current of $\sim$5500 Amps, which exceeds the limit imposed by the cooling system and the power supply transformer. For this cycle to run continuously, the repetition rate must be slowed to reduce the rms current to $\sim$3600 Amps. This corresponds to $\sim$5.4 sec cycle time.

Currently, the primary proton energy for $\bar{p}$ production is 120 GeV. To maintain compatible operation of the NuMI beamline and $\bar{p}$ production at 150 GeV, we would also have to upgrade magnet power supplies and cabling in this transport line.

In summary, although 150 GeV cycles can be run for short periods of time, the MI was not designed to support a 150 GeV program. Continuous operation would require an increase in the cycle time of almost a factor of three, which would more than cancel any gain in production cross section with higher energy protons.

C.3.2 Tevatron beam possibilities

The challenge of bringing Tevatron beams to the NuMI production target includes the design of a new high energy extraction system and the transport of high energy beam to the target. As described below, this is not possible without major civil construction and reconfiguration of Tevatron accelerator components.

A possible running scenario might be to inject 10 - 12 MI batches into the Tevatron (two Main Injector cycles), accelerate to 400 GeV and resonantly extract from the Tevatron over a 2 to 3 msec time period. The Tevatron cycle time would be on the order of 20 to 25 sec.

The only two Tevatron extraction locations which could be used for targeting on the NuMI target are straight sections E0 and F0. Straight section F0 is utilized for Tevatron RF and for injection from the Main Injector. It is parallel to, and offset from, MI-60 by 11.8 m. F0 is also 2.33 m higher than the MI in elevation. F0 contains the Tevatron RF in

the upstream half and injection Lambertsons in the downstream half. It has no additional room to accommodate extraction equipment without moving the Tevatron RF to another location. Moving the RF to, for example, E0 would make room for extraction Lambertsons, with the electrostatic septa being located at an upstream straight section C0, D0, or E0. Many details of how to accomplish this would need to be worked out.

Even if additional lattice space were available, utilization of the $\bar{p}$ (A150) injection line tunnel for an additional beamline for NuMI is difficult due to the 160 mr angle required to enter the extraction stub from the $\bar{p}$ beamline enclosure. The highest energy that could be transported through the 160 mr bend is $\sim$100 GeV utilizing two Tevatron dipoles. In order to transport 400 GeV beam, the antiproton transfer line would need to be rebuilt and enlarged to accommodate the cryogenic transfer line.

Extraction from Tevatron straight section E0 would require substantial new civil construction, for example a tunnel which would intersect the MI-60 straight section and/or the Tevatron injection lines from the MI. This would require the duplication of about one sixth of the Tevatron to get around to the MI-60 straight section. Major civil construction in the MI-60 area would also be required.

It is relatively easy to upgrade the MI extraction stub to 400 GeV operation. The stub contains $\sim$100 mr of vertical down bend utilizing four recycled Main Ring 6-meter B2 magnets. Replacing these with five Tevatron dipoles (4.4 Tesla) will allow the transport of $\sim$400 GeV protons to the target. The four EPB dipoles in the pretarget enclosure would be replaced with three Tevatron dipoles.

In summary, it might be possible to provide $\sim$400 GeV beam to the NuMI production target, although major civil construction would be required. A careful and detailed design study will be needed to check this conclusion and to provide a cost estimate. The impact on other Fermilab programs would also have to be addressed.

C.4 Question #1 (e): Effects of the Decay Pipe Baffles

How do the decay pipe baffles affect the neutrino rates? How is the knowledge of the beam character influenced? Is this reflected in the beam measuring/monitoring devices?

The current design of the NuMI target hall and decay pipe includes collimators after each horn and at four locations along the decay pipe. The locations of the collimators have been chosen to minimize the radioactivity induced in ground water near the target hall and decay pipe during wide-band beam operation. Table C.3 lists the z positions and inner diameters of the 5 m long collimators described in Chapter 7 of this report. The design described in the Status Report was an initial, nonoptimized attempt to solve the radiation safety problem induced by beam scraping. We are attempting to find a solution, perhaps involving a decay pipe radius increasing with distance from the target, which will eliminate the need for most, if not all, of the collimators.

The beam program NUADA[19] was run to determine the effect of this collimator configuration on the neutrino rates at the far detector and on the radial distribution of neutrinos at the near detector. Note that the collimators influence only wide-band beam running and have no effect on the narrow-band event rates.

Enclosure	Distance from target	Inner Diameter
Target Hall	6 – 11 m	40 cm
Target Hall	23 – 28 m	50 cm
Target Hall	45 – 50 m	50 cm
Decay Pipe	100 – 105 m	75 cm
Decay Pipe	215 – 220 m	75 cm
Decay Pipe	295 – 300 m	75 cm

Table C.3: The locations and inner diameters of the collimators along the NuMI beamline.

The collimators reduce the ν_μ CC event rates at the MINOS far detector (in the absence of oscillations) by 12%. The primary reduction in event rate occurs for $E_\nu < 18$ GeV, as shown in Figure C.9a). The near-far energy spectrum differences, shown in Figure C.9b), are essentially unchanged by the collimators.

The radial distribution of neutrino events at the near detector location is expected to change with the introduction of the collimators. Figure C.10 shows the ν_μ CC event rate in four radial regions of the near detector. These are clearly different for the collimated and uncollimated beam configurations.

Our beam simulation model shows that the effects of the collimators will be easily observable in the meson beam characteristics within the decay pipe, and in the energy and radial distributions of neutrino events at the near detector location. We believe that the beam measuring and monitoring devices previously described in Chapter 6 will provide measurements which are sufficiently detailed to allow an accurate prediction of the characteristics of the neutrino flux at the MINOS far detector from the collimated hadron beam.

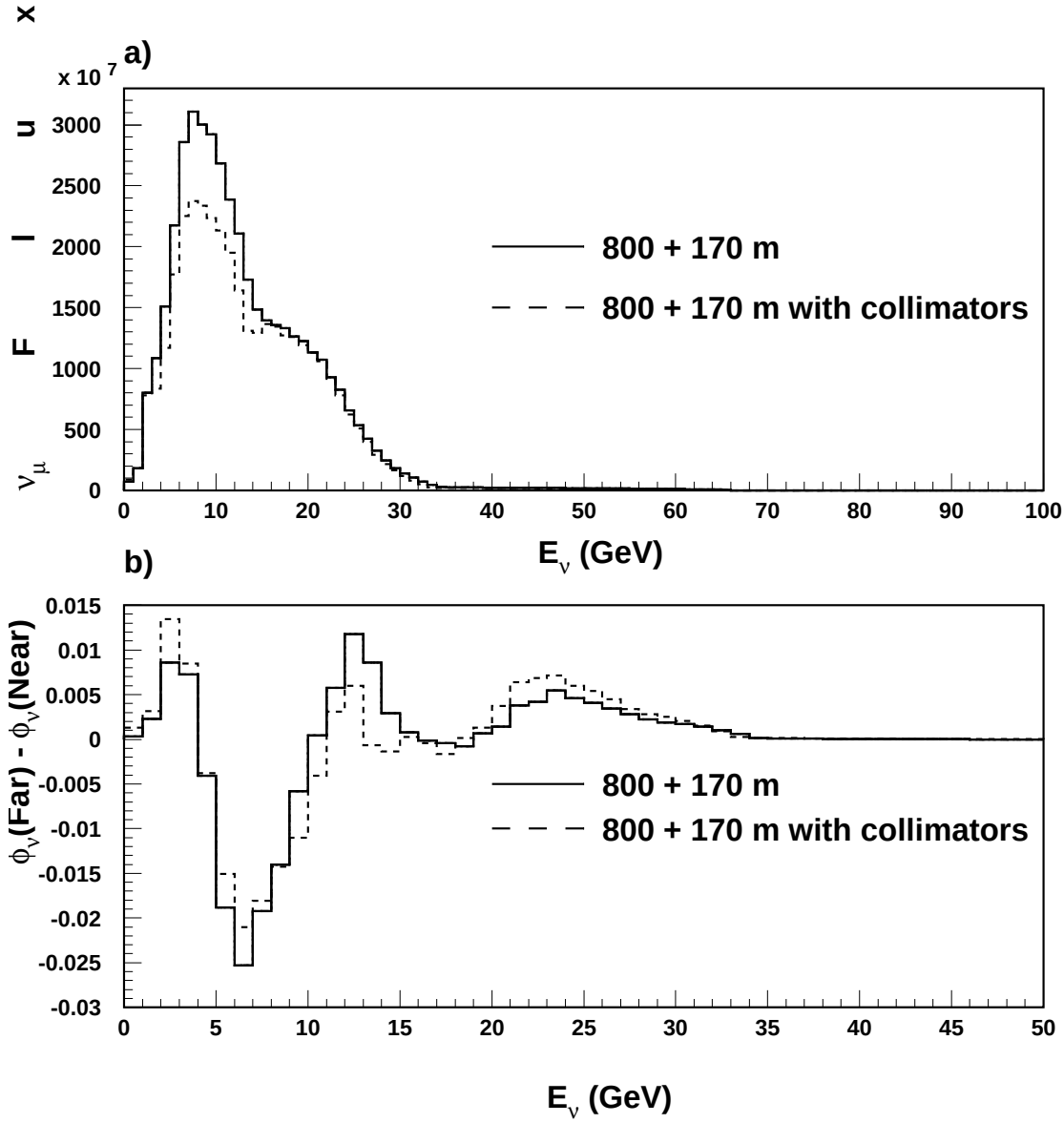

Figure C.9: a) ν_μ fluxes for the uncollimated and collimated wide-band beams. b) The far-detector flux minus the inner near-detector flux, normalized to unit areas, for the uncollimated and collimated beams.

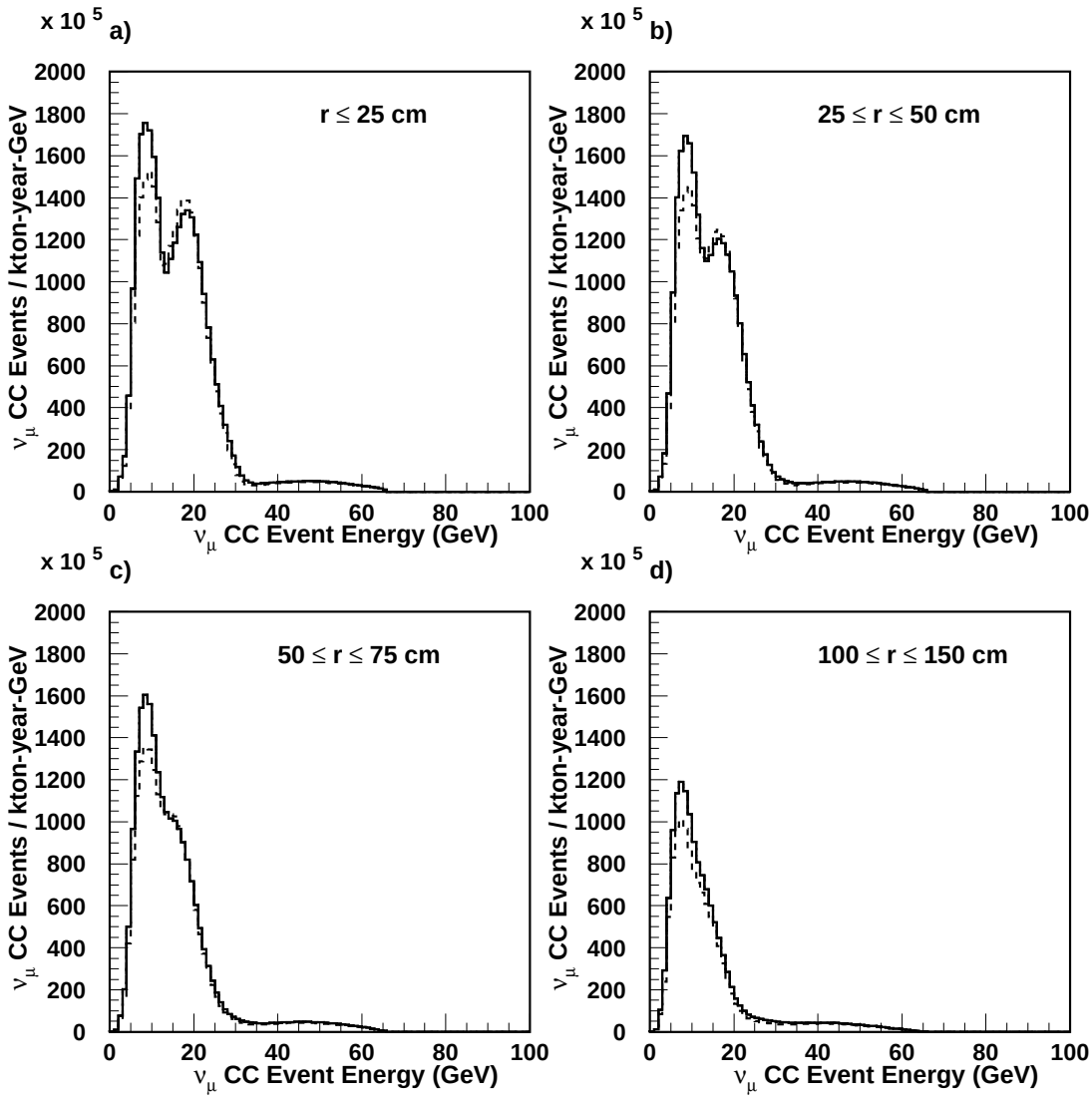

Figure C.10: The ν_μ CC event rates for the nominal beam and the beam with collimators for four different radial regions in the near detector.

Bibliography

[1] e.g. "Summary of Fermilab Neutrino Physics" at the Workshop in Neutrino Physics at Fermilab, September 1988, Fermilab.

[2] N. Reay (spokesman), *E–803 proposal for ashort baseline experiment at Fermilab*, October 1990; revised October 1993.

[3] Proceedings of the Workshop on Long-Baseline Neutrino Oscillations, November 17-20 1991, M. Goodman editor, Fermilab.

[4] R. Davis *et al.*, in *Proc. 21st Int. Cosmic Ray Conference, Adelaide, 1990*, Vol. 12, p. 143; P. Anselmann *et al.*, Phys. Lett. **B285**, 376 (1992), Phys. Lett. **B285**, 390 (1992), Phys. Lett. **B314**, 445 (1993); A.I. Abazov *et al.*, Phys. Rev. Lett. **67**, 3332 (1991); K.S. Hirate *et al.*, Phys. Rev. Lett. **65**, 1297 (1990), Phys. Rev. Lett. **66**, 9 (1991), Phys. Rev. **D44** 2241, (1991).

[5] e.g. G.L. Fogli and E. Lisi, "On the Atmospheric Neutrino Anomaly and its Statistical Significance", IASSNS-AST 95/21, submitted to Phys. Rev. D. 1995.

[6] See, *e.g.* H. Harari, Phys. Lett. **B216**, 413 (1989).

[7] Letter to Snowmass '94 participants in Particle and Nuclear Astrophysics and Cosmology in the Next Millennium, John Peoples, Director of Fermilab, June 27, 1994.

[8] *Proceedings of the Workshop on New Directions in Neutrino Physics, Fermilab, 1988*, edited by R. Bernstein.

[9] *Proceedings of the Workshop on Physics at the Main Injector*, Edited by Stephen D. Holmes and Bruce D. Winstein, May 16-18 1989.

[10] Linda Stutte, in Proceedings of the Workshop on New Directions in Neutrino Physics, 1988.

[11] *"Conceptual Design Report: Main Injector Neutrino Program"*, FNAL, 1991, edited by R. Bernstein *et al.*.

[12] T. Sager, *"P–875 Survey and Alignment, Status and Costs"*, NuMI-L-62 (1995).

[13] "Project Definition Report: NuMI Project (LBL MI–60 Revision 2)", Fermilab F.E.S.S, (1995).

[14] Virgil Bocean, Survey and Alignment Group, internal memo dated Nov. 3, 1994.

[15] The Fermilab Main Injector Technical Design Handbook, Chapter 2, August 1994.

[16] John Johnstone, private communication.

[17] H. Grote, F. C. Iselin, "The Methodical Accelerator Design (MAD) Program", CERN/SL/90-13(AP) , Rev.4.

[18] "E–803 Sensitivity to Antineutrino Contamination in the Beam", Noel Stanton, NuMI-S-25 (1994).

[19] NUADA, the Fermilab Neutrino Flux Program, D.C. Carey and V.A. White, June 1975, PM0011.

[20] "Empirical Formula for Thick Target Particle Production", A.J. Malensek, FN-341 (1981) and "Comparison of Particle Production Measurements and FN-341 with 100 GeV Protons", A.J. Malensek, NuMI-B22 (1994).

[21] The E803 Monte Carlo is by Noel R. Stanton, Kansas State University.

[22] A. E. Brenner, *et. al.*, Phys. Rev. **D26**, 1497 (1982).

[23] D. S. Barton, *et. al.*, Phys. Rev. **D27**, 2580 (1983).

[24] S. P. Denisov, *et. al.*, Nuclear Physics **B61**, 62 (1973).

[25] The horns and dichromatic beam line are designs by Anthony Malensek, Fermilab.

[26] The NUANL Monte Carlo is by Robert E. Blair and Daniel A. Crane, Argonne National Laboratory.

[27] ANSYS 5.0(1992),Swanson Analysis Systems,Inc. Houston,PA.

[28] A. Visser, "Preliminary Design Note for a Direct Coupled 200,000 Amp Neutrino Power Supply with Energy Recovery", Fermilab TM-1924, (1995).

[29] G. Dugan et al.,IEEE Trans. Nucl. Sci.30:3660-3662(1983).

[30] S. O'Day and K. Anderson, Proceedings of the 1995 IEEE PAC, Dallas Texas.

[31] A. Malensek, NuMI-B-39, Internal Note, October 1994.

[32] F. Nezrick and S. Lehoczky, NuMI-B 28, Internal Note, September 1994.

[33] R. Bellone et al., "Targets for High-Intensity Beams at CERN: Design, Operational Experience and Developments," CERN 86/ST/TE/A/113 (1986)

[34] POCO Graphite Inc., Decatur Texas, 76234.

[35] A. van Ginnekin, "CASIM - Program to Simulate Transport of Hadronic Cascades in Bulk Matter", Fermilab Report FN-272 (1975)

[36] "Beam Issues from a Short–Baseline Perspective", Noel Stanton, NuMI-S-40 (1994).

[37] R. Blair, *et al.*, NIM 226 p281 (1984)

[38] A. Van Ginnekin, "Weighted Mont Carlo Calculations of Hadronic Cascades in Thick Targets" NAL-FN-250 (1972);. Van Ginnekin and M. Awschalom, "High Energy Particle Interactions in Large Targets", vol. 1. Fermilab (1975); A. van Ginnekin, "CASIM - Program to Simulate Transport of Hadronic Cascades in Bulk Matter", Fermilab Report FN-272 (1975)

[39] D. Cossairt, "A Collection of CASIM Calculations", Fermilab TM-1140 (1982)

[40] Fermilab Radiological Control Manual, Chapter 13, Appendix 13A, Section 2.3 (October, 1993)

[41] M. Barbier, "Induced Radioactivity", North Holland Publishing Company, (1969)

[42] G. Lauten, Accelerator Division Assistant Radiation Safety Officer, private communication.

[43] DOE Order 5480.11, "Radiation Protection for Occupational Workers".

[44] T. B. Borak, M. Awschalom, W. Fairman, F. Iwami, J. Sedlet, "The Underground Migration of Radionuclides Produced in Soil Near High Energy Proton Accelerators", Health Physics 23 (1972) 679-687

[45] A. Malensek, A.A. Wehmann, A. J. Elwyn, K. J. Moss, and P. M. Kesich, "Groundwater Migration of Radionuclides at Fermilab", Fermilab TM-1851 (1993)

[46] J. D. Cossairt, "Use of a Concentration Based Model for Calculating the Radioactivity of Soil and Groundwater", Fermilab Environmental Protection Note 8, (1994)

[47] A. Malensek, "NuMI Groundwater Limits", NuMI-B-55, Internal Note, Jan. 1995.

[48] J. Schneps, S. Willocq and W.P. Oliver, *"Determining Δm^2 in E803: The Moveable Beam Stop"*, NuMI-S-60 (1995).

[49] The COSMOS Collaboration, "1995 Update Report on Fermilab E803/COSMOS, Short-Baseline Neutrino Oscillations to ν_τ," Fermilab report NuMI-S-94, June 6, 1995.

[50] Noel Stanton of the COSMOS collaboration provided Figure C.2.